Summer 8-2020

Mechanism of Compaction With Wrinkle Formation During Automatic Stitching of Dry Fabrics and the Size Effect of Compression Molded Discontinuous Fiber-Reinforced Composites

Anibal Benjamin Beltran Laredo
Old Dominion University, abelt005@odu.edu

MECHANISM OF COMPACTION WITH WRINKLE FORMATION DURING AUTOMATIC STITCHING OF DRY FABRICS AND THE SIZE EFFECT OF COMPRESSION MOLDED DISCONTINUOUS FIBER-REINFORCED COMPOSITES

by

Anibal Benjamin Beltran Laredo

A Thesis Submitted to the Faculty of
Old Dominion University in Partial Fulfillment of the
Requirements for the Degree of:

MASTER OF SCIENCE
MECHANICAL AND AEROSPACE ENGINEERING

OLD DOMINION UNIVERSITY
August 2020

Approved by:

Oleksandr G. Kravchenko (Director)

Sebastian Bawab (Member)

Xiaoyu Zhang (Member)

ABSTRACT

MECHANISM OF COMPACTION WITH WRINKLE FORMATION DURING AUTOMATIC STITCHING OF DRY FABRICS AND RANDOMLY ORIENTED COMPRESSION MOLDED DISCONTINUOUS FIBER-REINFORCED COMPOSITES

Anibal Benjamin Beltran Laredo

Old Dominion University, 2020

Director: Dr. Oleksandr G. Kravchenko

With an ever-increasing demand for composites, more ways of manufacturing them are becoming popular and widely used. Stitching of dry fabrics is an efficient method for improving delamination resistance. Discontinuous fiber reinforced composites can be used as a lightweight alternative material for metals through a process of compression molding, which allows for complex shape manufacturing while offering structural grade mechanical properties.

This study demonstrates how the stitching of dry fabrics can be adapted to more complex surfaces. The consequences of stitching of curvilinear surfaces can result in defect formation. Therefore, to understand the physical formation of possible defects, experimental characterization methods were proposed, which considered a compaction test, a roller compaction test with fabric pull to induce a wrinkle formation. A stitching system available at the NASA Langley Research Center was used as a basis for the automated stitching. It was concluded that a purely compaction pressure over 100 kPa would densify the fabric enough that the resin infusion process after stitching could be affected. The pulling of the fabric demonstrated that pressures over 400 kPa along the surface result in permanent fiber damage which will affect the structural properties of the composite after curing. To mitigate the damage of dry fabrics during automated stitching at NASA, a new component called the presser foot was designed to replace its old stiff counterpart. This piece will allow for a more flexible stitching process able to accommodate to more complex surfaces.

The carbon/epoxy thermoset was adapted from a continuous pre-impregnated fiber tow to form a discontinuous platelet-based type molding compound. Due to the increasing aspect ratio of the platelets, mechanical properties increase, but after a certain point these properties decrease due to a reduced platelet count in the sample. A premade glass-fiber/nylon thermoplastic composite demonstrated there is a general fiber orientation in the almost randomly oriented composite, which helps control the material behavior. The span of the samples during testing was changed to simulate the change in fiber length of the composite. Both kinds of composites showed there is an increase to material properties as fiber length increases.

Dedicated to my father, mother, and sister for supporting me every step of the way

ACKNOWLEDGMENTS

I would like to thank Dr. Kravchenko for helping me get to this level of education while providing his knowledge, patience and support. Special gratitude to the ODU Mechanical and Aerospace Department and its faculty members: Dr. Bawab and Dr. Kravchenko, along with NASA Langley Research Center members: Dawn C. Jegley and Andrew E. Lovejoy for allowing me to be part of the Structural Mechanics & Concepts Branch, who all helped fund my research and get better in many aspects of my academic career. Thanks to everyone who is/was part of the Composites Modeling and Manufacturing Lab for helping me along this road while enjoying their presence and friendship. I would also like to thank everyone in my committee for their time and support. Thanks to Cooper for being available to machine my metal pieces during the COVID-19 pandemic when no one else could. Lastly, I would like to thank my family and close friends for their moral support throughout these years.

TABLE OF CONTENTS

LIST OF TABLES

Table Page

TABLE OF FIGURES

Figure Page

1 INTRODUCTION

With an ever-increasing demand, more ways to manufacture composites are becoming popular and widely used within the aerospace, automotive, and energy industries. Offering great strength, stiffness, and rigidity at low density, fiber reinforced composites are used as a lightweight alternative material to metals. Some commonly used configurations are: pre-impregnated aligned fibers, dry woven or non-crimped fabrics, and discontinuous fibers. These three types of composites can be categorized into continuous and discontinuous fiber reinforced composites.

1.1 Continuous Fiber Reinforced Composites

Aligned composites can be extremely anisotropic, meaning that their longitudinal tensile loads are high, but they have weak transverse loads in the y and z directions [1]. This anisotropy is due to the fact that stress concentrations are carried along the fiber direction, and the matrix alone is weak and brittle. So, if loads are applied in directions other than along the fiber, the composite can easily fracture. Another disadvantage of this type of composite is that it usually comes with the matrix in an uncured state, therefore, the pre-impregnated fibers need to be refrigerated for the material to stay useful until curing takes place. An experimental analysis inspecting the strength of an arbitrary material proved this weakness by examining a specimen with three cured laminate of continuous fibers loaded under uniaxial tension. The two outer layers in the 0-degree direction, i.e., or aligned with the load, and the center layer perpendicular to the loading direction. After data analysis, the calculated strength along the x direction was 37 times stronger than the load along the y direction [2]. The anisotropy of the material can be taken advantage of by having several layers oriented at different directions on top of each other, giving it higher material properties under several loading conditions. Another study investigated biaxial

fatigue loadings applied to a quasi-isotropic layup configuration of $[0/-45/45/90]_s$. Delaminations started between the 45 and -45 degree plies but delays in damage propagation were observed, leading to a more uniform load distribution and decreases in stress amplitudes around the tested regions [3].

The next type of commonly used composite are dry woven or non-crimped fabrics. Since they are also continuous fibers, the fabrics have many of the same applications as pre-impregnated aligned fibers, with the difference being that the fiber threads/bundles are woven so that fibers run in multiple directions introducing waviness in the bundle, or they are held together by a thin polyester yarn to avoid most of the through-thickness fiber misalignment seen in woven fabrics. But this textile preform does not come impregnated with a matrix, leading to a reduced cost and extremely long storage time with no impact on properties or workability. The downside to using dry preforms is that resin infusion will ultimately be needed, which is one extra step that can itself be challenging. A structural evaluation of woven composites concluded that understanding and knowing the fiber orientation is a critical step before resin infusion takes place [4]. Stitching these weaves and fabrics before infusion is one of the ways of combining several layers together, and what makes it unique is exactly what the name implies. Two or more laminates of pre-aligned dry fibers are stitched together with threads such as Vectran to combine and hold the structure together. Each part then goes through the infusion process that is based on the principle of a pressure difference between the vacuum bag and resin supply [5]. Small parts are commonly manufactured with autoclaves, but as the size of the desired structure increases the cost of production quickly increases as well. Large parts can instead be manufactured without autoclaves to reduce cost, therefore, the use of just a flexible film as the vacuum bag makes it easy for immense structures such as wind turbine blades to be made and avoid the alternative

most expensive method. This also helps “enclose” the system within the confinements of such procedure, thus minimizing the exposure of hazardous and volatile chemicals to the worker(s). Additionally, due to the separate use of fibers and resin previously mentioned, there is no need for cold storage units for pre-impregnated carbon fiber, whereas dry fiber rolls or preforms can be stored almost indefinitely at room temperature, which significantly reduce expenses of production and risk of scrapping a part. Even though this alternative of composite manufacturing is an improved cost-effective method for lighter, high strength, and high-quality parts; it is important to understand that out-of-autoclave methods are still far from perfect and this technology should be considered an evolving technique. Many improvements are happening around the industry each year, but certain aspects of resin infusion which will be discussed further in this paper can result in defects that are not easily avoidable.

1.2 Discontinuous Fiber Reinforced Composites

The last type of material form are discontinuous fibers; in this case, even though short discontinuous fiber reinforced composites are not as strong as the two previous pre-aligned structures, they can instead offer isotropic properties that unidirectional fibers do not, in addition to a cheaper manufacturing process. Failure modes for randomly oriented fibrous structures are also not as catastrophic as their more-expensive counterparts due to the lack of long fiber stress buildup, and they can be more flexible under certain loading conditions. This type of composite is manufactured through a compression molding process.

To understand the basics on failure mode for this type of fibers, a micromechanical simulation study was attempted based on failure under tensile loads when all the discontinuous fibers were aligned with the load. The study determined that the main failure mode was fibers breaking when the fibers were sufficiently long. On the other hand, fibers did not fail when they

were short, and the main failure was matrix crack propagation, where a single carbon fiber diameter was 7 micrometers with long and short fibers ranging from 2-4 and 0.3-1 mm, respectively [6]; indicating that the size of the fibers used and the effects it has on the composite could change its material property responses. Another study evaluated elastic constants and bond stresses by analytically studying a single cylindrical body in an infinite matrix first, and then used point matching methods for composites of repeated overlapping fibers under uniaxial tension [7]. Elastic constants were found to increase as fibers were closer to each other while also reducing bond shear fractions. Results also demonstrated that when fiber/matrix bonds progressively fail, bond behavior is the same as fully bonded fibers of shorter lengths. A model for predicting the elastic properties of randomly oriented fibers concluded that when a material is hot pressed, it becomes transversely isotropic. If fiber length-to-diameter ratio is large, 1000+, in-plane properties also become less isotropic while having the opposite effect when the fibers become shorter [8]. This study on predicting properties for randomly oriented fiber composites also assumed a defect-free composite but made remarks that micro voids, broken fibers and fiber/matrix debonding cannot be prevented since this material fabrication requires plastic deformation of the matrix. Discontinuous fiber reinforced composites are mainly used for secondary structures that are not subjected to extreme loading conditions. One example of such is an application to aircraft interiors; these composites are not implemented as part of the fuselage or wings, but they can instead be used for the inner parts like seats, tables, and secondary panels throughout the surroundings. The automotive industry also makes significant use of this process for light weighting cars due to its feasibility on adapting to 3D objects. Frequently, short dry fibers are byproducts of other engineering projects and they are treated as scrap. So, this material is readily available and can be used for other purposes without a separate

purchase. Most of the process for manufacturing this composite relies on two steps: the use of any amount of a chosen type of fiber and length, and the combination of a matrix to hold the fibers. The two materials are combined and cured using a compression molded process, where unidirectional forces are applied, and the temperature required varies depending on the matrix used. An intriguing experimental study on thermoplastic optimization manufacturing for bio-composites [9] emphasized the importance of how the crystallization of the composite going through its curing cycle can influence the material properties once fully treated. The study concluded that the main factors for a proper compression molding process are: increasing pressure, temperature, and processing time such as consolidation and cooling rate all favor fiber/matrix impregnation resulting in higher crystallization of the matrix, thus, resulting in higher material properties for strength and modulus. However, the factors for processing time of temperature and cooling rate have counteracting effects. Higher temperatures result in composite degradation of the fiber and matrix. Where fast cooling rates of -25 ^{o}C/min gave better results than with slow cooling at -2 ^{o}C/min. The chosen optimal cooling results of -15 ^{o}C/min gave a slight increase in both material properties, but the differences were not too substantial from that of a fast cooling rate. Consequently, it is important to understand what happens when the composite begins to cool down. A process called nucleation begins, which leads to the overall crystallization of the matrix, and determines the final material properties. An investigation looking into this subject analyzed the effects on loading for polyamide 6 (PA6) carbon and glass fiber preform composites. Levels of crystallinity were calculated by comparing the enthalpy values from heat-cool-heat scans for each experiment to the 100% crystalline PA6 enthalpy; with 44% and 26% for carbon and glass fiber composites, respectively. The carbon fiber samples gave higher elastic modulus and tensile strength, which was expected due to their material properties

alone, and not much crystallinity value variation was seen per group type [10]. Whether the composite is a discontinuous or continuous fiber structure, the degree of crystallinity will have a significant effect on the material properties.

When considering the mold itself, it is usually custom made to fit a specific design and goal that can also be adapted to injection molding for more complex geometries [11], therefore it can be quite expensive to make it at first, but once it is ready, discontinuous fiber composites can essentially be mass produced one after another. However, since each new piece can vary between part making due to the nature of the composite, a certain workflow is designed to reduce manufacturing error and minimize low quality part making when manual assembly is in place. Software and multi-objective optimization are used to identify patch positions for the uncured material and predict flowability as compression molding takes place. The composite is then analyzed with thermography and fiber orientation before experimental data can be acquired for certification and mass producing of these polymer structures [12].

This study focused on two topics. The first one is focused on discontinuous fiber reinforced composites which showed how a simple geometric compression molded process can be used for both, an adapted platelet-based thermosets and thermoplastics. The second topic is focused on stitching parameters of pre-aligned dry fibers and the effects it has on the fabric, followed by modeling of a new piece aimed to facilitate stitching on uneven surfaces.

1.3 Background

1.3.1 Discontinuous Fiber Systems

Part of this thesis research was directed towards the use of the IM7/8552 material, a high-performance pre-impregnated carbon fiber thermoset created by Hexcel Corporation. This material was adapted to a platelet-based form composite using a compression molded technique in order to understand the material properties when the platelet size varies during a three-point flexural test at a constant span. Two studies examining this form of thermoset used a similar approach for a T700/2510 fiber/epoxy material from Toray Industries. As fiber length increased, ultimate tensile strength, compression and flexural responses also increased, while mechanical properties stayed relatively stable for all types of moduli. Notched and unnotched tension tests showed similar results where the hole did not appear to affect the responses when the diameter was small and failed in between the grips and the hole but became a predominant failure initiation location as it increased. All tests displayed important effects for strength values based on platelet dimension [13,14].

Since it is common to use carbon fiber while making composites, it is important to analyze how other types of fibers and matrices behave within similar parameters. For that reason, the other part of this thesis focused on a different material consisting of discontinuous 25.4 mm long bundles of glass fiber infused with a polyamide 6 (nylon) matrix. The span on the samples tested during three-point flexural tests varied in order to understand the size effect on mechanical properties. This is an AP Nylon thermoplastic organosheet composite CR-6 series [15] that comes from Johns-Manville (JM) Corp. Polyamide 6 synthetic matrix has many uses due to its adaptability with other materials, including carbon fiber. A technique for joining discontinuous fibers reinforced composites with this matrix was developed using a riveting method which

showed no compromise of the structure after connection [16]. Composites made with nylon become weaker as temperature increases; an experimental study in the toughness of the fiber/matrix interface for glass fiber-nylon composites tested samples at different temperatures. The interfacial toughness, or interfacial crack, G, decreased as temperature rises, which would be expected for such material [17]. Changes of material properties such as flexural strength and flexural modulus along with the size effect of the fibers with respect to the span chosen during three-point bending loading conditions for a better understanding of the fiber-matrix interactions are of interest.

1.3.2 Continuous Dry Fiber Systems

NASA has previously worked with the Boeing Company (Boeing) in the development of stitched composite structures [18]. The Pultruded Rod Stitched Efficient Unitized Structure (PRSEUS) concept was created as a part of a project aimed to reduce the impact on the environment. The Environmentally Responsible Aviation (ERA) project was established to achieve this goal by creating lighter unconventional aircraft configurations and moving on from the common wing-to-tube designs. Thus, the Hybrid Wing Body (HWB) structure was designed to better improve the lift to drag ratio while at the same time making it in a cheaper and efficient manner, Figure 1. For an HWB configuration, the pressure cabin would also change from a circular cross-section to that of a rectangle one. Therefore, the internal pressure cabin configurations would be different in shape when compared to the most common models we see in the industry today.

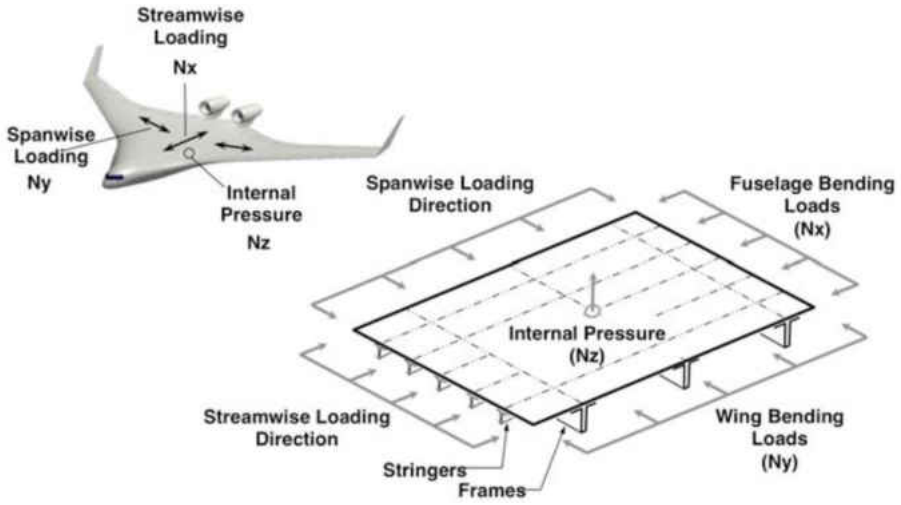

Figure 1 HWB Pressure Cabin Structure Concept

- Development of Stitched Composite Structure for Advanced Aircraft

This new shape will also affect the locations of the engines, therefore giving the plane a better aerodynamic configuration over its counterpart. Some of the design changes this type of plane encounters is the need for continuous structures within the body to accommodate the new load magnitudes in all the X-Y-Z directions. The rectangular cross-sectional fuselage would not withstand repeated pressure cycles, thus, continuous load paths due to stitching would be the only way this shape is possible while also reducing overall part count and avoiding thousands of metal bolts and attachments. The need of such substantial amount of parts increases the chances of structural failure such as cracks and delamination problems at their points of connections, whereas continuous structures would minimize the chances of defects with fewer components needed while drastically reducing overall weight [18].

The continuous structural connection of the HWB helps the uninterrupted load paths better support the loading conditions of the new plane design with its non-cylindrical pressure chamber and avoid most of the fastener pull-through problems from current models which are used to reduce delamination. Such manufacturing process was accomplished using dry material and single sided stitching with precured high-stiffness pultruded rods. Stitching was strategically placed along key structural interfaces, as they have shown suppress out-of-plane failure modes, delamination, and resist crack propagation along the web frame of the structures [18,19].

Automated machines can help facilitate stitching of dry fabrics; however, this is primarily applied to flat surfaces. The Integrated Structural Assembly of Advanced Composites (ISAAC) robotics system at the NASA Langley Research Center, shown in Figure 2, can be used for stitching through the thickness of dry fabrics. With seven total degrees of freedom to help with movement of the machine, ISAAC can also be used for AFP of pre-impregnated tows of carbon-epoxy material, and cutting laminates with an ultrasonic knife prior to curing.

Figure 2 ISAAC robot at NASA Langley Research Center

The software used to control this machine consists of two parts; the first one is called Vericut Composites Programing (VCP) and the second one is called Vericut Composites Simulation (VCS); both were created by CGTech Inc. VCP is used to identify an object or surface created from CAD programs like CREO Parametric, and then to customize it to identify paths based on certain initial parameters and locations given; this methodology creates a G-code that ISAAC uses to place material on a surface. Due to the sheer size and cost of the machine, it is absolutely crucial to run simulations with any program created to diagnose any possible collisions and joint movement errors based on the location of the machine, its surroundings, and the object/surface under question. VCS is, basically, a virtual 3D space representation of

ISAAC's clean room interior as shown in Figure 3, where the locations of every important part like walls, attachments, and tables are known so simulations can be run with precision before physical trials take place. If any errors occur, changes on the created object or its locations must be made accordingly before the program is used for real-world scenarios.

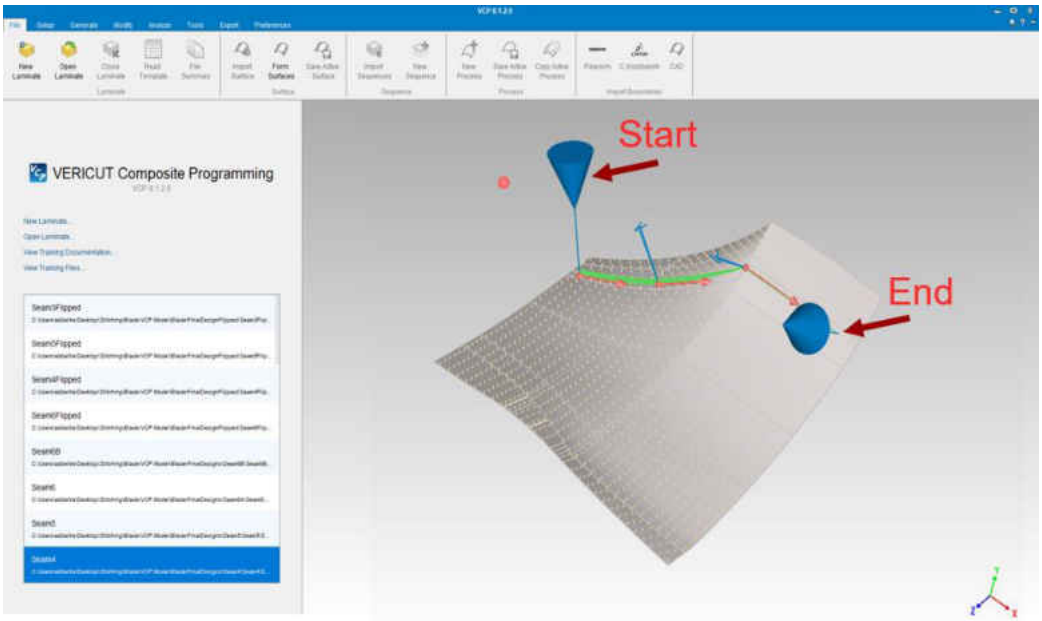

(a)

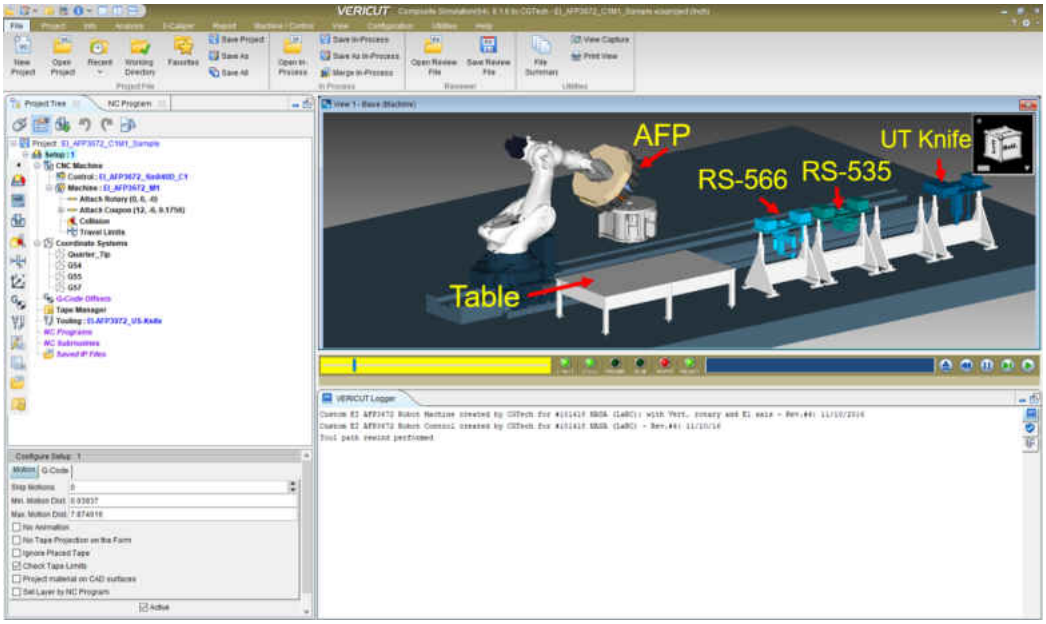

(b)

Figure 3 (a): VCP- Used to Identify Stitching Paths on CAD Surfaces - Start and End Points of uneven Stitch Path

(b): VCS - Used to Simulate Robot Behavior and Identify Possible Errors - ISAAC's Tools and Table used to place Stitch Paths

ISAAC's capabilities of stitching can be integrated by using two different heads, the Single-Sided two needle head (RS-535), Figure 4a, and the Double-Sided single needle head (RS-566), Figure 4b. The RS-535 head can be used for more parts as it is not limited by the length of the underside arm shown in Figure 4b, but one of its current downsides is at the tip where the two needles lie. A part called the Presser Foot is there to keep the fabric from lifting as the needles thread the polyester yarn, and spacings or grooves also need to be present under the fabric to allow for both the catcher and insertion needles to move freely as they stitch on the material. Since the presser foot is flat, if a concave or convex surface is being used, it would not have enough freedom to turn/bend and cover the area properly. The edges of the presser foot would compact the fabric and can also build up wrinkles or bulging sections depending on the movement and pressure exerted. All this could lead to fabric damage before infusion.

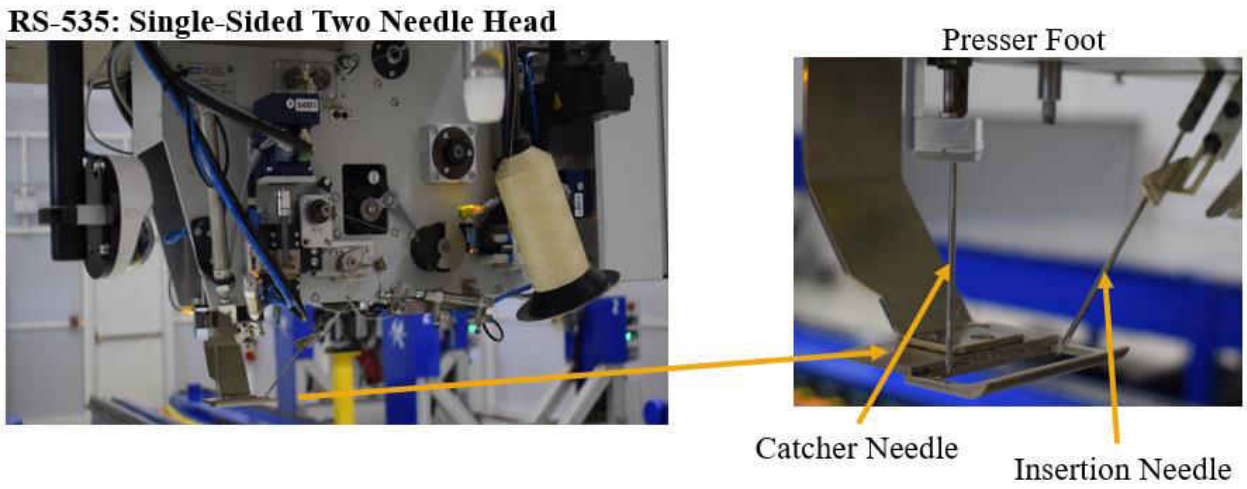

(a)

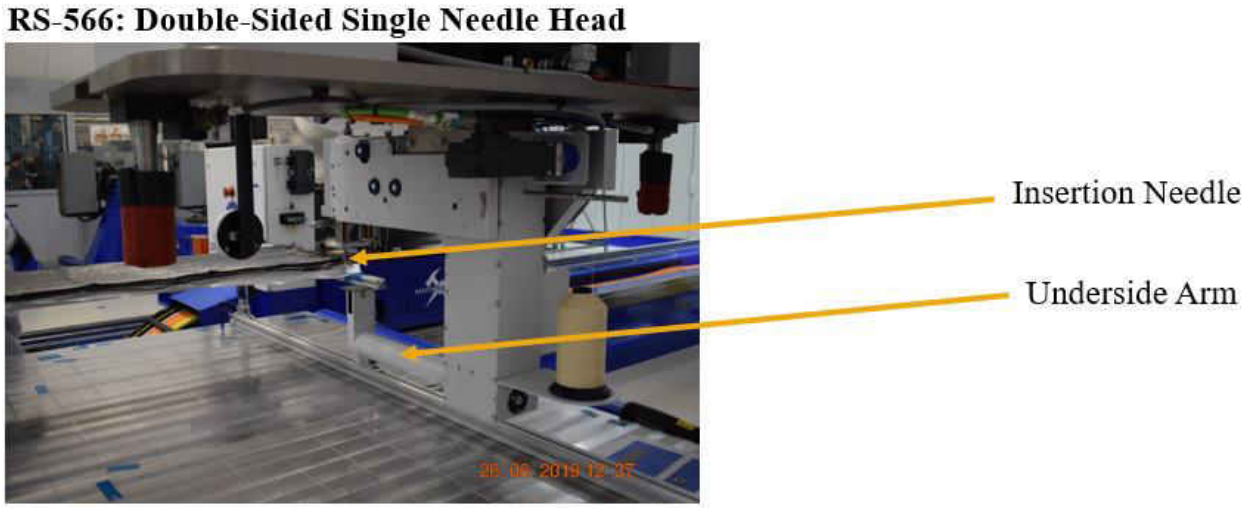

(b)

Figure 4 ISAAC's Stitching Machine Capabilities: RS-535 (a) and RS-566 (b)

Maintaining the dimensional stability of the fabrics is important throughout both the stitching and infusion processes; since parameters such as pressure, viscosity, temperature and fiber permeability which is impacted by fiber deformation, can influence the resin infusion process. Therefore, keeping the fabric as intact as possible during stitching is critical to avoid creating defects that would eventually form into residual stresses, affecting structural strength

and stiffness [20]. Other studies analyzed the difference between stitched and unstitched joints. It was found that stitched joints reduce delamination failure under Mode I loading conditions, while also increasing strength and damage tolerance, unlike the unstitched lap joints which failed through the entire thickness under tensile loads [21]. Even though stitching makes the structure stronger, two studies found strong evidence that all their specimens had fiber damage within the needle penetration areas or created openings, leading to stress concentrations and strip delamination which result in earlier failure initiation cracks [22,23], but that did not stop them from obtaining a 38 percent improvement in maximum static failure load for their single lap joints.

Previous attempts were made to use the original presser foot with uneven surfaces. This concept considered use of the surface geometry of a wind tunnel blade, modify it, and create a model to be 3D printed and used with an RS-535 head. The grooves previously mentioned were added to the surface at desired locations to avoid needle collisions. The final design was also separated into four pieces for easier prints and assembly, Figure 5.

Figure 5 Wind Tunnel Blade Model Created Using CREO Parametric

- Final dimensions are roughly 0.76m by 0.89m with 0.43m at max height

Conducting preliminary runs indicated that modification to the presser foot was required. Even without the dry fabric placed on the tool surface, the edges of the rigid model collided with the plastic surface as shown in Figure 6. For this reason, minimal attempt was made to work with the areas of higher curvature, with only one out of six stitching paths being successful due to the current presser foot configuration.

Figure 6 Presser Foot Collision: (a) 3D Printed Surface to hold Fabric,
(b) Presser foot collision with surface without fabric

In order to develop a stitching piece that is adaptable to an ever-changing surface, certain design parameters need to be considered. A solution such as a non-rigid presser foot configuration would conform to surfaces with varying curvature as previously shown in Figure 6. The design most likely to be successful would be spring loaded, as that is the most versatile way offering easy adaptation to ISAAC's new intended stitching configurations. Manufacturing a new presser foot was the end goal, however, obtaining enough material data from the textile used for stitching is necessary for the design of the new presser foot.

To get enough data from the material commonly used at ISAAC, it was determined that a compaction test, followed by a wrinkling test of the fabric were going to be part of this project's investigation. These two methods of investigation would hopefully provide an insight on the

parameters and limits needed for design of the new presser foot, and with enough information of dry fabrics throughout the reviewed literature, an understanding of the results of each test methodology will consequently also be applied to the design of the new presser foot. Two studies done on the compaction behavior of different textile preforms determined that compaction speed had no effect on wet and dry fabrics and compacted deformation of their samples were dominant after more than one test [24,25].

The two tests developed for this study are both compacting the fabric under different conditions; a purely static compaction test and roller compaction test with fabric pull to create a possibility of wrinkle formation were administered to compare the results to each other. The static compaction test simulates the presser foot approaching the fabric from one direction before applying a force on the fabric, while the wrinkling tests simulates the presser foot being dragged along the surface of the fabric as it stitches curvilinear surfaces. Both tests are meant to be used as an understanding of what transpires when there is contact between the presser foot and the fabric.

2 MATERIALS & METHODS

2.1 Compression Molded Discontinuous Fibers

To understand how the change in platelet size affect the material properties, the Hexcel carbon fiber material was mechanically cut into three groups of platelet lengths: 6.35, 12.7 and 25.4 mm, all have a constant width of 6.35 mm. The span sample of the three-point bending setup was 90 mm, and a width of ~25.4 mm. The thickness of the samples will vary after compression.

For the glass fiber composite, even though there is one constant length of fibers available, the three-point bending span of the test set up was changed to understand the sample size effect on the mechanical properties. Five different spans of 20, 30, 50, 70 & 100 mm were completed to better understand the behavior of the composite as the ratio between thickness and span increase. A 20mm span was selected to induce more fiber breakage; fiber bundles were 25.4 mm in length.

After the compression process was completed by using a Wabash Genesis 75-ton Heat Press, both types of composites samples were cut with a ProtoMAX high performance waterjet cutter built by OMAX Corp. This cutting method minimizes damage or crack formation in the samples. The process of compression molding and testing followed four general steps highlighted in Figure 7.

Figure 7 Compression Molding Process

2.1.1 Compression Mold Design

In order to make a durable tool able to sustain long-lasting constant use in addition to high forces and temperatures, S7 Tool Steel was selected. Its high toughness and strength made it the optimal material for a compression molding tool. The depth of the mold was designed at 25.4 mm, therefore leaving no cavity in between the top and bottom part once combined and giving full compression when a material is in between. Four threaded holes were created on the bottom half, they remained closed during compression and were used with ejector pins to help take samples out of the mold as seen on Figure 8.

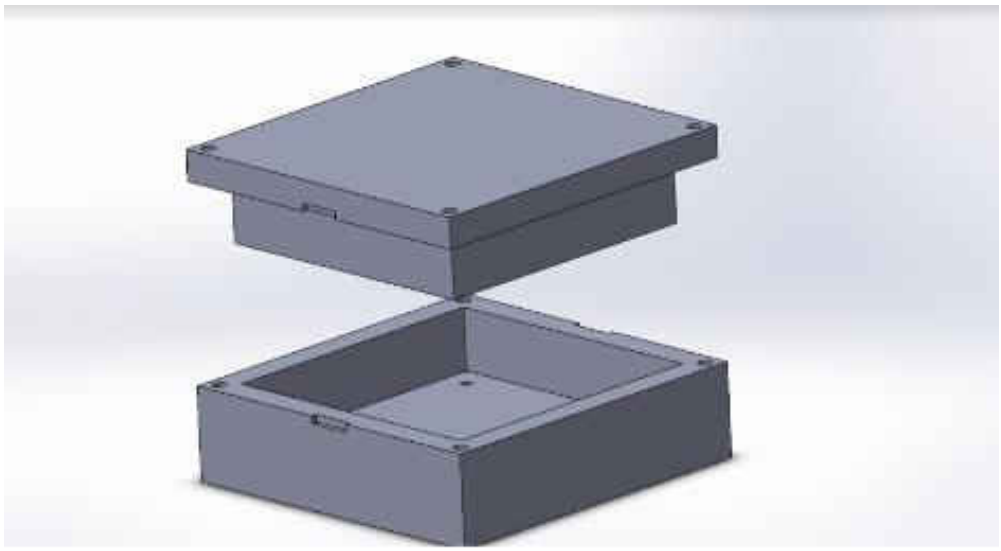

Figure 8 SolidWorks CAD Model for 127x127 mm Mold

Small design changes were made for the final design (Figure 9) to help with handling and an easier detaching between the two halves. Similarly, a 254x254 mm mold (Figure 10) made with the same material and principles was made for the use of the glass fiber organosheets. This would later be used to make bigger panels and get more samples out at once. Due to the difference in weight between the two molds, the bigger mold was carefully handled. All glass fiber panels were made with the big mold.

Figure 9 Final 127x127 mm Mold Design

Figure 10 Final 254x254 mm Mold Design

Another important step to take before each compression occurs is to coat the surfaces with some high temperature release wax obtained from Hexcel (Figure 11). Otherwise the matrix

in the impregnated system will adhere to the metal, resulting in possible damage of the specimen when the ejector pins are used.

Figure 11 Mold Release Wax

2.1.2 Hexcel Carbon Fiber Prepreg Based Molding Compound

The initial fiber material comes wrapped in spools (Figure 12) where the pre-impregnated carbon fiber itself has a rectangular cross-sectional area. The material has a thickness of 0.13 mm with a constant width of 6.35 mm, this is called a fiber tow. All spools are kept in a freezer to maintain its uncured state for longer times and only taken out when needed. A paper cutting board with a titanium blade was used to adequately obtain the desired dimensions of each platelet (Figure 13) until an amount of ~40 grams was gathered; this allows for a final panel

thickness of 1.3-1.5 mm. The cut amount was then placed into the bottom piece of mold and carefully shaken to evenly distribute the platelets and obtain a more uniform, random platelet orientation (Figure 14). Once the mold is closed, it undergoes a modified epoxy matrix curing cycle for monolithic components given by Hexcel's Product Data Sheet [26], temperature ranges will stay as recommended but pressure will be modified to properly compact all the platelets into a flat panel.

Figure 12 HexTow IM7/8552

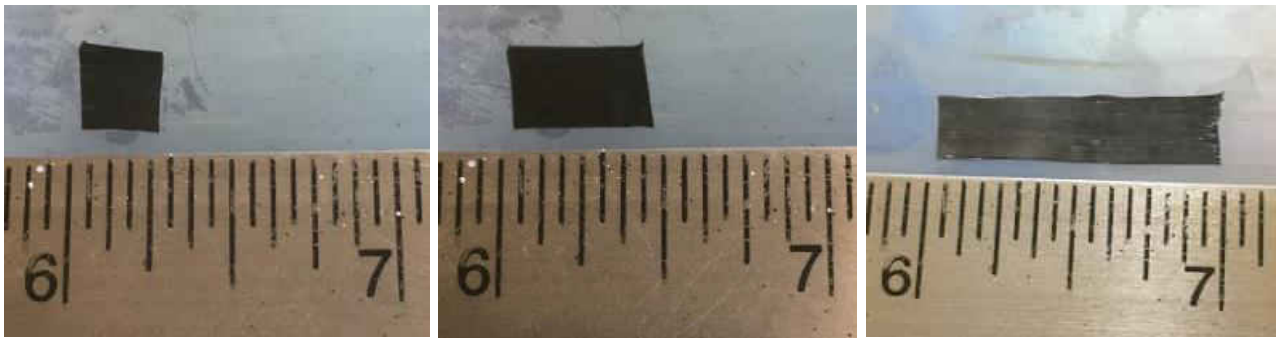

(a) (b) (c)

Figure 13 6.35 mm= ¼ inch (a), 24.7 mm= ½ inch (b), and 25.4 mm= 1-inch (c) Platelets

Figure 14 Uncompressed 25.4 mm Long Platelets

2.1.2.1 Carbon Fiber IM7/8552 Modified Curing Cycle

Preliminary tests were completed before determining that high compression pressures are needed to achieve good consolidation between the fibers and matrix. Cooling of the material is

also meant to be done at a certain rate based on the resin, but no attempt was executed since that capability is not achievable by the heat press.

The following curing cycle for IM7/8552 was used for this experiment:

- Preheat mold at 108 C for 35 mins
- Apply load of 14 MPa or ~25 tons (for 127x127 mm panel) for 30 mins.
- Raise temperature to 180 C for 2 hours, keep same load.
- Let cool down at room temperature.

(a) (b)

Figure 15 Before (a) and After (b) Compression Process for IM7/8552 Thermoplastic

The finished panel (Figure 15) comes out with a glossy surface and a thickness ranging from 1.3-1.5 mm.

2.1.3 Glass Fiber Organosheet Composite

The base material obtained from Johns Manville is a thin flat semi-finished sheet (Figure 16a). Most of the fibers were aligned in the general direction of the line shown and have an ellipsoidal cross-sectional area with a semi-minor and semi-major diameter of 80 and 400 micron, respectively. In order to make samples which can be tested, the thin sheets of ~1.5 mm thick needs to be compacted into a final solid thicker panel that removes the initial porosity in the material system. Therefore, two semi-finished sheets were stacked on top of each other and set to undergo the composites molding. The waterjet was used to cut the material and fit the 254x254 mm mold so they can be stacked on top of one another.

2.1.3.1 Glass Fiber Organosheet Curing Cycle

This curing cycle does not need a transition of different temperature levels throughout the process. The only requirement is to obtain a temperature higher than melting point of nylon (220C). Molding pressure was increased with slow intervals, followed by an extra step of the same applied force for better final compaction.

The following curing cycle for Glass Fiber-Nylon 6 was used for this experiment:

- Reach temp of 230 C.
- Apply load of 0.7 MPa or ~5 tons (for 254x254 mm panel), steps of 1 ton every 30 secs.
- Leave under heat press for 15-20 mins.
- Turn temperature off, leave pressure on for 25-30 mins.

- Let cool down at room temperature.

(a) (b)

Figure 16 Before (a) and After (b) Compaction Process for Johns Manville Thermoplastic

The finished panel (Figure 16b) comes out with a smooth surface and a thickness ranging from 2.4-2.7 mm.

2.2 Non-crimp Fabric Configuration

The non-crimp fabric (NCF) material used in this work has Saertex multiaxial non-crimp fabrics provided from NASA Langley Research Center, with a laminate layup configuration of [+45/-45/0/90/0/-45/+45]. Each carbon fabric and layer was held together by a polymer thread applied through a warp knitting process. This thread was used to hold the dry fibers in place during preform fabrication and not intended to carry structural loads, as opposed to stitching or

sewing with Vectran threads, which are intended to join layers together and support structural loads after resin infusion to form the final product. The fiber layout configuration can be custom made to order, as shown on Figure 17.

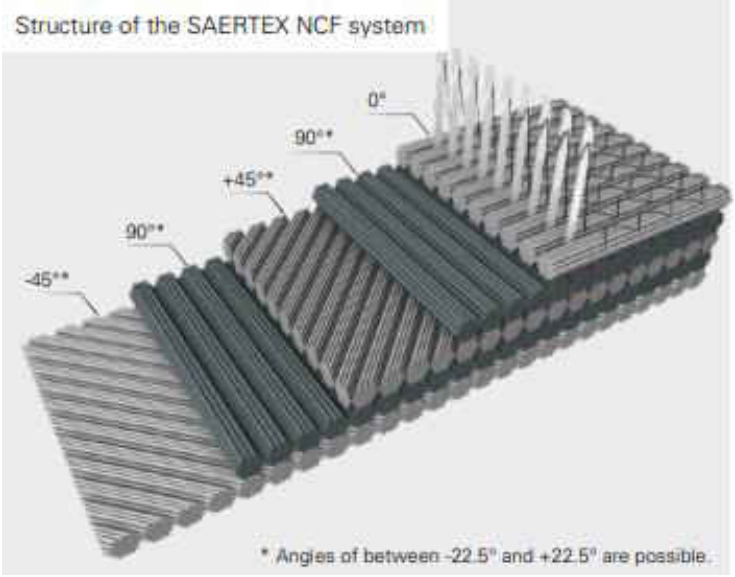

Figure 17 Basic Construction of a Woven Non-crimp Textile

- Obtained from SAERTEXs flyer of multiaxial fabrics

2.2.1 Compaction of Non-crimp Fabric Test

The compaction test considered the following variables: thickness, sample dimension, compaction speed, and testing cycles. Initial and final thickness may be the most important ones, considering that having compacted regions on the fabric prior to resin infusion could result in flaws and defects during or after curing. Resin infusion behaviors were shown to change when

the fabric is deformed, since resin flow pattern and flow rates change depending on fiber direction and spacing in between [27]. Dry region may follow due to low permeability and increased local fiber volume fraction. The initial fabric is about 2 mm thick; therefore, total thicknesses of 4 mm and 8 mm, two and four layers of fabric respectively were considered in these tests to analyze how the compaction is affected by total laminate thickness. ISAAC can be configured to stitch woven fabrics of up to 51 mm thick, but there has been no need to reach those dimensions and these thicknesses are the most frequently used for stitching at NASA Langley

The two other dimensions chosen for this experiment were squares of ~152x152 mm and 229x229 mm. This approach explored the idea of how fabric area changes the results. Compaction zones closer to the edges of the material can result in different behavior as compared to locations farther away from edges. These two sizes were also chosen due to limited material, and with a total area ratio of 2.25 between the two, both results would be enough to show a difference, if any.

The speed at which the presser foot approaches the fabric is yet another factor to consider. The machine can operate at different speeds throughout its movement of approaching the surface or turning to go in a different direction along it. Therefore, three different approach speeds of 1, 2 and 5 mm/min were applied to each sample.

Finally, each sample was set to undergo three different compaction cycles. This variation was considered to observe how repeated loading and varying compaction approaches affected the overall residual deformation of the fabric due to nesting of fiber tows. With all these parameters taken into consideration, as shown in the following Table 1, a total of 36 tests were conducted for this type of non-crimp fiber.

Table 1 Compaction Test Layout

Parameters	**Units**
Thickness	4 and 8 mm
Sample Dimensions	152x152 and 229x229 mm
Compaction Speeds	1, 2 and 5 mm/min
Testing Cycles	1-3

2.2.1.1 Non-crimp Fabric Compaction Test Setup

The non-crimp fabric was measured, marked, and then cut using an electric fabric cutter. Two groups of 18 pieces with dimension of 152x152 mm and 229x229 mm were cut and combined into six samples for both dimensions: three of them with two fabric laminate, and the other three with four, as shown on the following Figure 18. Each sample for both dimensions were numbered 1-6; with samples 1-3 having two laminates, and samples 4-6 having four laminates. The 229x229 mm specimens were referred as "*Big Sample #*" to help identify and compare them throughout this project. Finally, they were secured with masking tape to properly handle them and prevent sliding of the fabric during tests.

(a) (b) (c)

Figure 18 152x152 mm cut Samples

- Samples on the left and right side of pictures (b) & (c) have 2 and 4 laminate respectively

Once both types of samples were ready, they were tested using a Tinius Olsen Tension & Compression machine, with a load cell capacity of 10kN. The fixtures used for this experiment were two circular metal plates. The bottom had a diameter of 147.32 mm which was used to lay down the material while being compacted. The top fixture has a diameter of 48.26 mm, and its area was used to obtain pressure calculations. Before each sample was tested, a Mitutoyo Electronic Caliper was used to measure the overall thickness of each sample before compaction. Four random locations were chosen for thickness measurements to obtain an estimate of the thickness of every sample. The 152x152 mm samples, 1-3, had an average thickness of 3.94 mm, and samples 4-6 had an average thickness of 8.08 mm. Similarly, the big samples had an overall

average thickness of 4.00 mm and 8.18 mm for big samples 1-3 and 4-6, respectively, as shown in Table 2.

Table 2 152x152 mm Samples (a), and 229x229 mm Big Samples (b) Average Thicknesses

152x152 mm Samples		
	Avg Thickness (mm)	**Overall Avg Thickness (mm)**
Sample 1	3.87	3.95
Sample 2	3.97	
Sample 3	4.02	
Sample 4	8.09	8.08
Sample 5	8.02	
Sample 6	8.12	

(a)

229x229 mm Big Samples		
	Avg Thickness (mm)	**Overall Avg Thickness (mm)**
Sample 1	3.91	4.00
Sample 2	4.01	
Sample 3	4.09	
Sample 4	8.2	8.18
Sample 5	8.14	
Sample 6	8.19	

(b)

Data during compaction test were recorded at 10 Hz frequency. The top fixture was manually lowered until it contacted the top surface of each sample. The crosshead was stopped when it recorded a force between +0.01 and +1 N, and then displacement and force readings adjusted so that all tests started at zero load and displacement.

During fabric compaction, the initial fiber tow configurations begin to deform excessively, this is described as nesting. The compaction curve demonstrates the following distinctive regions: a linear behavior, then a nonlinear exponential curve develops when nesting of fiber tows occurs, followed by another linear behavior with a significantly increased slope due to densification of the fiber bed. Lower displacement speeds demonstrated similar compaction behavior. Before a new cycle on the same sample started, the machine was moved back to the original preset position, Figure 19-20.

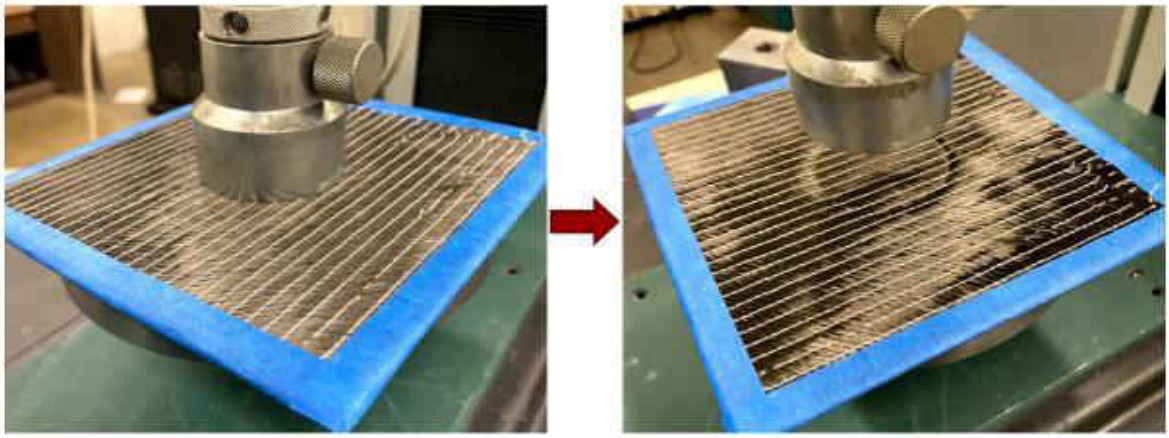

Figure 19 152x152 mm Compacted Sample

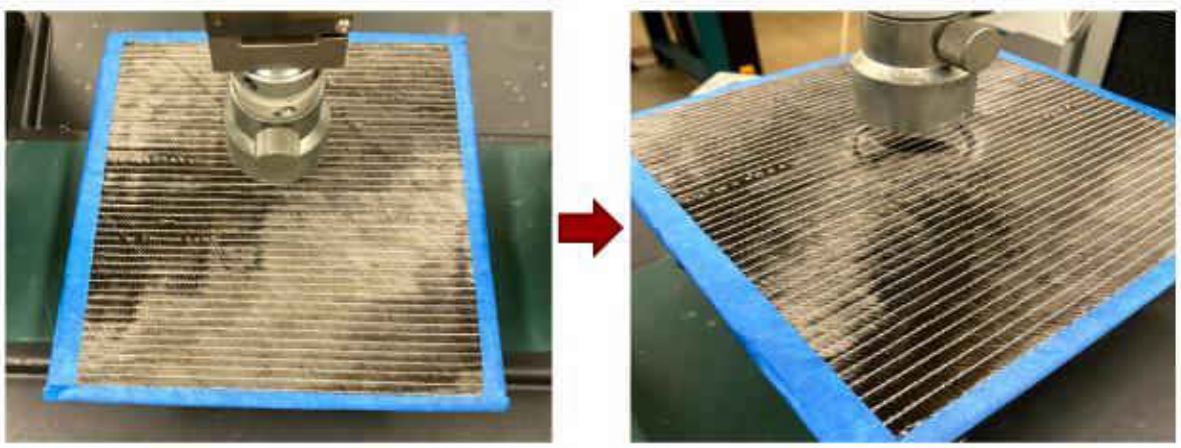

Figure 20 229x229 mm Compacted Sample

The fixture used for the wrinkling tests, Figure 22, was also used for a purely compaction test on two selected samples. This compaction test was used to compare the results based on the change in geometry of the fixture.

Once all compaction tests were completed, the representative fabric samples were scanned using a Leica DM6-M Material Microscope, Figure 21, to scan the surface at different positions and detect changes in surface topology between the compacted and uncompacted regions.

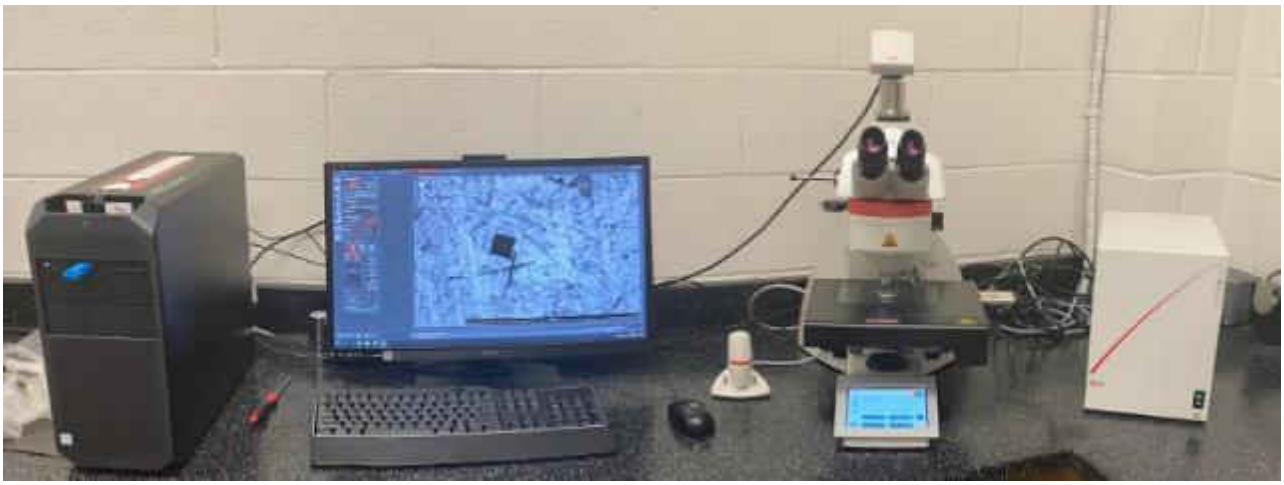

Figure 21 Leica DM6-M Microscope

2.2.2 Wrinkling of Non-crimp Fabric

When stitching takes place, the front side of the presser foot can come in contact with the fabric, which will conform to the curvilinear shape of the presser foot.

Therefore, a test method was developed to recreate such behavior. Using the Tinus Olsen machine, the control parameters such as displacement and speed were modified to accommodate with new compaction movements while the machine recorded load data. The crosshead moved at a slow rate of 1 mm/min until a set amount of distance until forces of about 50, 100, and 150 N are constantly being output. The roller fixture, Figure 22, with a diameter of 5 mm was used to apply compressive forces representative of the different regions in the corresponding compaction tests. The wrinkling test was conducted by pulling the non-crimp fabric as the roller contacts the surface.

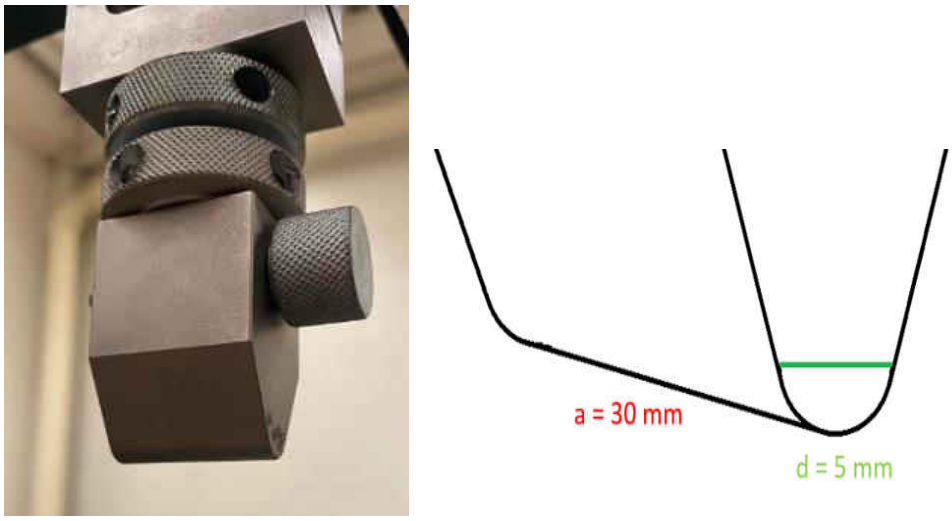

Figure 22 Roller Fixture for Wrinkling Test

2.2.2.1 Wrinkling Test Setup

Two samples from the big samples (229x229 mm) non-crimp fabric group were selected for this test due to their larger workable areas, one from the 4 mm thick samples and one from the 8mm. Each sample was placed on the flat plates to keep the fabric in place. However, said fabric was attached to an acquired manual winch able to pull the sample sideways at a slow controlled speed, therefore a testing fixture was created using a thin metal steel sheet, three thin metal rods, and some 310 A/B Epoxy adhesive. Figures 23-25 show what the designed fixture looks like after it has been cut with the Waterjet and assembled. This fixture was used to clamp the sample into the fixture with the help of the teeth-like grips that were tightly secured with screws and nuts. The hook of the winch was finally attached to the fixture holes while it is being pulled.

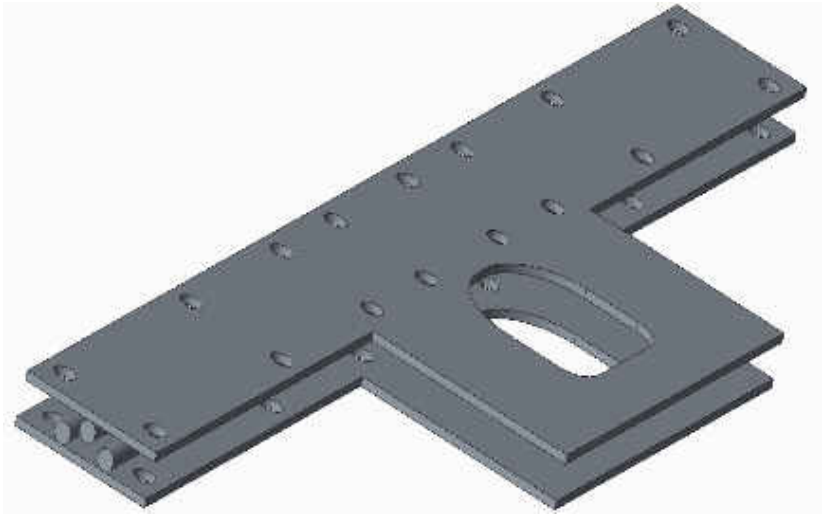

Figure 23 Custom Made Wrinkling Testing Fixture CAD Model

Figure 24 Wrinkling Fixture Water Cutting Process

Figure 25 Wrinkling Fixture Assembly

A small trial was performed with spare twill fiberglass cloth to ensure the testing set up worked accordingly as shown, Figure 26.

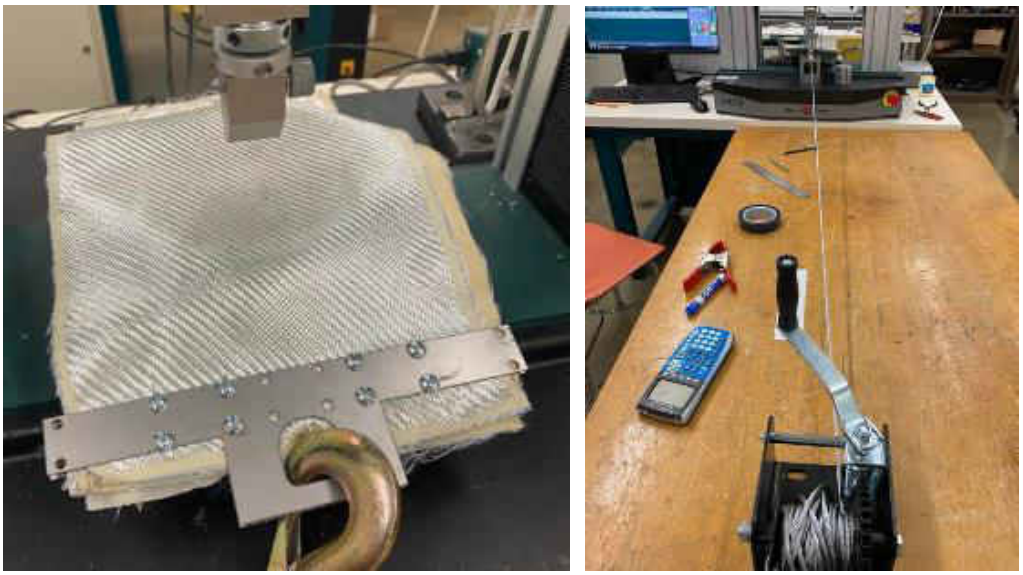

Figure 26 Wrinkling Test Trial

The glass fiber was pulled a distance between 25-50 mm until a small bulging surface started to develop on the back side of the crosshead. Thus, our DIC camera was set on to back of the machine to record any lumps growing and have a visual portrayal to analyze while the fabric was being pulled. No calibrations were done to the camera since the purpose was to record our findings. When implementing the non-crimp fibers, the fixture was dropped to the desired load reading and the pulling of the samples with the winch began, reading the changes in force over time while a video was recorded simultaneously. This trial would give an overall performance of the thin and thick samples under the created loaded constraints. Figure 27 shows the three pulling set ups the two samples were subjected to. The grip center changed accordingly to properly accommodate to the cable direction.

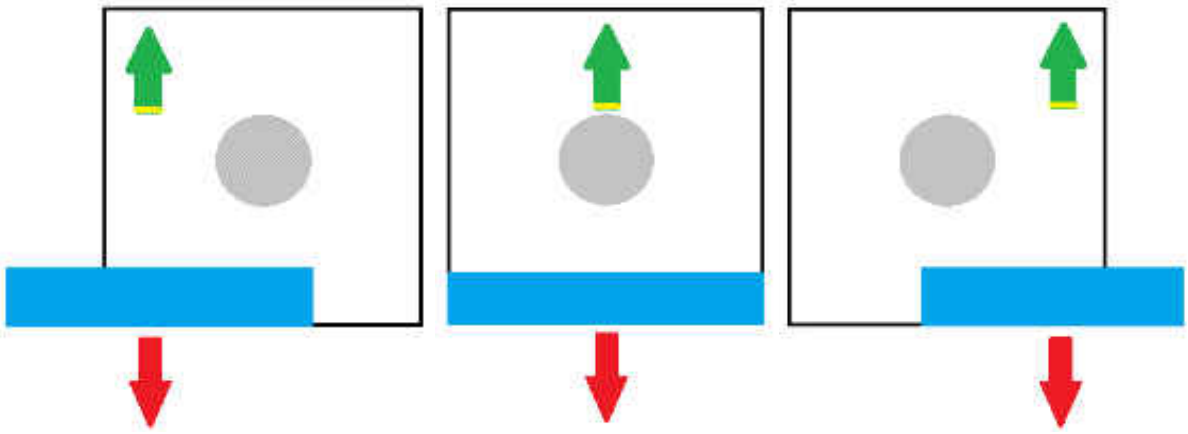

Figure 27 Wrinkling Test Pulling Directions

3 MATERIAL PROPERTIES CALCULATIONS

3.1 Compression Molded Discontinuous Fibers

Flexural response of a material was used to assess the general properties of a structure. It can be used to obtain estimates for compressive, shear, and tensile tests while also requiring less preparation and time, making it the cheaper alternative. When loading takes place, the top surface of the specimen was subjected to compressive loads while the bottom was under tension. Therefore, the stress along the span (normal stress) cancels out at the midplane of the specimen balanced by a linear distribution. Shear stress behaves in an opposite manner, where it is directly proportional to the applied load and is maximum at the midplane between the top and bottom sections of the rectangular sample. Stress is also dependent on higher span length-to-thickness ratio (*L/h*), where shear is more dominant with small ratios. The equations used follow the ASTM standards for three-point bending tests. Flexural strength, modulus, and strain were calculated using Eq. 1, Eq. 2 and Eq 3.

$$\sigma = \frac{3FL}{2wh^2} \qquad \text{(Equation 1)}$$

$$E_f = \frac{L^3}{4wh^3}\frac{\Delta F}{\Delta \delta} \qquad \text{(Equation 2)}$$

$$\varepsilon_f = \frac{6Dh}{L^2} \qquad \text{(Equation 3)}$$

where *F* is load (force) at fracture point, *L* is the distance of the span, *w* is the width of the sample, *h* is the thickness of the sample, $\frac{\Delta F}{\Delta \delta}$ is the plot of load vs deflection (slope), and *D* is the maximum deflection at center of the span.

3.2 Non-crimp Fabric

For pure compaction tests, the new fiber volume fraction was calculated and compared to the uncompacted fiber volume fraction of the fabric based on the measured average thicknesses for both the 4 mm and 8 mm big samples back on Table 2. The following equation is:

$$V_f = \frac{\rho_a n}{\rho_f T} \qquad \text{(Equation 4)}$$

where ρ_a is the areal density of the fabric, n is the number of the laminate in the sample, ρ_f is the density of the specific fiber, and T is the thickness of the sample.

ρ_a = 1425 g/m^2

ρ_f = 1.79*10^6 g/m^3

4 EXPERIMENTAL RESULTS

4.1 Compression Molded Discontinuous Fibers

All experimental results were grouped into four different types of data visualization: Stress-strain graphs, data tables for modulus and maximum flexural strength, bar charts, and box and whiskers plots. MATLAB was used to help group and graph data from Excel, which minimized the likelihood of error in combining thousands of data points with Excel alone. Lastly, a Design of Experiments (DoE) approach was implemented to a portion of this analysis. A software called Design-Expert (DX) was used for performing the regression analysis.

4.1.1 Carbon Fiber Compression Molded Compound

The IM7/8552 stress-strain graphs illustrate a significant difference in maximum stress as the platelet length increases. Where the 6.35 mm long platelet samples (Figure 28a) act in a more isotropic manner with the lowest coefficient of variance, Figure 29a. The 25.4 mm long platelet samples vary greatly per test, where strength was sometimes found to be over twice as much as the 6.35 mm long fibers, and in other cases it gave similarly values (Figure 28c).

Due to the increasing aspect ratio of the platelets, load transfer between individual platelets improves mechanical properties. However, number of platelets per sample decrease as the aspect ratio increase, resulting in a more non-uniform local platelet orientation. Regions of platelet orientation transverse to the applied load result in early failure and reduced strength for the 25.4 mm long platelet samples. The 12.7 mm long platelet samples can be presumed to be the intermediate between the three dimensions, where the results appear to behave like both 6.35 and 25.4 mm long fibers.

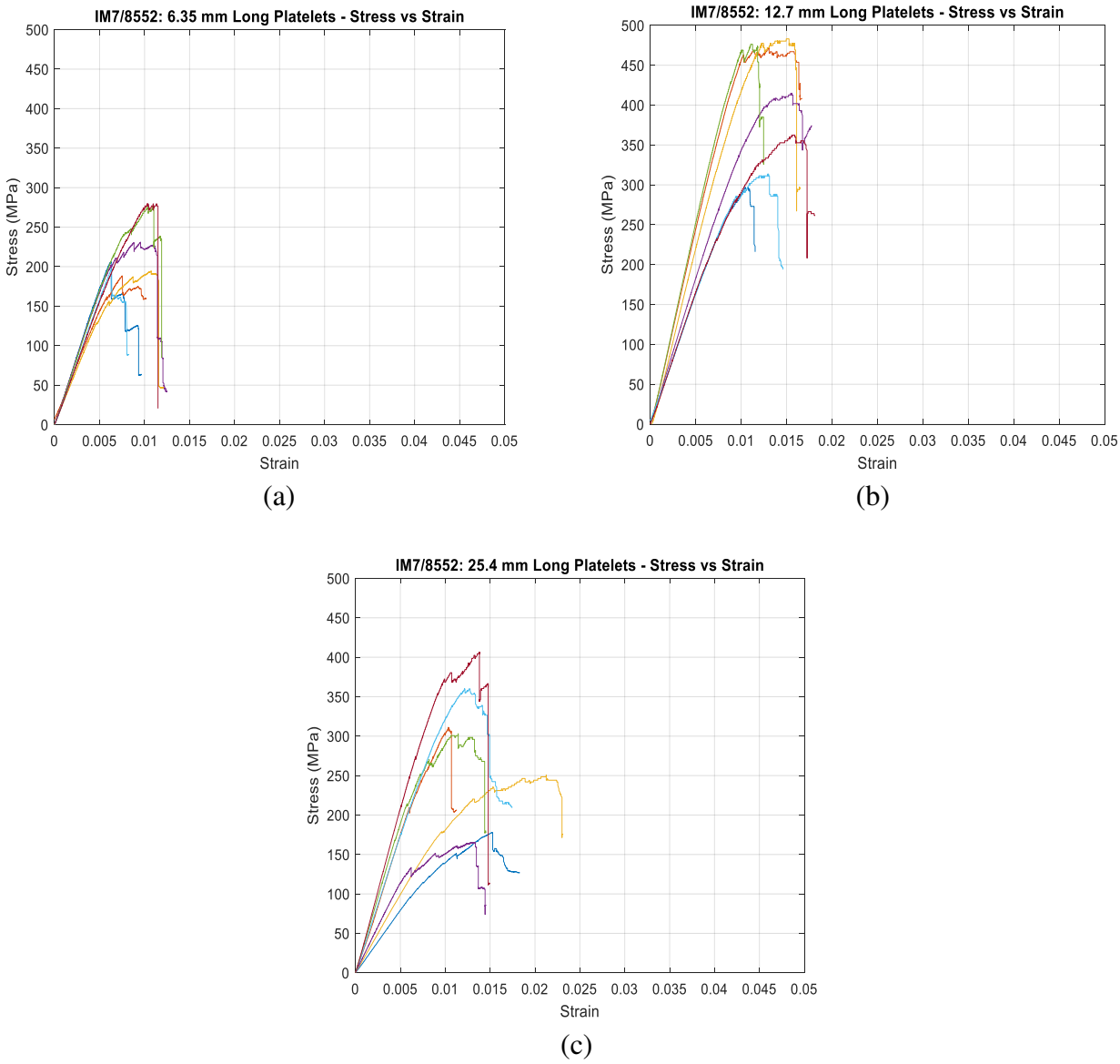

Figure 28 IM7/8552: 6.35 mm (a), 12.7 mm (b), and 25.4 mm (c) Flexural Stress-Strain Curves

The high length to thickness ratio seen in Figure 29 indicates that mostly tensile loads and compressive stresses are present rather than shear forces.

Hexcel Prepreg IM7/8552								
Strength (Mpa)	Span Ratio	90mm Span Samples						
		1	2	3	4	5	6	7
6.35 mm Platelets	63	206.27	188.28	194.23	231.05	275.05	198.02	279.40
12.7 mm Platelets	59	297.21	472.73	483.04	414.92	476.30	313.52	362.41
25.4 mm Platelets	57	177.85	311.09	250.65	165.34	302.98	359.97	406.42

IM7/8552		
Mean Strength (MPa)	Std Dev (Mpa)	CV (%)
224.61	38.46	17.12
402.88	79.19	19.66
282.04	89.71	31.81

(a)

Hexcel Prepreg IM7/8552								
Modulus (Gpa)	Span Ratio	90 mm Span Samples						
		1	2	3	4	5	6	7
6.35 mm Platelets	63	35.19	27.68	27.81	33.61	34.50	31.84	31.38
12.7 mm Platelets	59	32.90	49.80	46.70	36.73	51.53	32.05	33.05
25.4 mm Platelets	57	31.95	34.08	38.07	22.90	37.92	34.33	41.57

IM7/8552		
Mean Modulus (GPa)	Std Dev (GPa)	CV (%)
31.72	3.03	9.55
40.40	8.62	21.33
34.40	6.00	17.43

(b)

Figure 29 IM7/8552: Flexural Strength (a), Modulus (b) Raw Calculated Data

The bar charts (Figure 30) display the flexural strength and modulus calculated data side by side; where both material properties do show more isotropy for shorter fiber lengths but disperse a lot more when they are longer. The graphs in Figure 31 display the non-linear trend between the three platelet dimensions, with the 12.7 mm long platelets being the highest overall results and coefficient of variance increasing as the platelet aspect ratio increases.

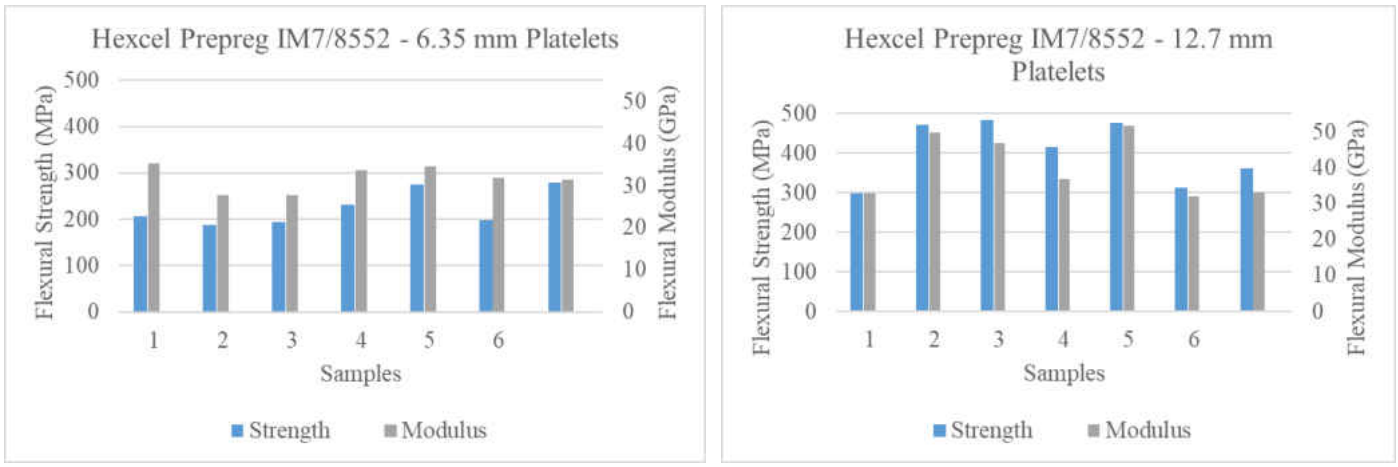

(a) (b)

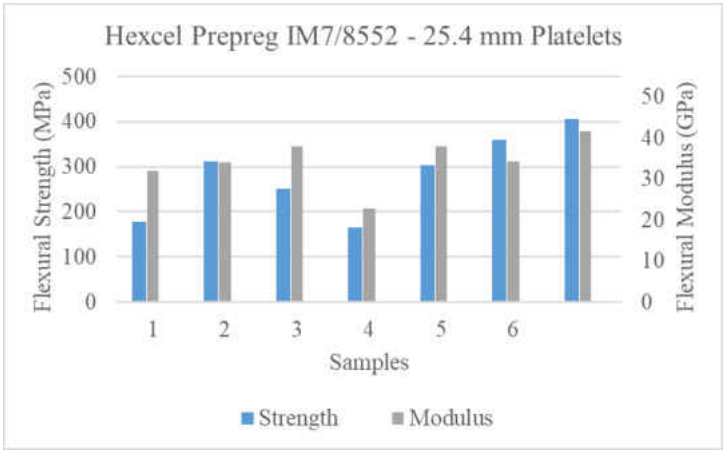

(c)

Figure 30 IM7/8552: 6.35 mm (a), 12.7 mm (b), and 25.4 mm (c) Calculated Data Bar Charts

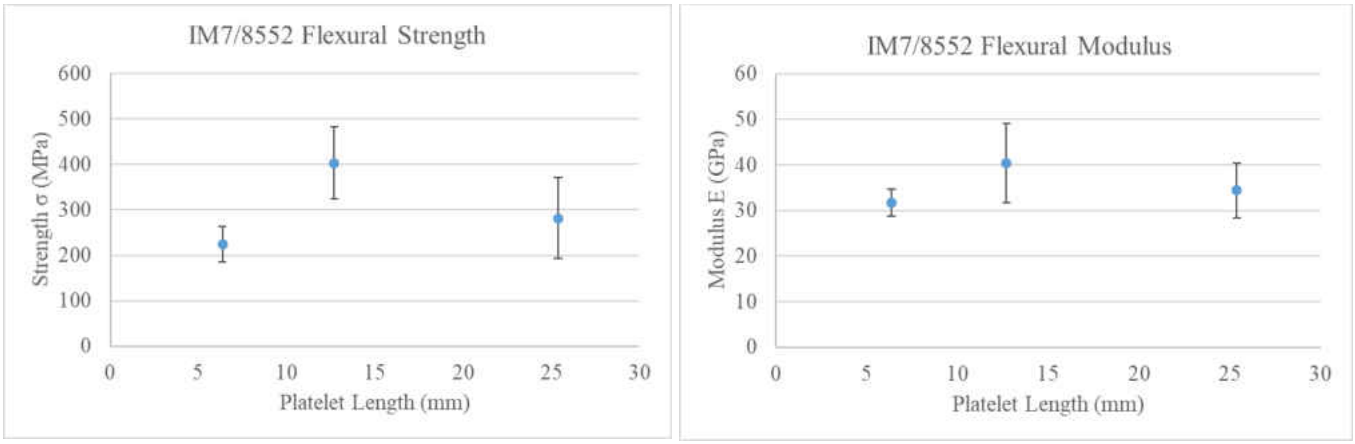

(a) (b)

Figure 31 IM7/8552: Flexural Strength (a), Modulus (b) Calculated Data with Error Bar Graphs

4.1.2 Glass Fiber Organosheet Composite

The results for the glass fiber composites showed a more uniform mechanical behavior for each test group, which can be explained by the small fiber bundle volume of 0.64 mm^2 and helping with the more uniform bundle orientation. When comparing the biased and unbiased direction of the organosheet, a difference in flexural properties were observed, which is indicative of a preferred bundle orientation along the biased direction. Both types of directions appear to behave in the same manner for flexural strength, even though their average results are not the same. However, this cannot be said for flexural modulus, where the results for the biased direction reached its maximum at a span of 50 mm, or a ratio of 18. On the other hand, the flexural modulus for the unbiased samples continuously increased as the span to thickness ratio increased.

4.1.2.1 Biased Glass Fiber Direction

A span of 20 mm (Figure 32a) appears to give fairly constant and high values, where 30mm results (Figure 32b) range the most amongst all five different spans. A decreasing trend can be observed as the spans increases, but it can be currently assumed that each sample was not far off from their average results (Figure 33).

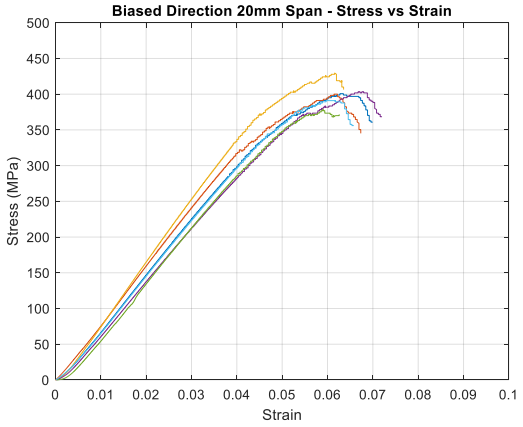

(a)

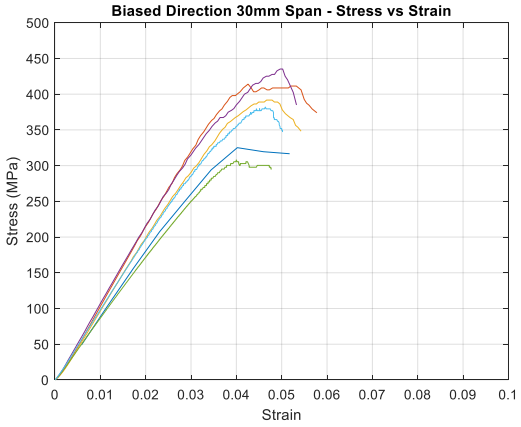

(b)

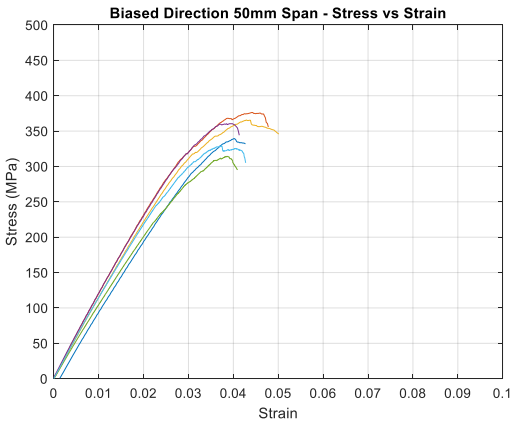

(c)

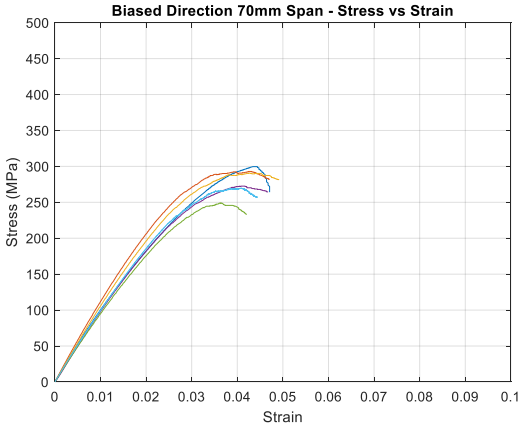

(d)

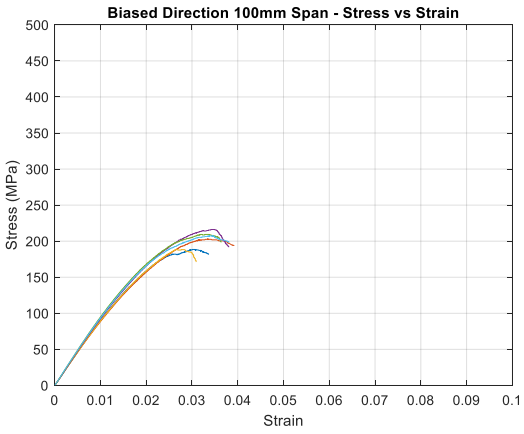

(e)

Figure 32 Glass Fiber Biased Direction: 20 mm Span (a), 30 mm Span (b), 50 mm Span (c), 70 mm Span (d), and 100 mm Span Flexural Stress-Strain Curves

Glass Fiber - Biased Direction							
Strength (MPa)	Span Ratio	Sample					
		1	2	3	4	5	6
20mm Span	8	400.70	400.02	429.58	403.45	378.59	390.99
30mm Span	11	325.12	414.05	391.73	435.22	308.01	381.95
50mm Span	18	339.31	376.23	365.71	360.42	314.22	329.10
70mm Span	26	299.65	292.96	290.77	272.52	249.17	269.73
100mm Span	33	188.53	203.26	188.31	216.22	209.32	207.32

Glass Fiber - Biased Direction		
Mean Strength (Mpa)	Std Dev (Mpa)	CV (%)
400.55	16.88	4.21
376.01	49.90	13.27
347.50	23.82	6.85
279.13	18.85	6.75
202.16	11.44	5.66

(a)

Glass Fiber - Biased Direction							
Modulus (GPa)	Span Ratio	Sample					
		1	2	3	4	5	6
20mm Span	8	7.65	8.11	8.79	7.26	7.75	7.74
30mm Span	11	7.42	10.52	9.55	10.43	8.28	9.48
50mm Span	18	9.93	10.83	10.47	10.82	9.82	10.62
70mm Span	26	8.43	9.47	9.09	8.98	8.65	9.30
100mm Span	33	8.81	8.45	8.52	8.91	9.08	8.89

Glass Fiber - Biased Direction		
Mean Modulus (Gpa)	Std Dev (Gpa)	CV (%)
7.88	0.52	6.61
9.28	1.22	13.15
10.41	0.44	4.21
8.99	0.39	4.35
8.78	0.24	2.75

(b)

Figure 33 Glass Fiber Biased Direction: Flexural Strength (a), Modulus (b) Raw Calculated Data

The bar chart show that values once again fall within close ranges of one another, with only the 30 mm span (Figure 34b) showing more variability from the rest.

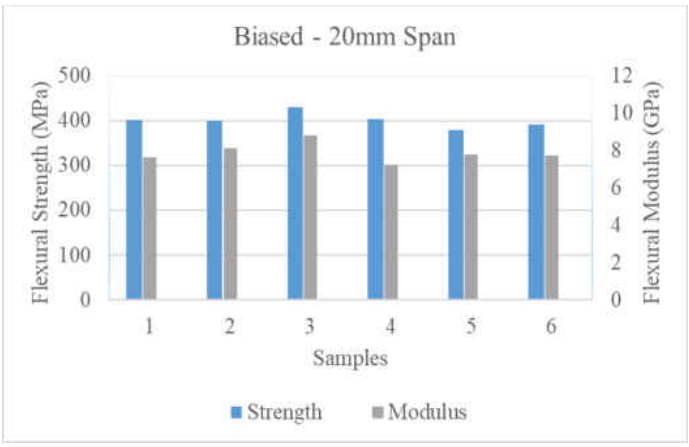

(a)

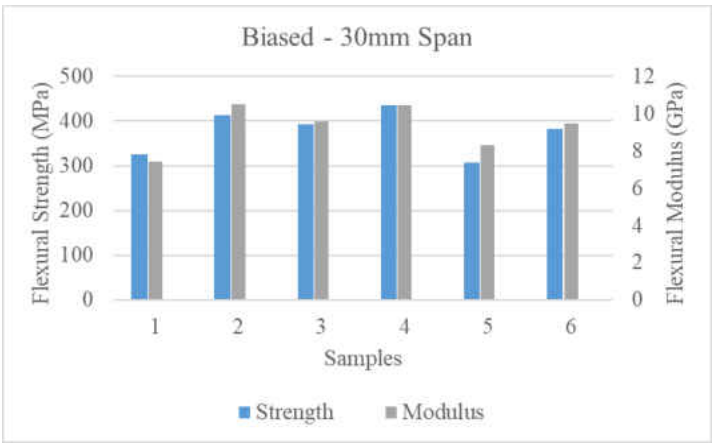

(b)

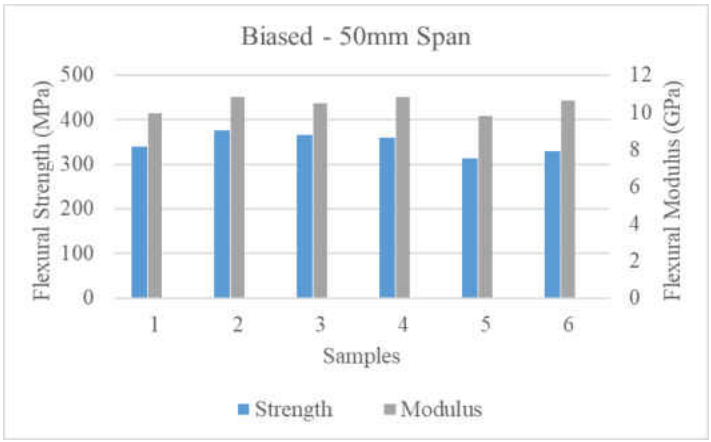

(c)

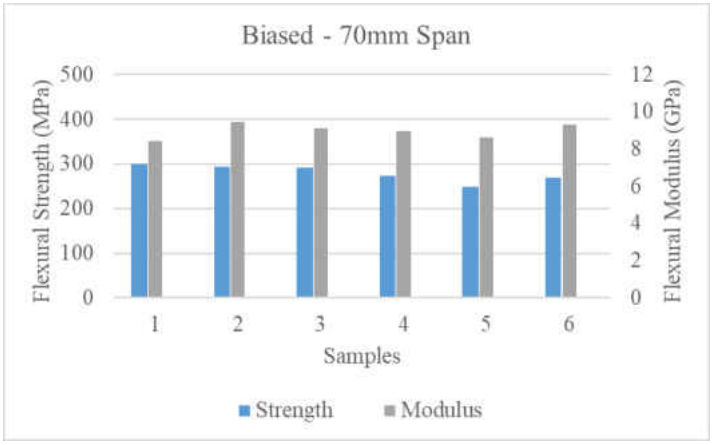

(d)

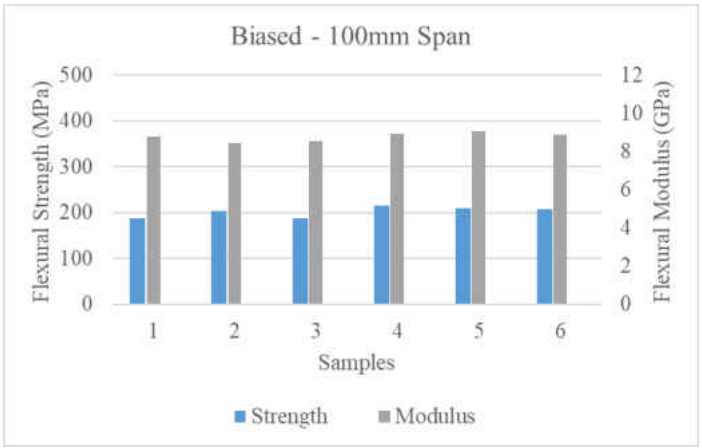

(e)

Figure 34 Glass Fiber Biased Direction: 20 mm Span (a), 30 mm Span (b), 50 mm Span (c), 70 mm Span (d), and 100 mm Span Calculated Data Bar Charts

The error bar graphs show what trend in material properties we can expect as we increase the span, with strength decreasing (Figure 35a) and modulus topping at a length to span ratio of 18 as shown in Figure 35b.

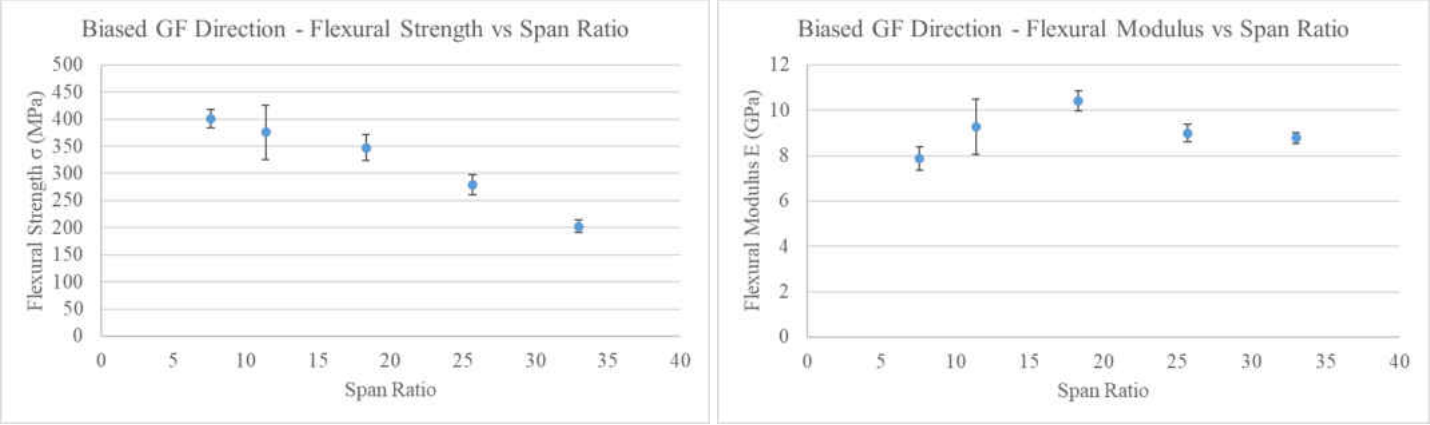

(a) (b)

Figure 35 Glass Fiber Biased Direction: Flexural Strength (a), Modulus (b) Calculated Data with Error Bar Graphs

4.1.2.2 Unbiased Glass Fiber Direction

Flexural behavior for the unbiased direction showed similar performance for the 20 mm span with a low length to thickness ratio showing the highest flexural modulus from all the group of samples, but their coefficinet of variance is not constant as the biased samples. Longer spans are more consistent with their results after a ratio of 19 was achieved.

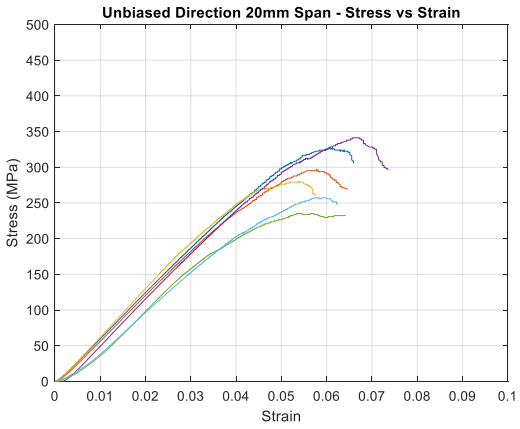

(c)

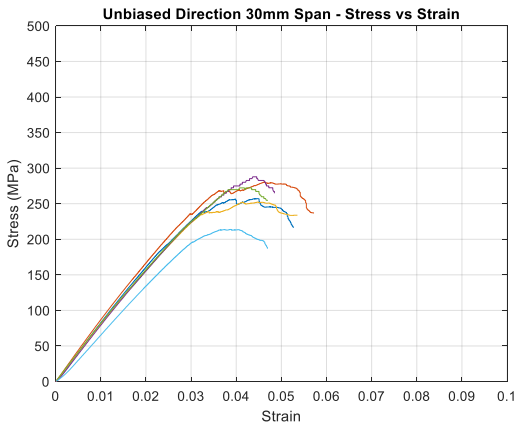

(d)

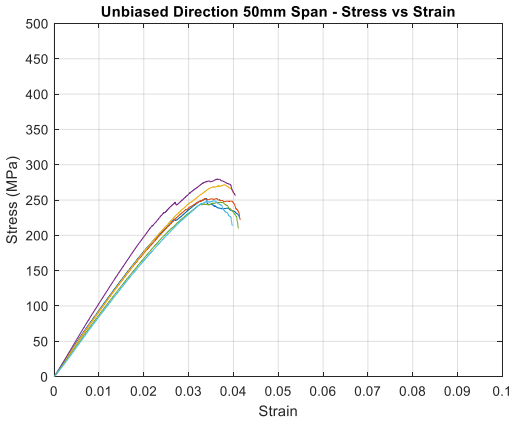

(c)

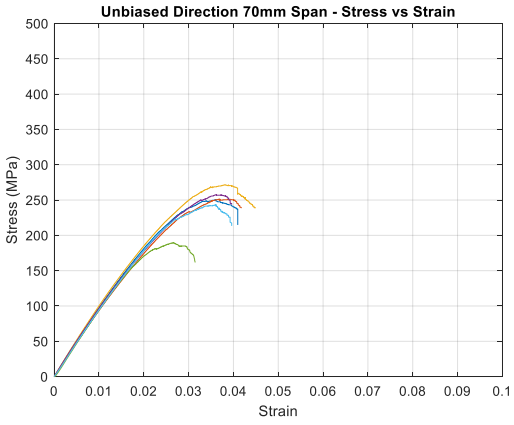

(d)

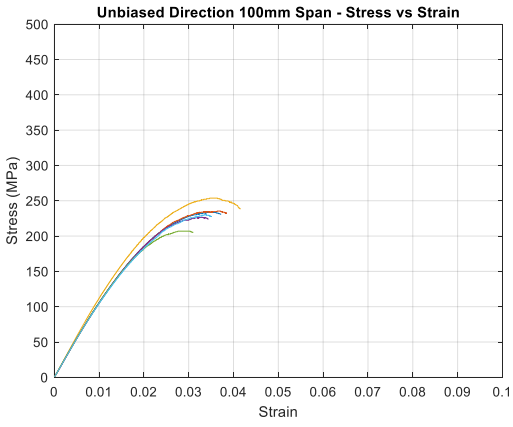

(e)

Figure 36 Glass Fiber Unbiased Direction: 20 mm Span (a), 30 mm Span (b), 50 mm Span (c), 70 mm Span (d), and 100 mm Span Flexural Stress-Strain Curves

Glass Fiber - Unbiased Direction							
Strength (Mpa)	Span Ratio	Sample					
		1	2	3	4	5	6
20mm Span	7	327.15	296.71	280.65	341.23	235.18	257.43
30mm Span	11	257.07	280.61	252.27	287.84	272.26	213.89
50mm Span	19	252.01	252.08	271.71	279.73	247.08	248.89
70mm Span	25	250.68	251.49	271.56	257.38	189.81	242.95
100mm Span	37	233.44	235.38	253.70	226.38	206.91	230.28

Glass Fiber - Unbiased Direction		
Mean Strength (MPa)	Std Dev (MPa)	CV (%)
289.72	40.50	13.98
260.66	26.61	10.21
258.58	13.65	5.28
243.98	28.20	11.56
231.02	15.12	6.54

(a)

Glass Fiber - Unbiased Direction							
Modulus (GPa)	Span Ratio	Sample					
		1	2	3	4	5	6
20mm Span	7	6.36	6.27	6.58	6.46	5.86	5.51
30mm Span	11	8.05	8.03	7.53	7.63	7.51	6.62
50mm Span	19	8.75	8.51	8.76	9.86	8.31	8.19
70mm Span	25	9.35	8.40	9.29	8.89	9.33	9.14
100mm Span	37	10.24	10.12	10.84	10.17	10.13	10.12

Glass Fiber - Unbiased Direction		
Mean Modulus (Gpa)	Std Dev (GPa)	CV (%)
6.17	0.40	6.55
7.56	0.52	6.88
8.73	0.60	6.88
9.07	0.37	4.09
10.27	0.28	2.76

(b)

Figure 37 Glass Fiber Unbiased Direction: Flexural Strength (a), Modulus (b) Raw Calculated Data

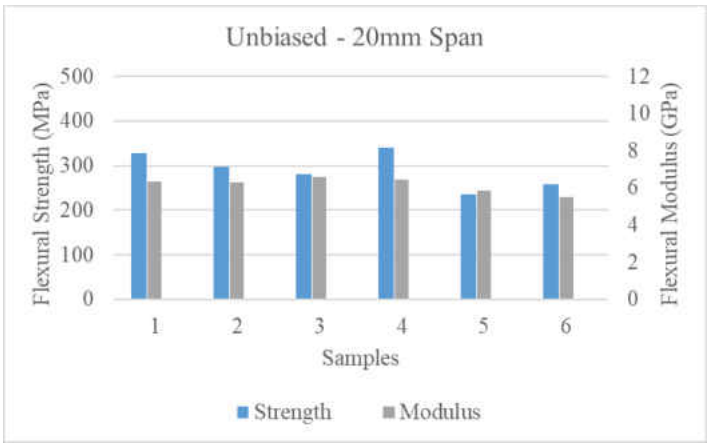

(a)

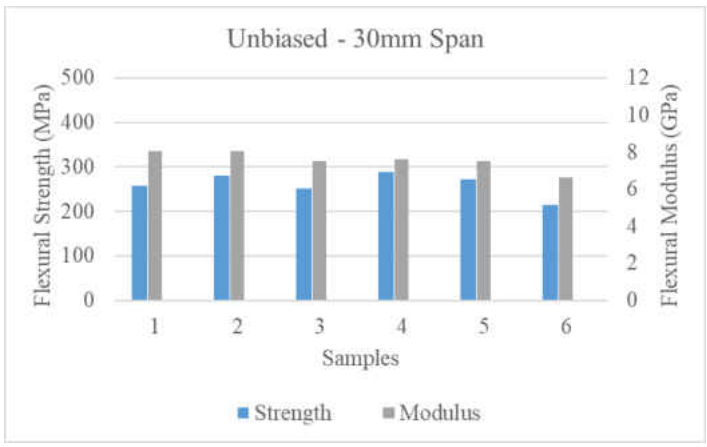

(b)

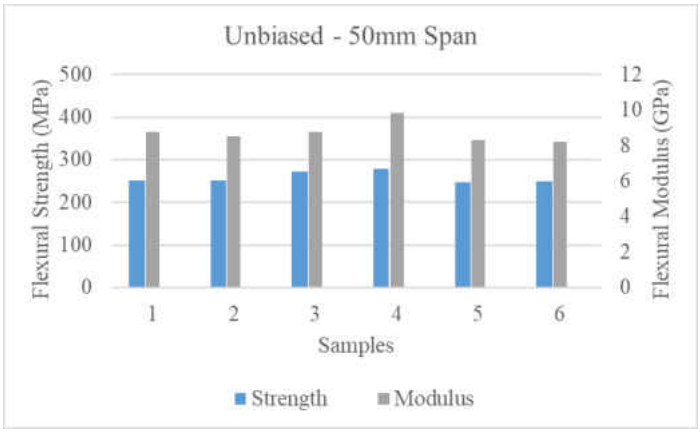

(c)

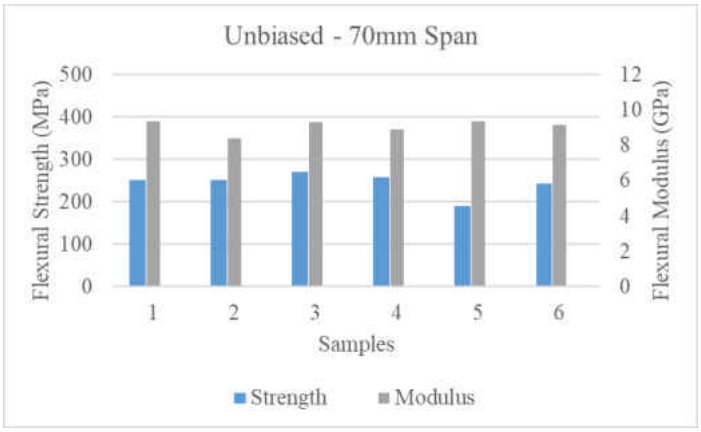

(d)

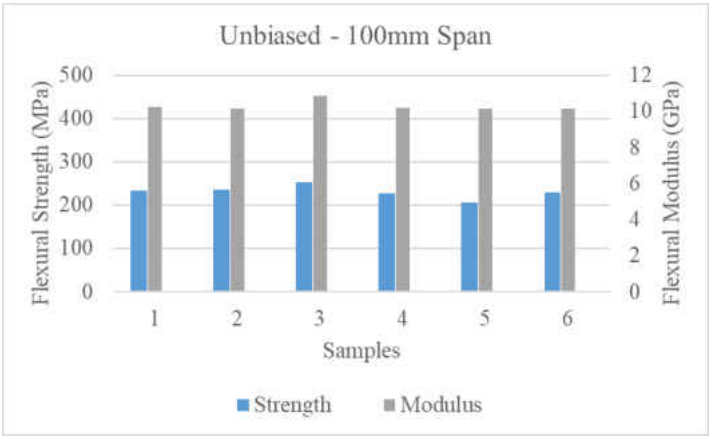

(e)

Figure 38 Glass Fiber Unbiased Direction: 20 mm Span (a), 30 mm Span (b), 50 mm Span (c), 70 mm Span (d), and 100 mm Span Calculated Data Bar Charts

Similar to the biased direction, flexural strength decreases as the span ratio increases (Figure 39a), but the difference in change was not as high as for the biased direction samples. The average result for the 100 mm span or ratio of 37 was also higher than the biased direction. Flexural modulus also appears to constantly increase and span increases, and a span ratio of about 20 was no longer the ratio for maximum modulus (Figure 39b)

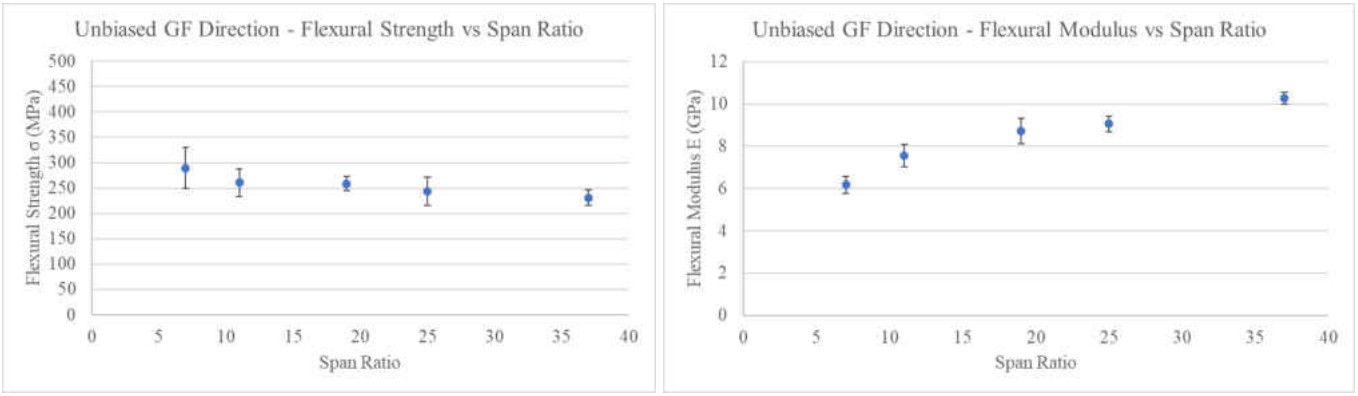

(a) (b)

Figure 39 Glass Fiber Unbiased Direction: Flexural Strength (a), Modulus (b) Calculated Data with Error Bar Graphs

4.1.2.3 Glass Fiber Composite: Design of Experiments Analysis

Prior to adding the 100 mm span for a better understanding of the behavior in material properties, a design of experiments approach was conducted to either help confirm or disprove this thesis' theory between the 20, 30, 50 and 70 mm spans.

It was important to identify the number of factors within the test. In this case two factors were selected: the span and fiber direction (Figure 40). Each factor is separated into proposed levels of analysis, factor A has four, which are the spans. Factor B is the general direction of the fibers, but since that may be random and cannot be truly measured, zero and 90 degrees were set for a numerical interpretation of biased and unbiased direction, respectively. There are two response variables, Flexural Strength and Flexural Modulus; these are the results that were compared against each other for correlation analysis.

DX6	Design Factor (units)	Range (normal level)	Measurement Precision	Proposed Levels
A	Span (mm)	20-180 (test machine limit)	0.1 mm	20, 30, 50, 70
B	Fiber Direction (Degrees)	0-90 degrees	1 deg	0, 90

Figure 40 DX Factors and Levels

Another important aspect to take in consideration for a DoE was to identify any nuisance factors, which are essentially the parameters we have no control over that may affect the results. The first nuisance factor is the theory itself, the fiber direction, certain sections of the sheets may have the fibers with preferred orientation, therefore creating inconsistency. The next is impurities, the most noticeable one would be the abrasive of the waterjet cutter, sand. The semi-finished sheets come in almost porous state, so if they are not properly cleaned before heating

and compaction, this could lead to unwanted particles and different results as if it was just fiberglass and nylon composites. The third is the thickness throughout the tested samples, which can be caused by fiber bundle waviness, causing a variation in thickness. Each specimen was measured at different places to estimate and overall thickness before they were subjected to testing. The final and what could be the most important factor is the cooling/crystallization of the composites, if not properly treated, this could lead to unsuccessful adhesion between the fibers and matrix, leading to drastically different material properties.

Once the calculated data were input into DX, a cubic model for an ANOVA was made. This specific model was chosen due to both of their responses being aliased, meaning that their interactions cannot be separated and individually analyzed. A significance level of $\alpha=0.05$ was administered to the test. After DX ran the first two aliased models, the response of Flexural Strength and Modulus were shown as the following (Figures 41 and 42).

Response 1: Flexural Strength

Source	Sum of Squares	df	Mean Square	F-value	p-value	
Block	15182.47	4	3795.62			
Model	1.190E+05	6	19829.08	37.65	< 0.0001	significant
A-Span	312.73	1	312.73	0.5939	0.4472	
B-Fiber Direction	29942.11	1	29942.11	56.86	< 0.0001	
AB	6516.54	1	6516.54	12.37	0.0015	
A^2	49.40	1	49.40	0.0938	0.7616	
B^2	0.0000	0				
A^2B	1071.07	1	1071.07	2.03	0.1645	
AB^2	0.0000	0				
A^3	1300.88	1	1300.88	2.47	0.1269	
B^3	0.0000	0				
Residual	15271.53	29	526.60			
Cor Total	1.494E+05	39				

Figure 41 DX Cubic Flexural Strength ANOVA Model

Response 2: Flexural Modulus

Source	Sum of Squares	df	Mean Square	F-value	p-value	
Block	2.99	4	0.7472			
Model	51.56	6	8.59	24.32	< 0.0001	significant
A-Span	0.9667	1	0.9667	2.74	0.1089	
B-Fiber Direction	7.92	1	7.92	22.42	< 0.0001	
AB	3.59	1	3.59	10.17	0.0034	
A^2	14.77	1	14.77	41.79	< 0.0001	
B^2	0.0000	0				
A^2B	1.31	1	1.31	3.70	0.0642	
AB^2	0.0000	0				
A^3	0.0533	1	0.0533	0.1509	0.7005	
B^3	0.0000	0				
Residual	10.25	29	0.3534			
Cor Total	64.79	39				

Figure 42 DX Flexural Modulus ANOVA Model

The two tables for aliased models can be interpreted by their p-values. Insignificant factor interactions between A and B can be ignored when *p*-values are greater than 0.05. Thus, for the current model, the factors along with all their possible combinations which have no effect on both strength and modulus are shown in Figure 43.

Flexural Strength	Flexural Modulus
A	A
A^2	-
B^2	B^2
A^2B	A^2B
AB^2	AB^2
A^3	A^3
B^3	B^3

Figure 43 DX Insignificant Factors

Due to the experiment having several insignificant factors shown, it can still be reduced to a simpler model. Currently, factor A (span) seems to be an insignificant parameter. However, due to the interaction AB shown to be significant, factor A was kept, maintaining hierarchy for both strength and modulus.

After removing all insignificant factors and their responses; span, fiber direction and their interaction were shown to be significant (Figures 44 and 45), each with *p*-values less than 0.05 and span having the biggest effect on the modulus, hence: A^2 (Figure 45).

Response 1: Flexural Strength

Source	Sum of Squares	df	Mean Square	F-value	p-value	
Block	15182.47	4	3795.62			
Model	1.165E+05	3	38839.58	70.11	< 0.0001	significant
A-Span	37790.81	1	37790.81	68.22	< 0.0001	
B-Fiber Direction	65376.84	1	65376.84	118.01	< 0.0001	
AB	6653.78	1	6653.78	12.01	0.0015	
Residual	17727.26	32	553.98			
Cor Total	1.494E+05	39				

Figure 44 DX Reduced Flexural Strength ANOVA Table

Response 2: Flexural Modulus

Source	Sum of Squares	df	Mean Square	F-value	p-value	
Block	2.99	4	0.7472			
Model	50.20	4	12.55	33.51	< 0.0001	significant
A-Span	19.93	1	19.93	53.23	< 0.0001	
B-Fiber Direction	10.77	1	10.77	28.77	< 0.0001	
AB	3.71	1	3.71	9.90	0.0036	
A^2	14.71	1	14.71	39.29	< 0.0001	
Residual	11.61	31	0.3745			
Cor Total	64.79	39				

Figure 45 DX Reduced Flexural Modulus ANOVA Table

The following fits statistics (Figures 46 and 47) values are meant to show how good the created model fits within the calculated data for possible regression modeling. It is shown that Flexural Strength has an ~87 percent variation explained by the model, and even with an adjusted or predicted model, the values are not too far off.

Std. Dev.	23.54		**R^2**	0.8679
Mean	310.17		**Adjusted R^2**	0.8556
C.V. %	7.59		**Predicted R^2**	0.7970
			Adeq Precision	20.6756

Figure 46 DX Flexural Strength Fit Statistic

Similarly, Flexural Modulus has an ~81 percent predictability, with its respective adjusted and predicted values falling within a 12 percent difference.

Std. Dev.	0.6120		**R^2**	0.8122
Mean	8.55		**Adjusted R^2**	0.7879
C.V. %	7.16		**Predicted R^2**	0.6958
			Adeq Precision	15.4010

Figure 47 DX Flexural Modulus Fit Statistic

Diagnostic plots are a good visual representation for noticing outliers or trends within the experiment ranges. The three main plots are: Normal Plot of Residuals (Figure 48), which essentially needs to pass the “fat pencil test” to make sure there are not any true outliers. The

second is a Residual vs. a Run plot (Figure 49), meant to see if each individual test is time variant and shows independence (no slope). If there is one, then the entire experiment would need to be done a second time after the issue has been identified and solved. The final plot is a Residual vs. a Predicted one (Figure 49), where variance is checked to see if values diverge from the mean, where a slope of zero is

also preferred.

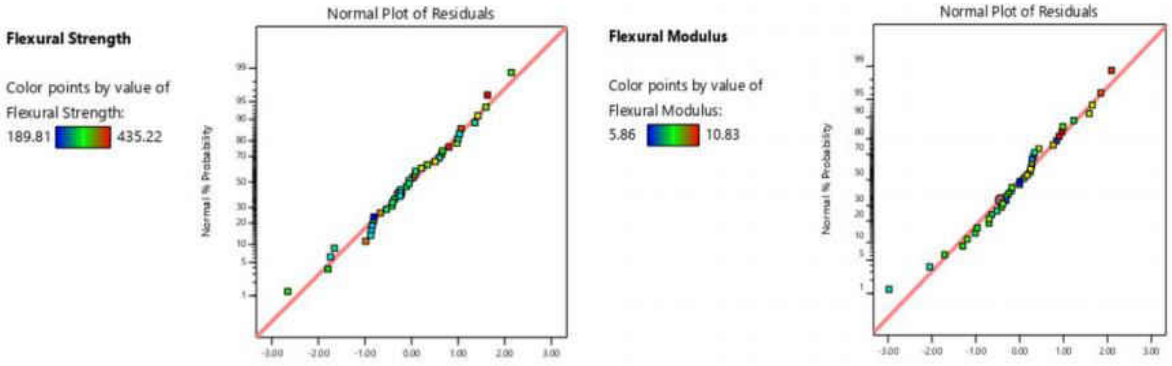

(a) (b)

Figure 48 DX Normal Plot of Residuals: Flexural Strength (a), Modulus (b)

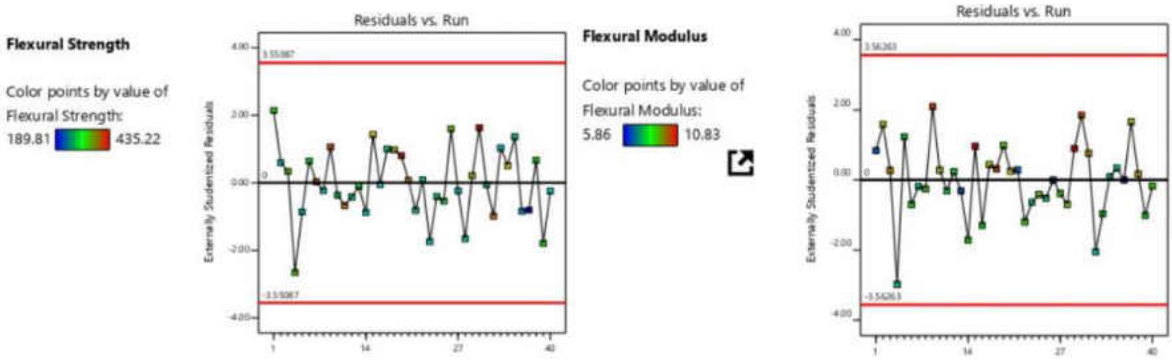

(a) (b)

Figure 49 DX Residual vs Run: Flexural Strength (a), Modulus (b)

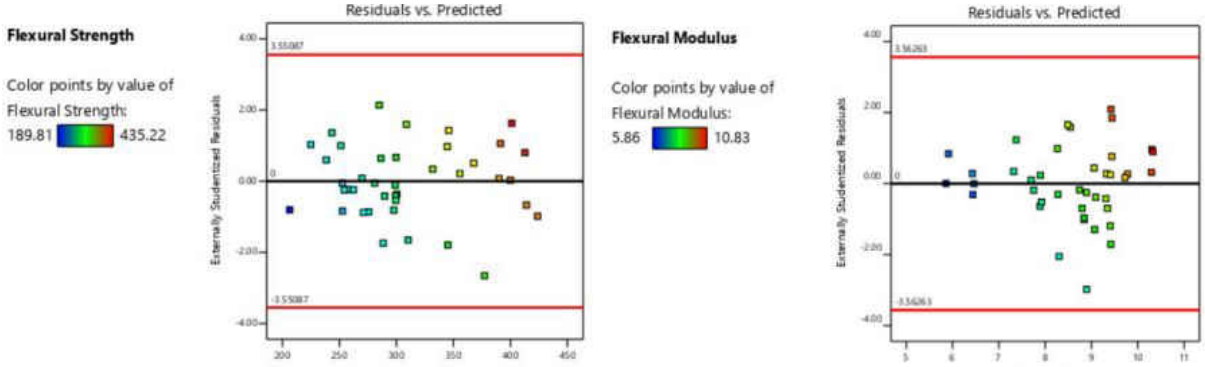

(a) (b)

Figure 50 DX Residual vs Predicted: Flexural Strength (a), Modulus (b)

Since all three Flexural Strength plots appear to pass their tests, DX does not recommend a Box-Cox transformation, however, that is not the case for our Flexural Modulus calculations. The first two plots pass their tests, but the Residual vs. the Predicted data appears to trend outwards in a conical shape and is not constant (Figure 50b – Flexural Modulus). Therefore, an inverse square-root transformation is recommended by DX as shown in Figure 51. This would increase our value ranges over several orders of magnitude.

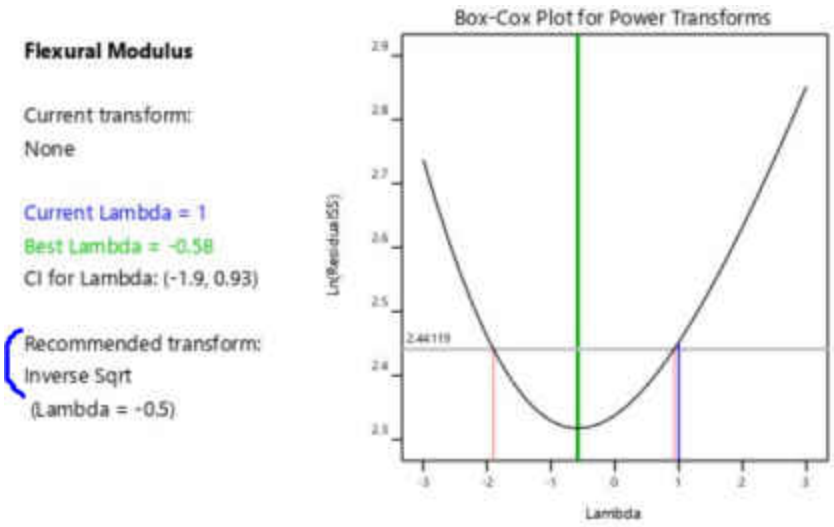

Figure 51 DX Flexural Modulus Transformation

After the Flexural Modulus data was transformed by DX, the three following diagnostic plots are shown.

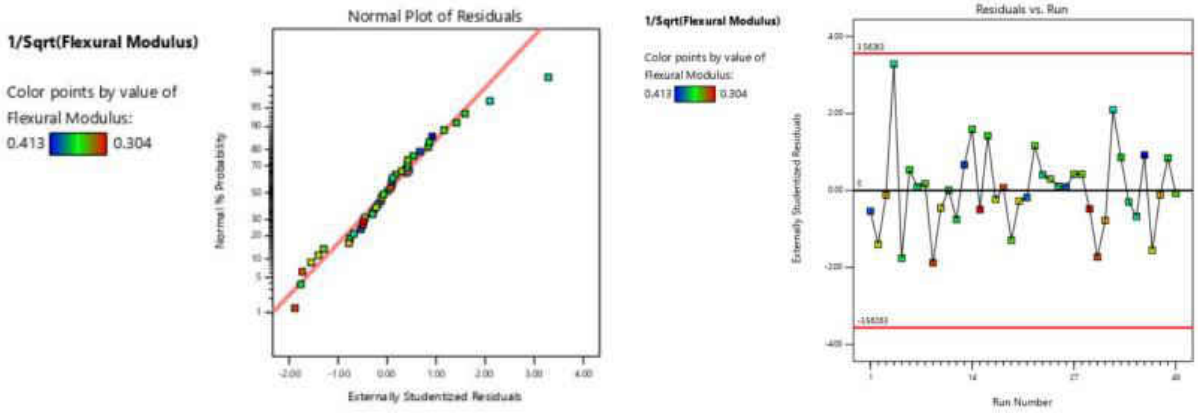

(a) (b)

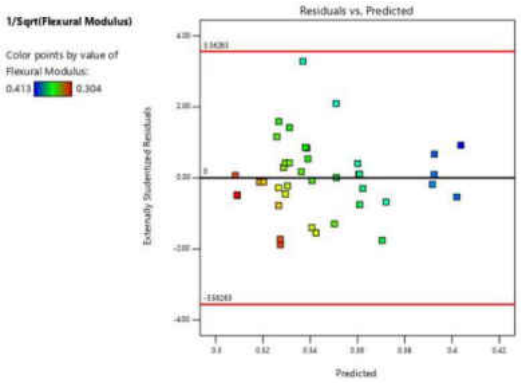

(c)

Figure 52 DX Transformed Flexural Modulus Diagnostic Plots: Normal Plot of Residuals (a), Residual vs Run (b), and Residual vs Predicted (c)

The new Normal Plot of Residuals has one point that falls outside the fat pencil test bound, but this point is kept since the potential outlier falls within bounds of the new Residual vs. the new Predicted plot. The transformed Residual vs. the Run plot shows independence across the centerline and once again, it passes. Finally, the last plot of Residuals vs. the Predicted now shows a more constant variance after transformation, therefore no new changes are recommended/necessary.

For confirmation, the same factors that were shown to be significant are still doing so after the transformation of our Flexural Modulus data (Figure 53).

Response 2: Flexural Modulus
Transform: Inverse Sqrt
Constant: 0

Source	Sum of Squares	df	Mean Square	F-value	p-value	
Block	0.0011	4	0.0003			
Model	0.0239	4	0.0060	44.12	< 0.0001	significant
A-Span	0.0101	1	0.0101	74.58	< 0.0001	
B-Fiber Direction	0.0046	1	0.0046	33.75	< 0.0001	
AB	0.0023	1	0.0023	17.22	0.0002	
A^2	0.0063	1	0.0063	46.60	< 0.0001	
Residual	0.0042	31	0.0001			
Cor Total	0.0292	39				

Figure 53 DX Transformed Flexural Modulus ANOVA Table

The transformed fit statistic for Flexural Modulus (Figure 54) now gives an ~85 percent predictability for regression modeling, with both the adjusted and predicted R showing better and closer results than without transformation.

Std. Dev.	0.0116		**R^2**	0.8506
Mean	0.3450		**Adjusted R^2**	0.8313
C.V. %	3.38		**Predicted R^2**	0.7589
			Adeq Precision	17.2809

Figure 54 DX Transformed Flexural Modulus Fit Statistic

A final step that can be done with DX is to use the predicted intervals to complete random confirmation runs that may fall within the experiment bounds. The higher the R value is, the more chances DX will randomly select a number falling within boundaries. This is done as a means to predict what outcome will happen on future tests. Randomly selected spans and biased (zero) or unbiased (90) fiber directions are chosen by the software, and in this case, the predicted values are acceptable, note that sometimes this is not the case as there is still a chance that predictions will not be realized.

Factor	Point 1	Point 2	Point 3
Span (mm)	20	50	70
Fiber Direction (deg)	0	0	90
Flexural Strength Predicted Interval (MPa)	$387.234 < x < 420.262$	$324.07 < x < 347.088$	$223.452 < x < 260.902$
Actual Flexural Strength (MPa)	390.99	329.1	242.95
Flexural Modulus Predicted Interval (GPa)	$7.5703 < x < 8.3801$	$9.76062 < x < 10.7672$	$8.4263 < x < 9.4883$
Actual Flexural Modulus (GPa)	7.74	10.62	9.14
Range Comparisons	Pass, Pass	Pass, Pass	Pass, Pass

Figure 55 DX Prediction Interval Confirmation Runs

4.2 Non-crimp Fabric Compaction and Wrinkling Tests

4.2.1 Compaction Test

Overall, compaction results did not show any noticeable difference between the size of the sample or compaction speed, all of the 152x152 mm (Figures 56 and 57) and 229x229 mm (Figures 58 and 59) samples also appear to behave the same way. Total thickness of the fabric does not show significant difference as pressure increases. The biggest change falls within the cyclic compaction, it can be concluded that fabric compaction is dominant for this non-crimp fabric after the third cycle, with the biggest difference just after the second trial.

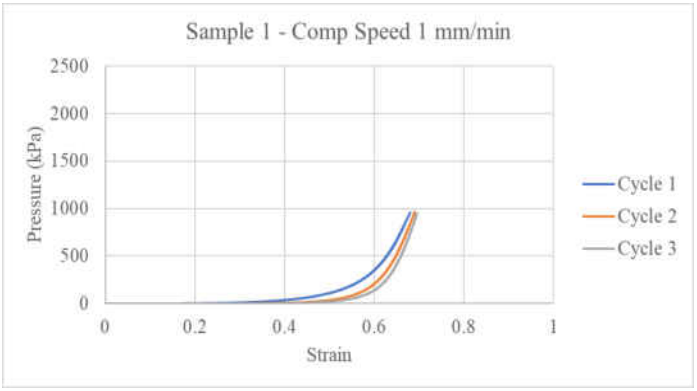

(a)

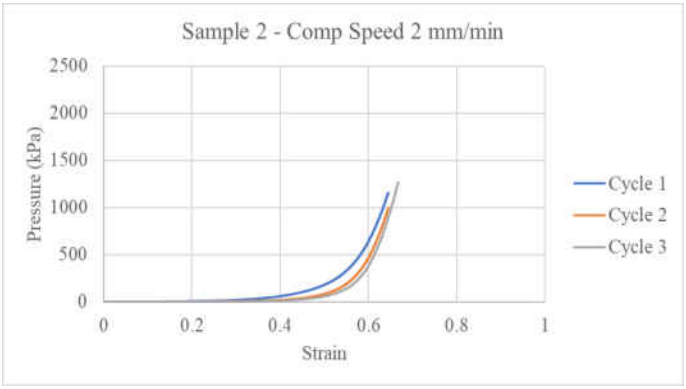

(b)

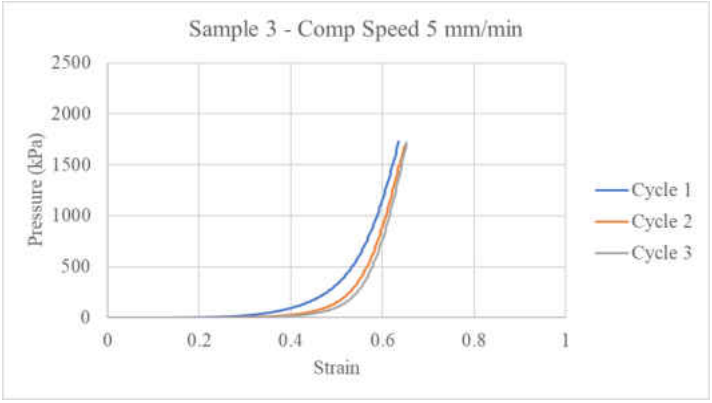

(c)

Figure 56 Influence of Compaction on 152x152 mm with 4 mm Thickness Samples

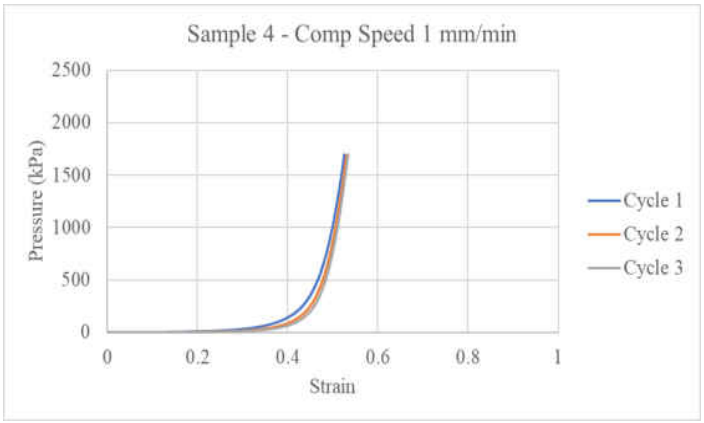

(a)

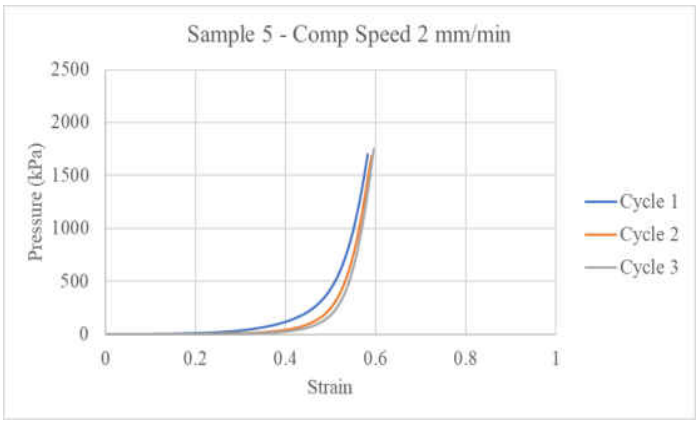

(b)

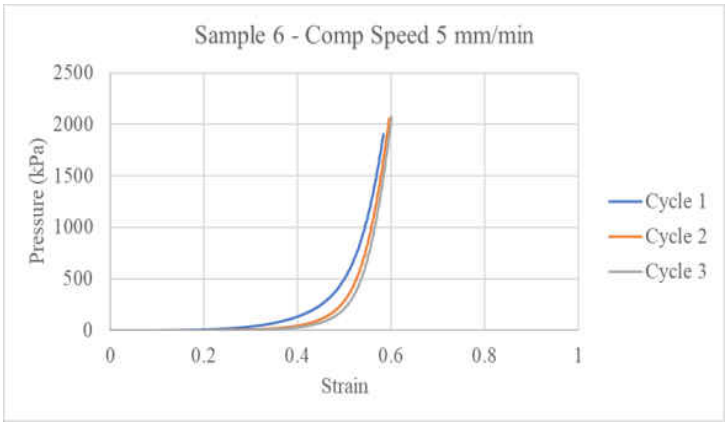

(c)

Figure 57 Influence of Compaction on 152x152 mm with 8 mm Thickness Samples

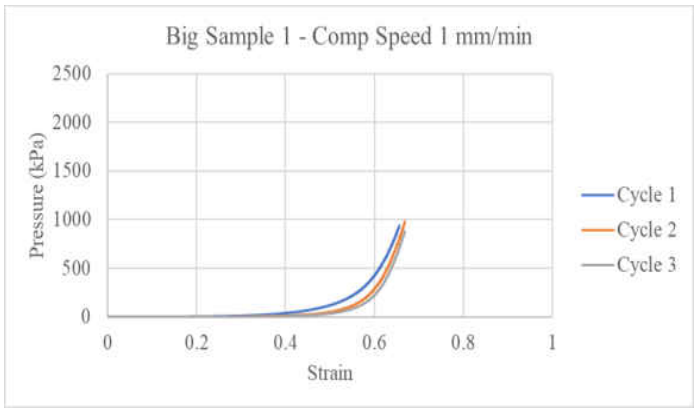

(a)

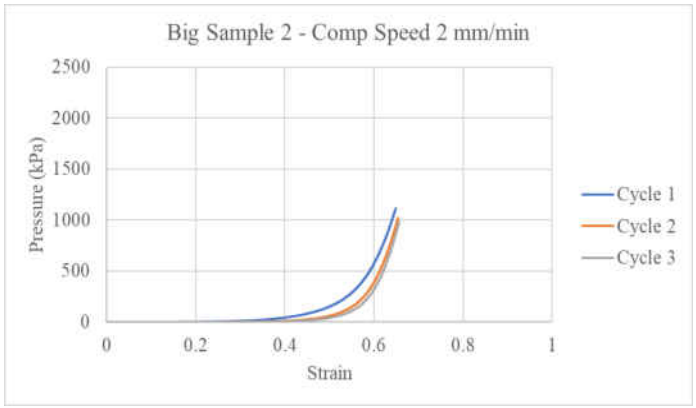

(b)

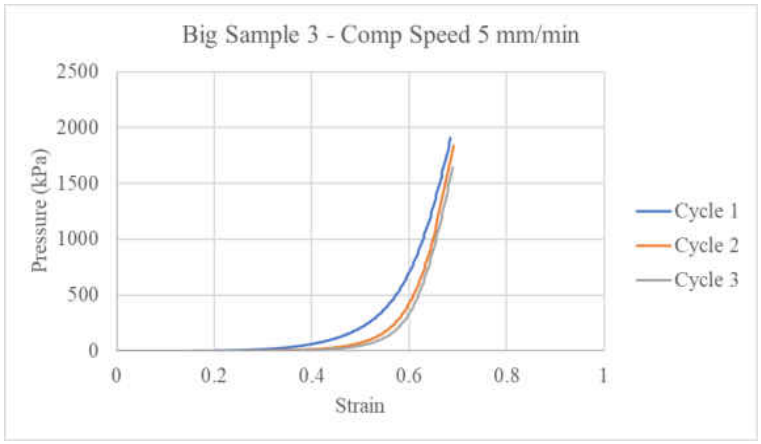

(c)

Figure 58 Influence of Compaction on 229x229 mm with 4 mm Thickness Big Samples

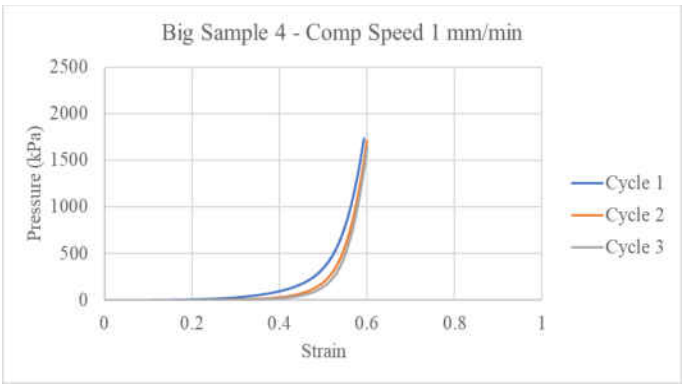

(a)

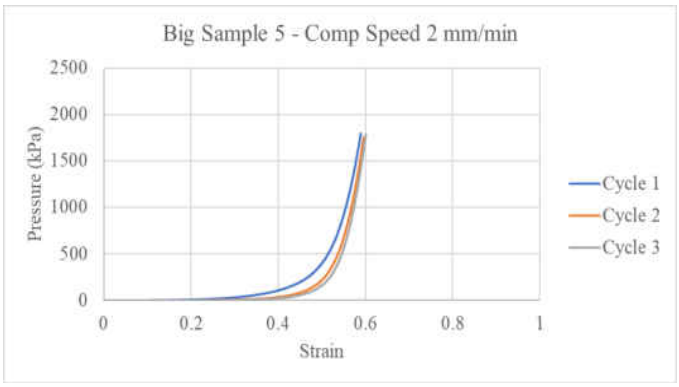

(b)

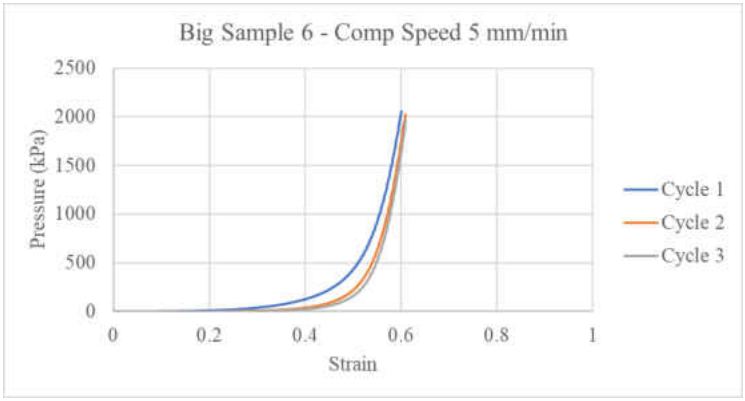

(c)

Figure 59 Influence of Compaction on 229x229 mm with 8 mm Thickness Big Samples

The two most visibly compacted 4 mm and 8 mm samples, samples 2 and 4, were selected from the big sample batch for further evaluation of the residual deformation. After the relaxation period, these two samples were scanned with the microscope to inspect the depth change from the uncompacted to compacted regions Figure 60.

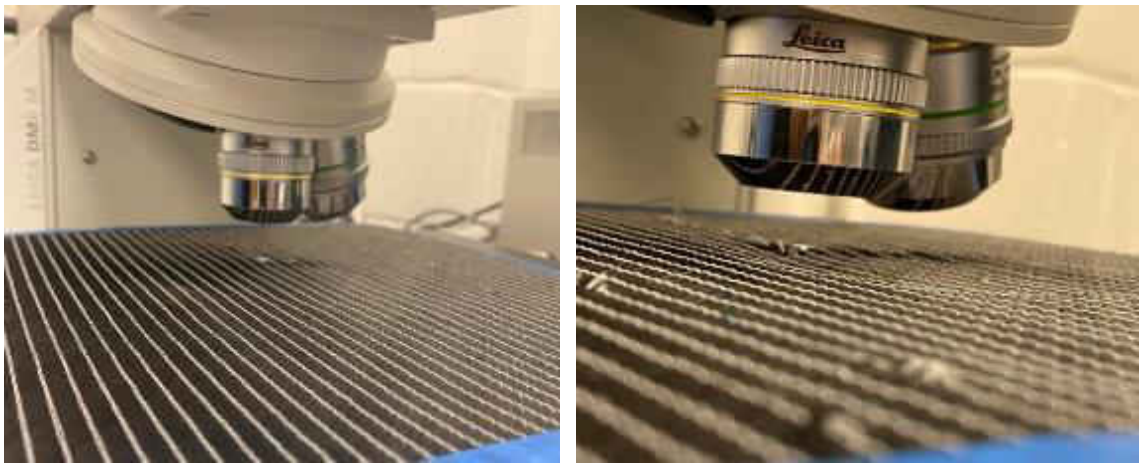

(a) (b)

Figure 60 Surface Scanning of 4 mm and 8 mm Thick Samples

The DM6-M Material Microscope scanned roughly a 2 mm x 20 mm section on both samples, this scan was parallel to the thin polymer threads to avoid scanning unnecessary sections. So, by combining pictures across the surface in all x, y, and z directions; 2D (Figure 61) and 3D (Figures 62 and 63) images were processed in order to be analyzed. Figure 61 shows the 2D scans of the 4 and 8 mm thick samples, respectively, where the uncompacted region starts on the bottom and transitions to the fully compacted region at the top of the images. Full scans of the compacted circles were not administered due to range limitations of the microscope.

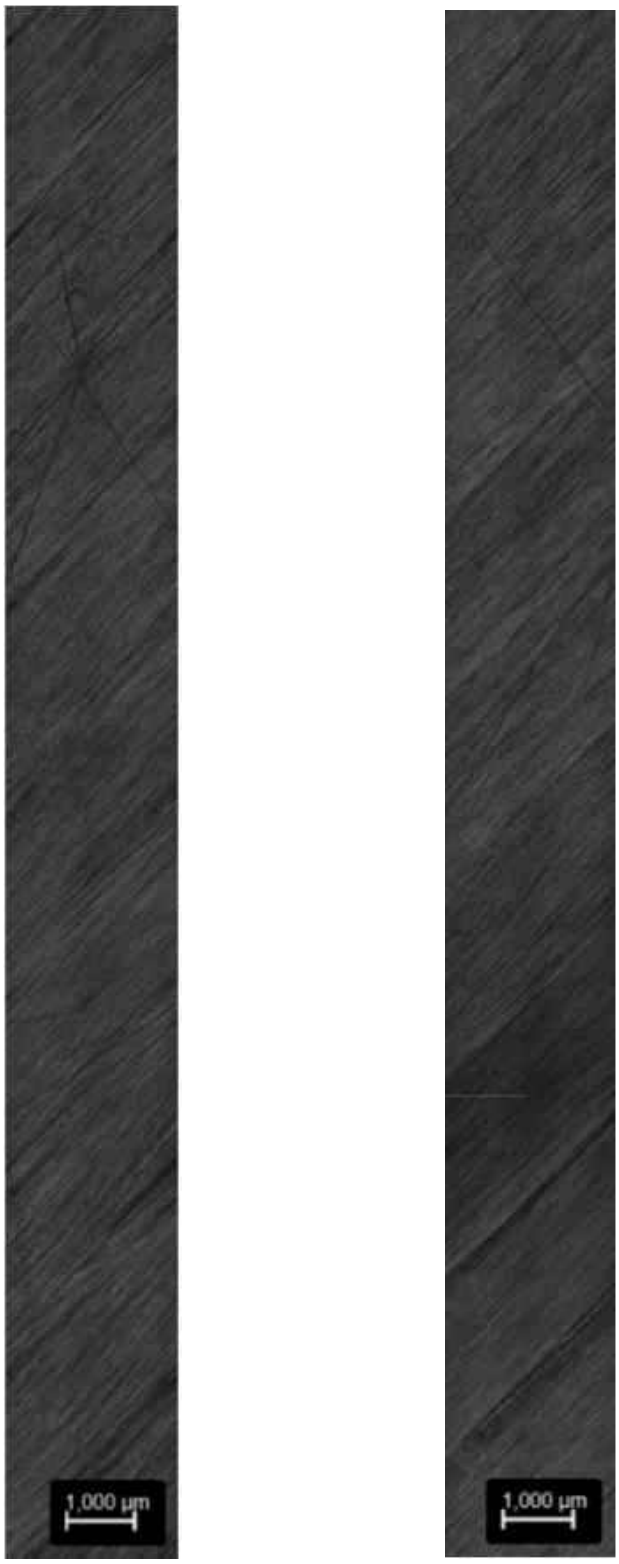

(a) (b)

Figure 61 2D Scan: 4 mm Thick Sample (a), and 8 mm Thick Sample (b)

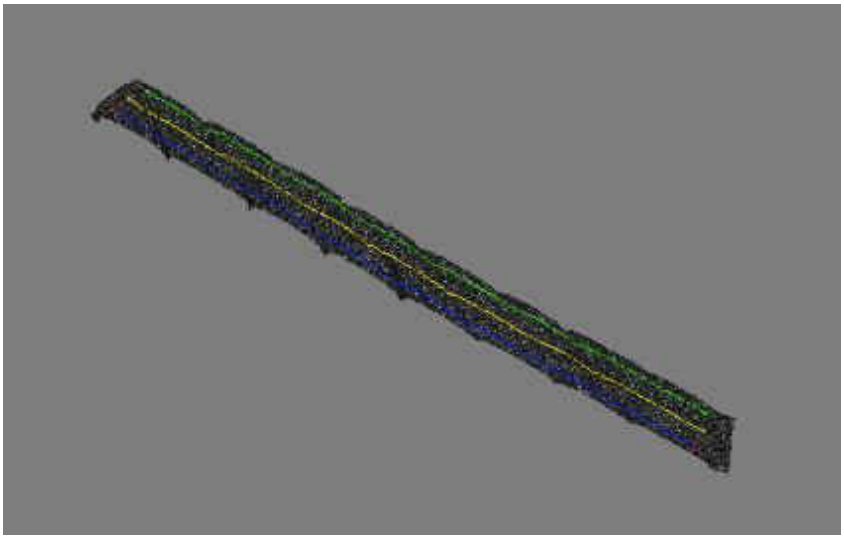

Figure 62 3D Scan: NCF 4 mm Thick Sample

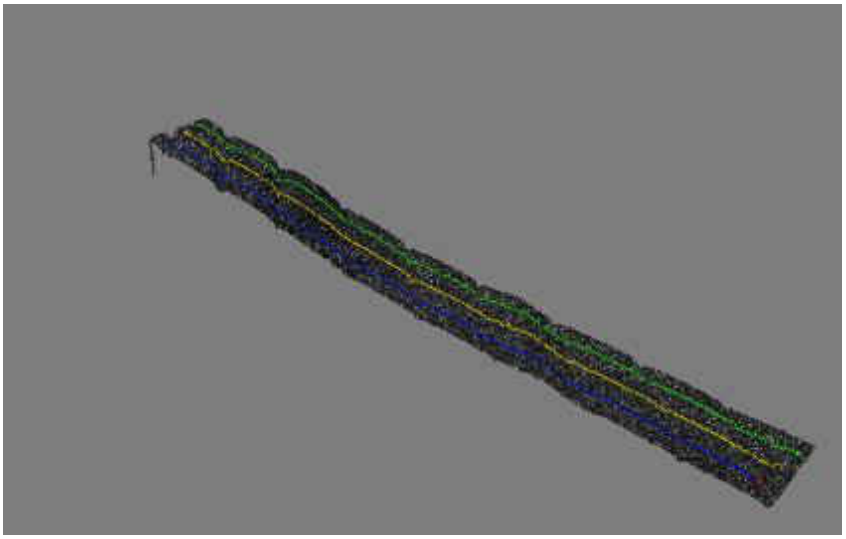

Figure 63 3D Scan: NCF 8 mm Thick Sample

The 3D view is used to measure the surface changes throughout the sample by manually adding colored lines on the surface. These lines gave data based on distance (x-axis) and height (y-axis) that were exported into an excel file for a single graph data merging per sample, Figure 64. The area scanned for these two surfaces had the uncompacted, transition, and compacted areas together. Three lines per sample gave enough data to estimate new fiber volume fractions.

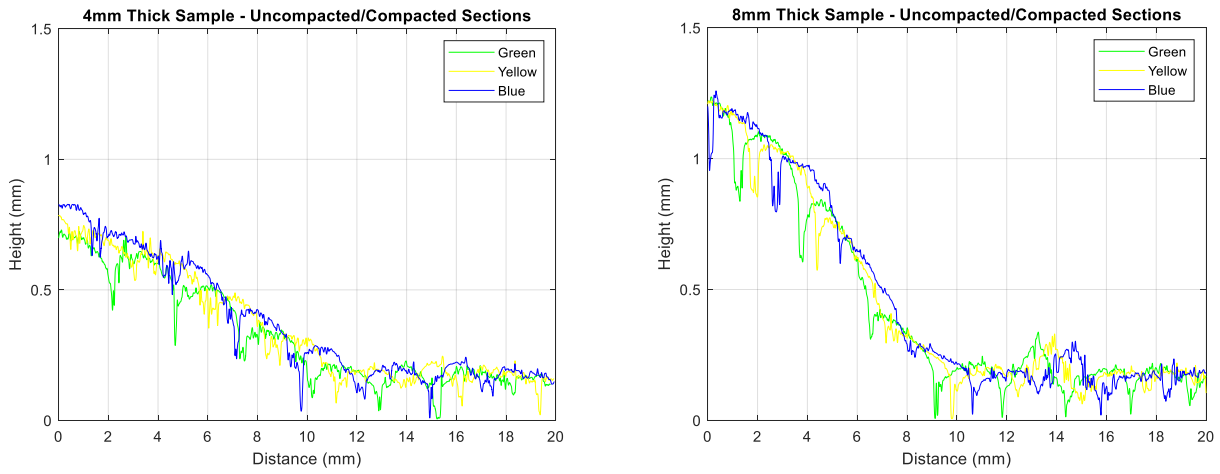

(a) (b)

Figure 64 4 mm Thick (a), 8 mm Thick (b) Compacted/Uncompacted Regions Shown in Figs 63-64

A 2D topography view (Figure 65) of the two surfaces gives a visual representation of the changes in height throughout both the 4 mm and 8 mm thick samples. The transition between the uncompacted and compacted regions can be seen on the left of each picture.

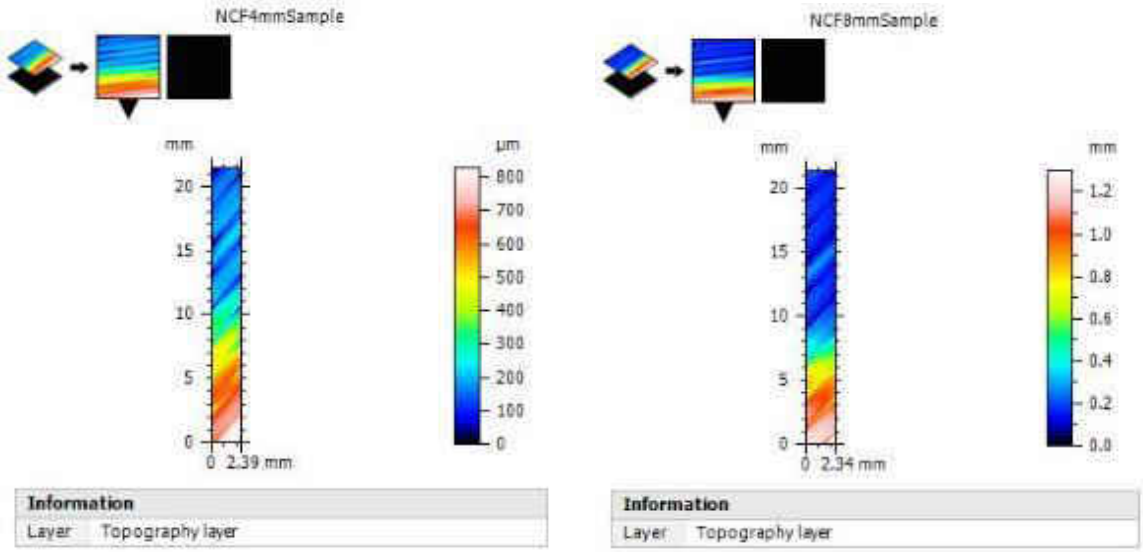

(a) (b)

Figure 65 4 mm and 8 mm Thick Samples: Pseudo-color 2D Views

From the calculated average thicknesses of both Big Samples 2 and 4; the uncompacted fiber volume fractions where calculated to be 39.7% and 38.8% fiber for the 4mm and 8mm thick samples, respectively. After the circular compaction took place and referring back to Figure 64, an average for the uncompacted region was measured from 0-1 mm, while the compacted region average was measured from 10-20 mm for both samples. The difference in height drop was then subtracted from the uncompacted thicknesses for final calculation. Both samples increased to 46.4% and 44.3% respectively, an increase between 5-7 percent.

A compaction test was also done with the roller fixture on the big samples 2 and 4 where the surface was still intact, Figure 66. Three cycles were completed for each thickness to replicate the testing parameters of prior flat compaction tests (Figure 67). Both surfaces were also scanned with the microscope to record the change in surface residual deformation after the same relaxation periods, Figure 68.

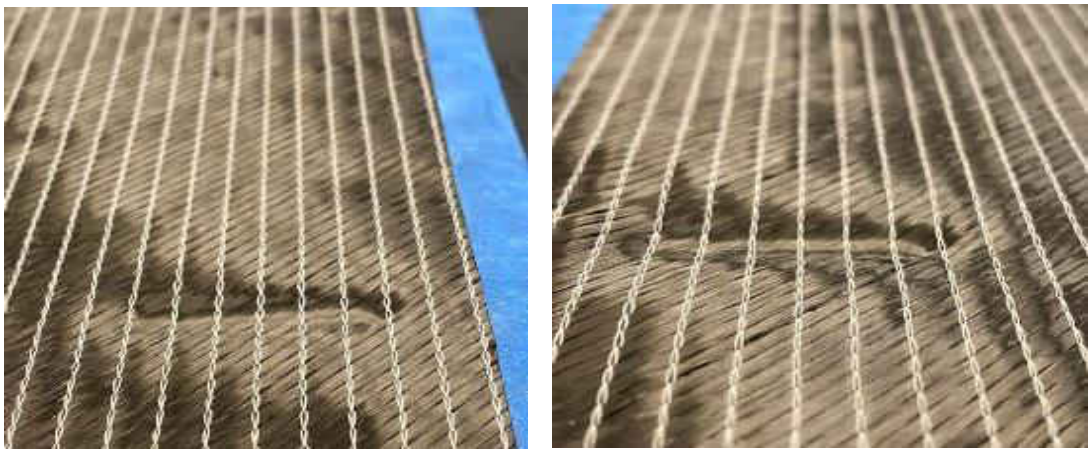

(a) (b)

Figure 66 4 mm Thick Compaction (a), 8 mm Thick Compaction (b)

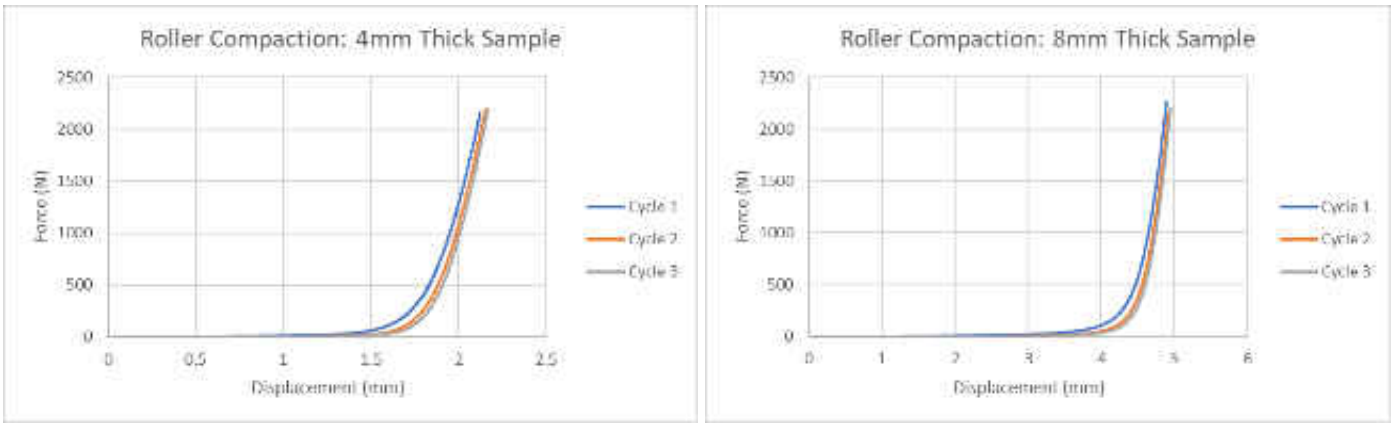

(a) (b)

Figure 67 Influence of Roller Compaction: 4 mm Thick (a), 8 mm Thick (b*)*

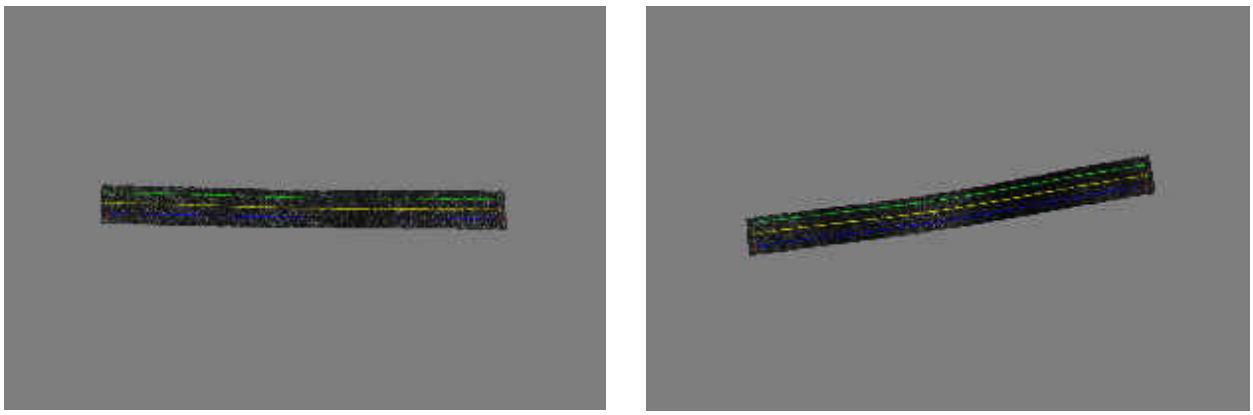

(a) (b)

Figure 68 4 mm Thick(a), 8 mm Thick(b) Samples Roller Compaction 3D Microscope Scans

The new roller compacted area for the 4mm thick sample (Figure 69a) appears to have a similar height difference as the 4mm thick circular compaction scans. However, the 8mm thick

samples show an increase of almost twice the height difference as the circular compaction, Figure 69b. Leading to conclude the smaller the areas of an object compacting the fabric, the more effect it will have on the fabric. For all scans, a 2 cm long scan was done since the microscope would take longer and run into more software issues when combining the scans.

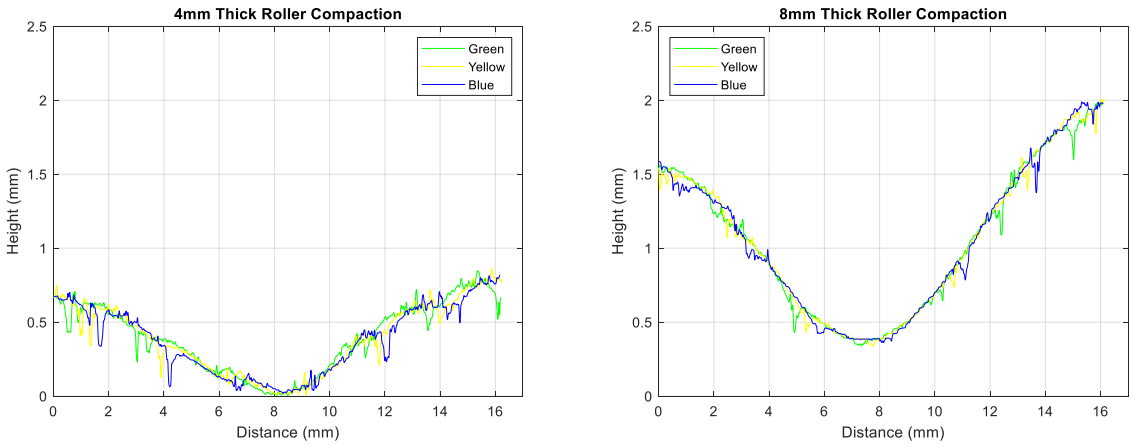

(a) (b)

Figure 69 4 mm(a), 8 mm(b) Roller Compaction Regions

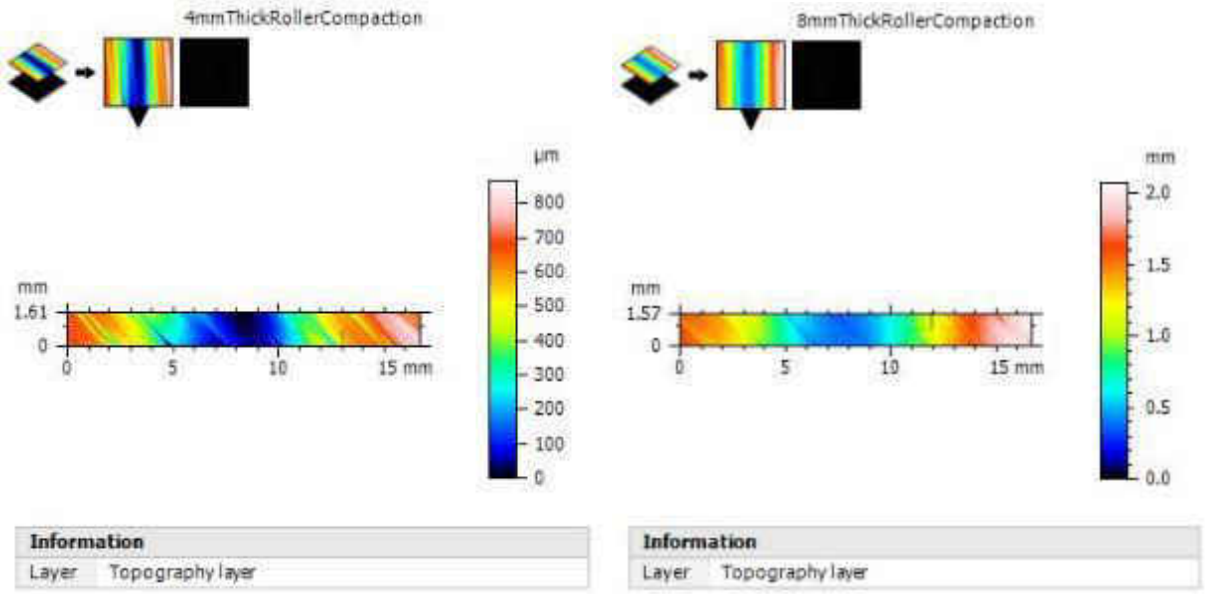

(a) (b)

Figure 70 4 mm Thick(a), 8 mm Thick(b) Topography Scans

Similar to the circular compactions and referring to Figure 69, the 4-mm-thick sample average compacted region was measured from 7-9 mm, while it average uncompacted region was from 15-16 mm. The 8 mm thick sample compacted region was from 6.5-8.5 mm, and from 15-16 mm for the uncompacted. After calculation, the 4-mm and 8-mm thick samples have a new fiber volume fraction of 48.3% and 47.7% respectively, with almost a 9% increase in fiber volume fraction for both samples.

4.2.2 Wrinkling Test

Once each sample was properly secured with the custom-made fixture (Figure 71a), it was laid on the bottom flat fixture as the crosshead of the machine was manually dropped close to the

surface of the sample. A metal block was also used to keep the sample in place and preventing the weight of the fixture and the hook of the winch from moving it before tests were started (Figure 71b). The same process was repeated when moving the loading location and fixture after each test.

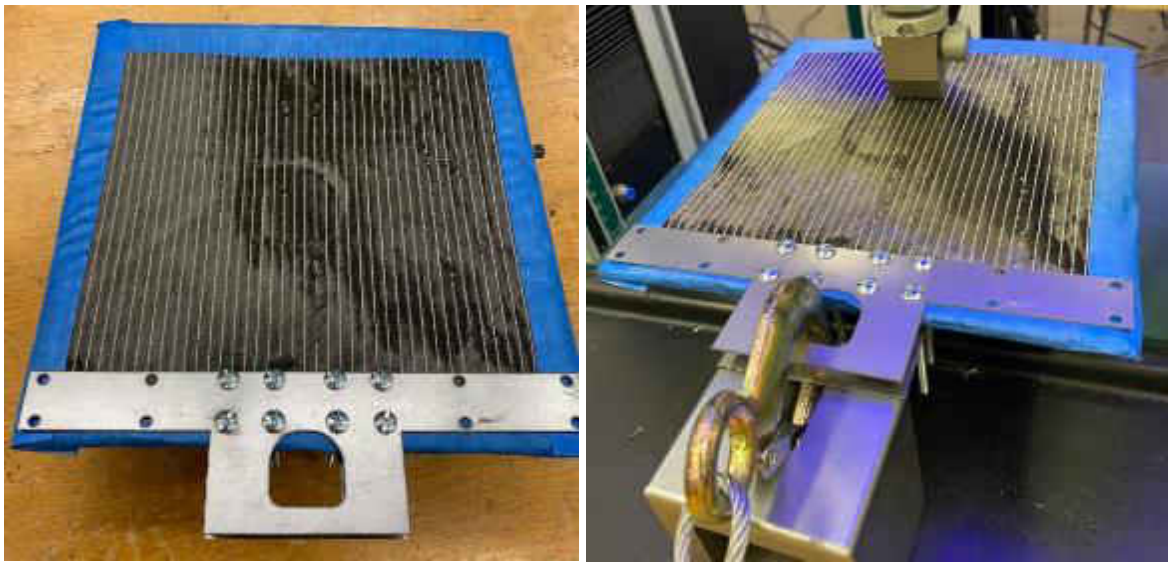

(a) (b)

Figure 71 Wrinkling Fixture Setup: Attached Fixture (a), Attached Winch (b)

Figure 72 shows how the winch was secured to the end of a table which was also raised to minimize the cable angle between the sample and the winch.

Figure 72 Winch and DIC Setup

When each test started, the crosshead was set to move downward until the desired load reading was attained. However, it was noticed that once the necessary force reading was attained, the load applied quickly decreased to lower values due to fiber tow nesting. Thus, every crosshead displacement was moved by a set amount to account for the desired load reading once the stable level of load was reached. At that time, the winch pulling was initiated with a digital camera recording the surface on the back of the roller until the end of the fabric was close or over the tape, or a maximum safety load reading of 500 N was reached for this test. For both samples, the load reading close to 150 N could not be reached due to the force quickly

increasing, and was instead completed between 200-250 N. Only the 4 mm thick sample went over the maximum set value, making the machine automatically stop the test. The sudden drops and increases of load on the fabric was an indication of the roller slipping and accommodating to compaction on the new bundles of fibers it touches as it is dragged along the surface. Figures 73 and 74 show the Force vs Time readings for each test.

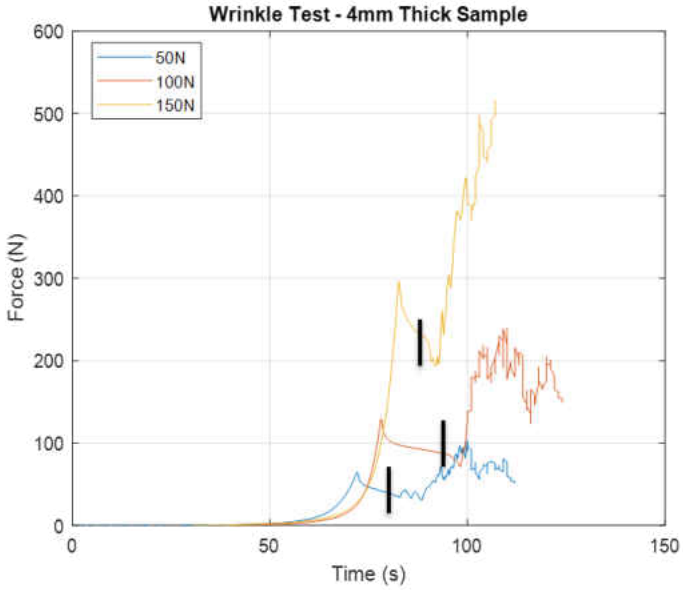

Figure 73 4-mm-thick Sample Wrinkle Tests

- Black lines indicate the points in which pulling and DIC recording started

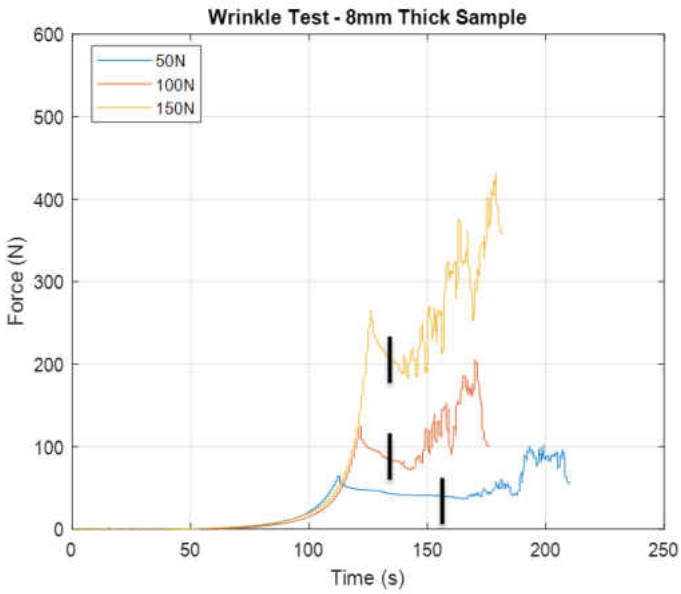

Figure 74 8-mm-thick Sample Wrinkle Tests

- Black lines indicate the points in which pulling and DIC recording started

Snapshots of the videos (Figure 75, 76) were taken and indicate the approximate location of the biggest increment in force for each test. These locations were also the points where bulging/buckling of the fibers can be detected.

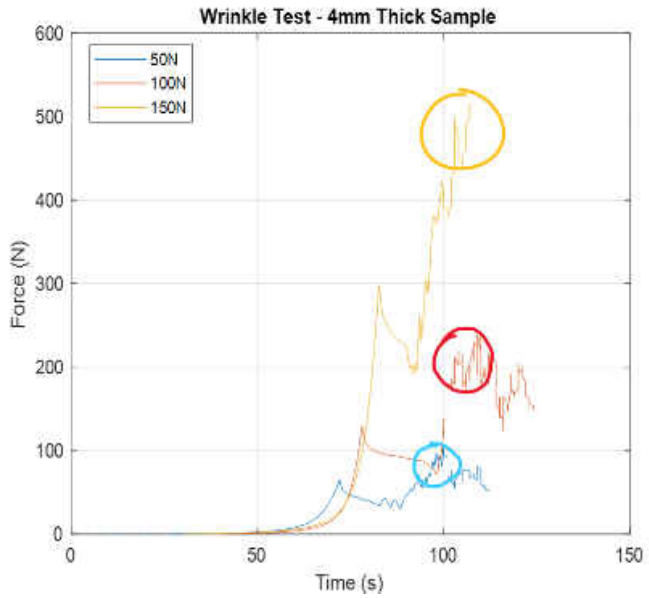

(a)

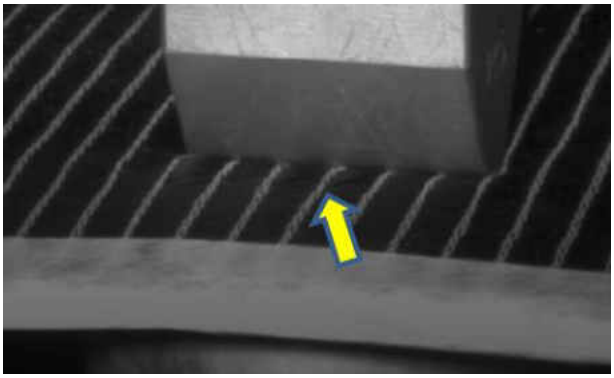

(b)

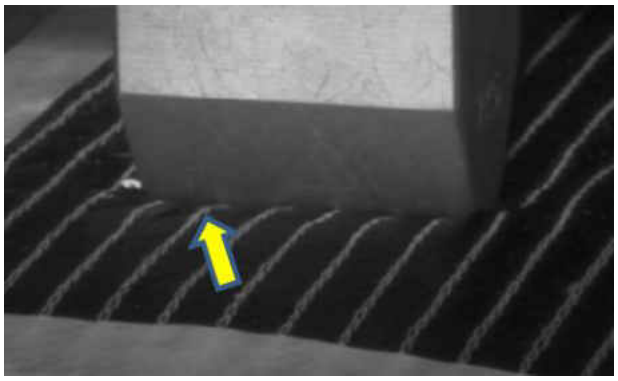

(c)

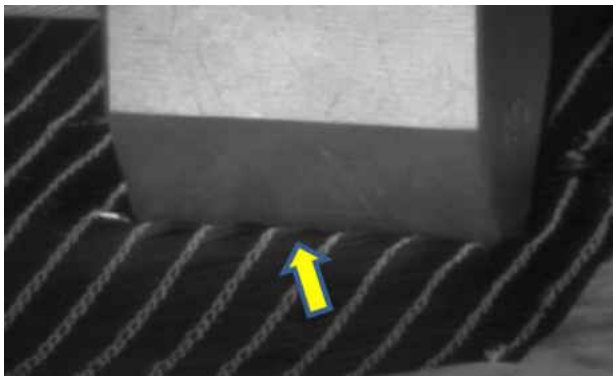

(d)

Figure 75 4-mm-thick Sample Max Load Increments (a): 50N (b), 100N (c), 150N (d)

- Arrows indicate the sections at highest force increments marked in the graph

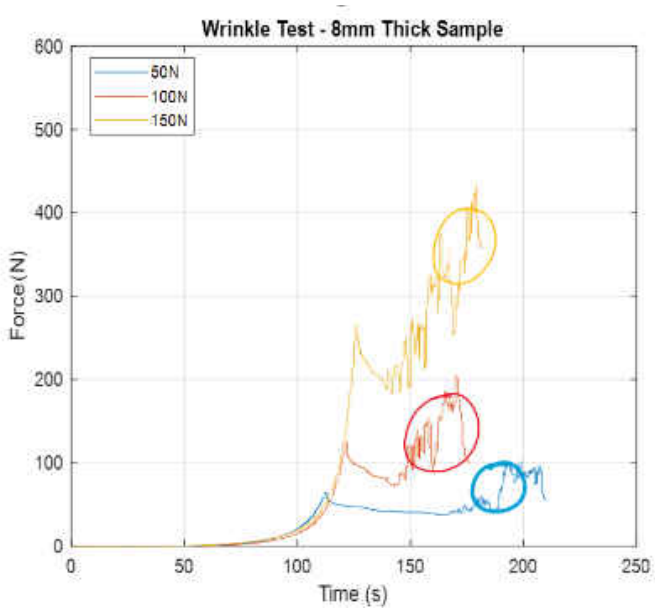

(a)

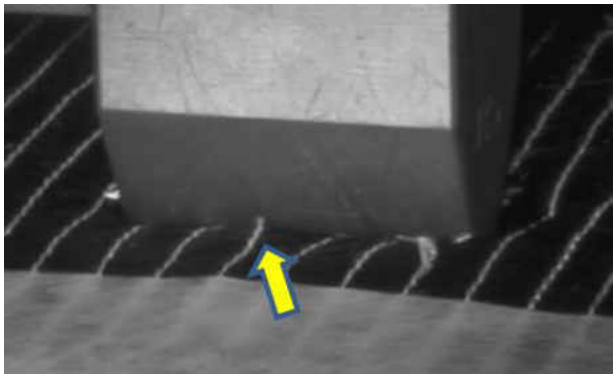

(b)

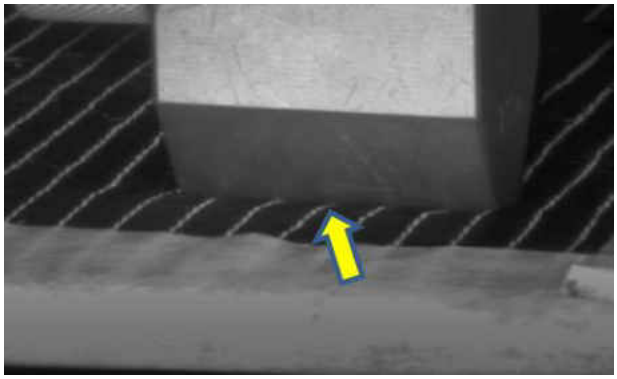

(c)

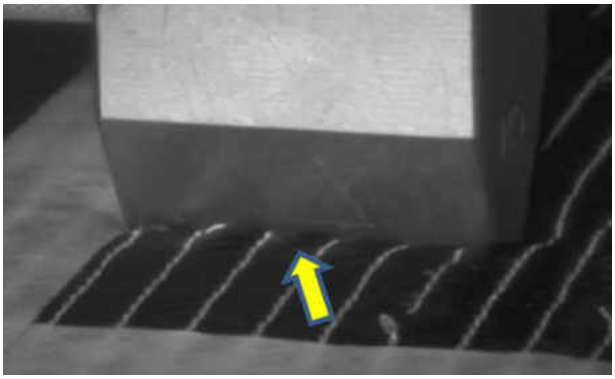

(d)

Figure 76 8mm Thick Sample Max Load Increments (a): 50N (b), 100N (c), 150N (d)

- Arrows indicate the sections at highest force increments marked in the graph

Figures 77 and 78 show surface scans of the most affected areas for the 4 mm and 8 mm

thick samples. As the force increases, more surface fiber distortion and damage can be detected on both cases, with a lot more fiber breakage with higher loads as indicated with the red arrows. It was also detected that the bundle orientation for the fibers were compromised (blue arrows) indicating loss of fiber collimation.

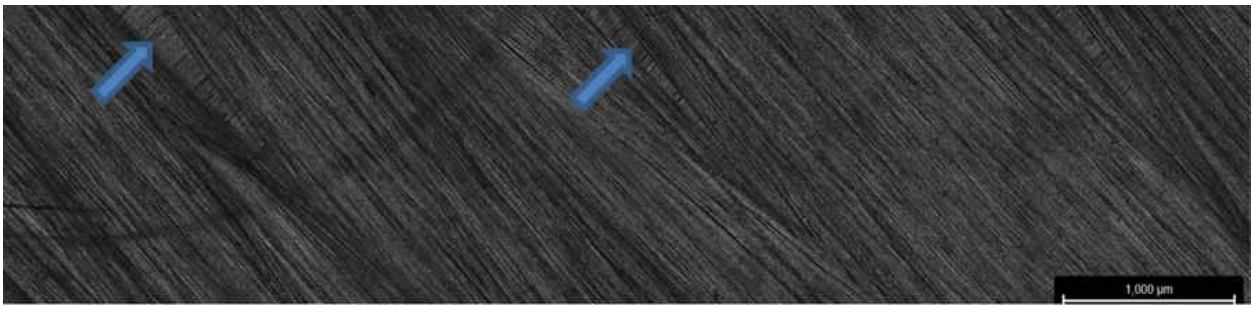

(a)

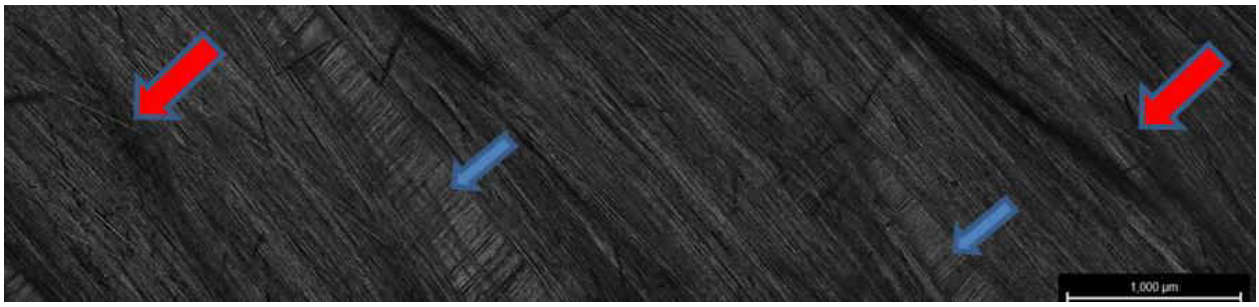

(b)

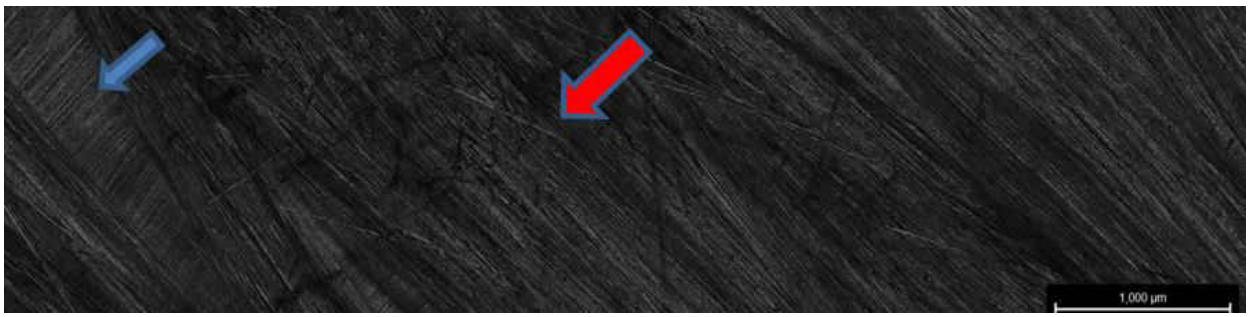

(c)

Figure 77 50 N (a), 100 N (b), 150 N (c) 4 mm Thick Surface Scans

- The roller fixture movement direction is from right to left on all three pictures

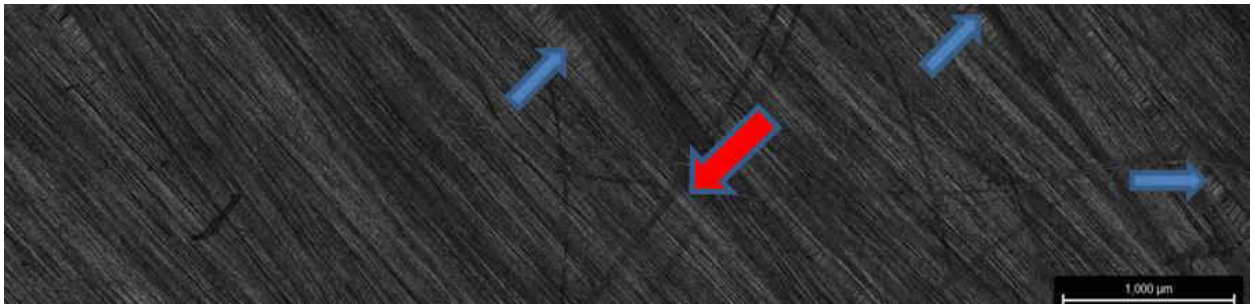

(a)

(b)

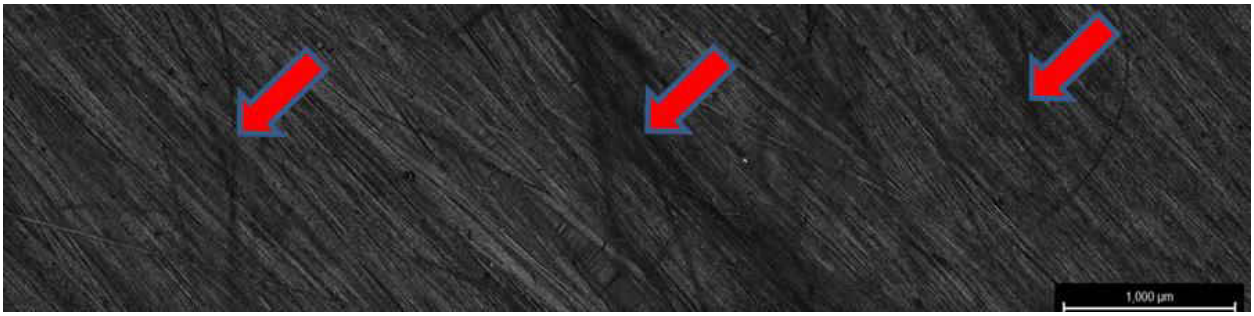

(c)

Figure 78 50 N (a), 100 N (b), 150 N (c) 8 mm Thick Surface Scans

- The roller fixture movement direction is from right to left on all three pictures

4.2.3 Presser Foot Design

Due to the lack of a CAD model for the current presser foot, it was carefully measured and duplicated using CREO Parametric, Figure 79. This models' dimensions were then used for comparison with subsequent design changes. Staying within boundary conditions was crucial to not end up with errors resulting in inaccurate sizes and collision when attached to the stitching head.

Figure 79 CREO Presser Foot Model

After identifying the important design constraints, such as assembly of the stitching head, or constraints associated with head movement and the presser foot itself, two main design models created that would satisfy the purpose of these changes. Option 1 is shown in Figure 80 and option 2 in Figure 81.

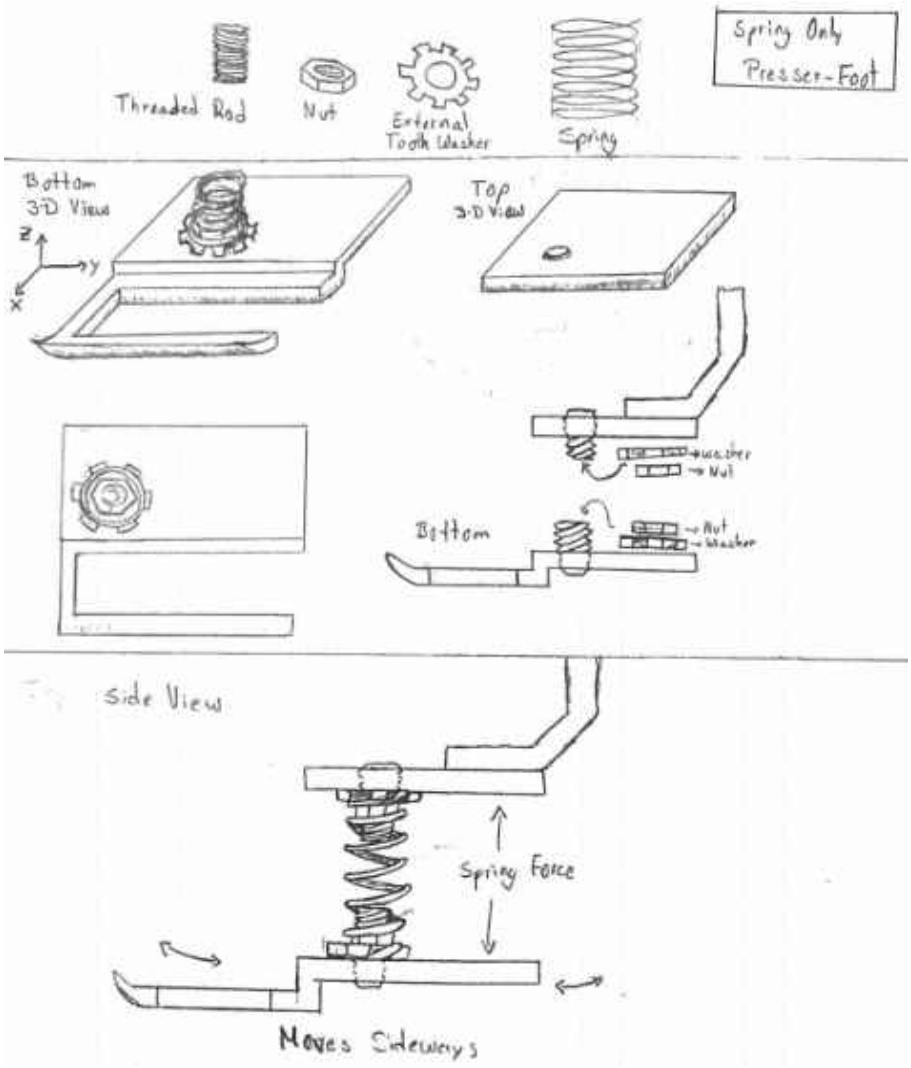

Figure 80 Spring Only Design

Option one, as shown in Figure 80, required several new pieces such as a metal springs, a threaded rod, a nut, an external tooth washer and a new top section for the presser foot. The new bottom part of the presser foot is also slightly different than the original piece to accommodate changes and eliminate unnecessary weight. The top part of new presser foot is used to connect the movable bottom part to a stiff shortened version of the arm. However, one of the downsides to this option is that this mechanism relies on the spring forces to sustain the weight of the bottom part, and counter act any forces applied on the presser foot. Therefore, the spring may wear off a bit faster than the second design option, while also being less stable.

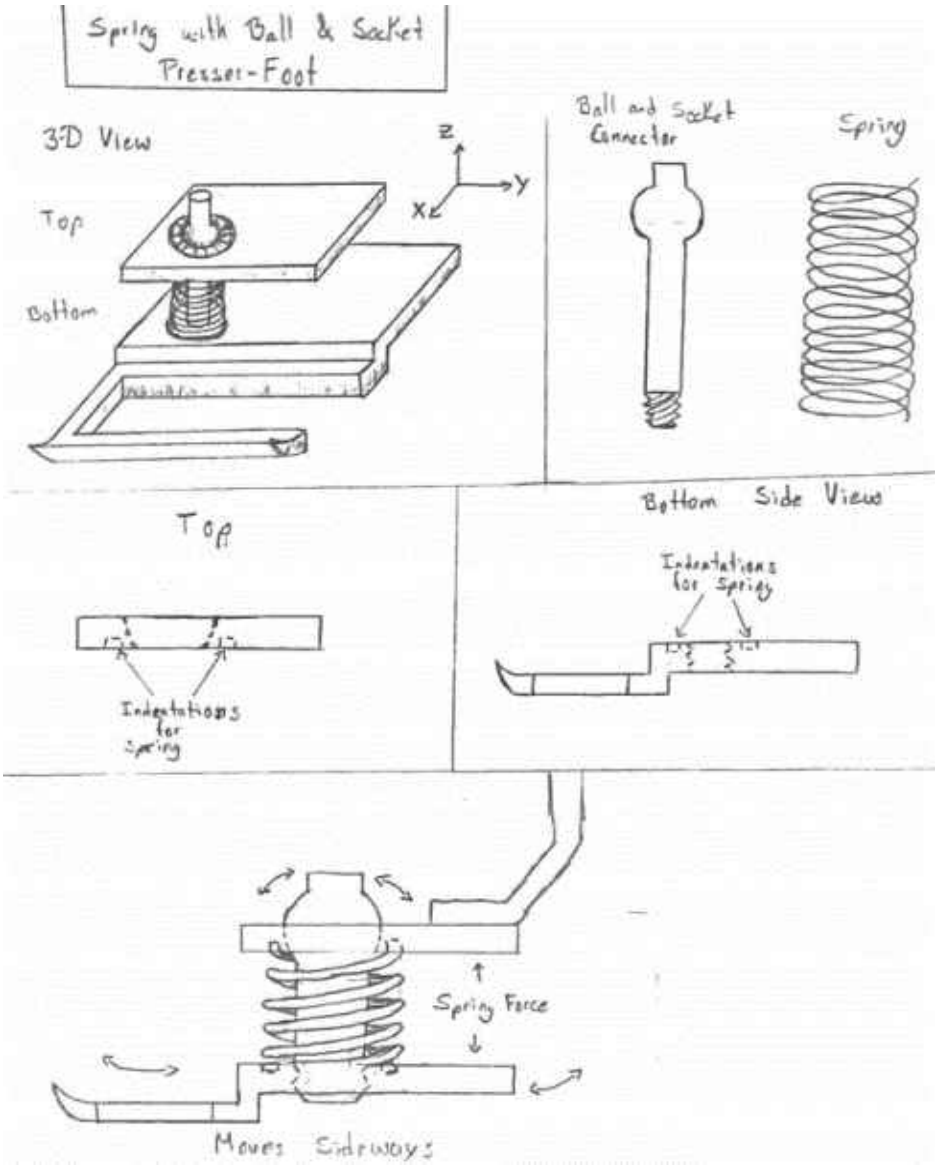

Figure 81 Ball & Socket Design

The only new parts for option two shown in Figure 81 would be a ball and socket connector which can be milled to specific dimensions, and a metal spring of desired length, inner radius and coil thickness. This design is like the design for option one, but requires fewer parts and is simpler to assemble. The spacing between top and bottom part of presser foot is dependent

on ball and socket connector length, which at the same time gives is a mechanical advantage over its counterpart. Since it does not require the stiffness of the spring to carry the weight of the bottom section, it is also more stable. Ring indentations will also be milled into the top and bottom parts to keep the spring from sliding sideways from desired location. The milling will be done once it has been decided what compression spring and parameters are needed. Even when compacted a small amount, this design becomes a spring-only dependent system when forces applied are applied.

Threaded holes were added to the top and bottom sections to make it a hybrid between the two options (Figure 82). The two holes on the sides of the ball and socket connector will be used for screws that will help clamp the spring on both sides, much like option one. This design also has the three holes making a triangle on the bottom section, so it can be used as the original stiff model if needed. Although the bottom part is now a bit longer on the y direction as shown in the drawings, it is shorter on the x direction. The underside edges were rounded to allow for a softer contact transition between the presser foot and fabric when contact occurs during the stitching of curvilinear configurations. This will also prevent sharp edges from digging into the material from any direction that can result in fiber damage and wrinkling as shown in the previous section. The material chosen for this new model was S7 Tool Steel.

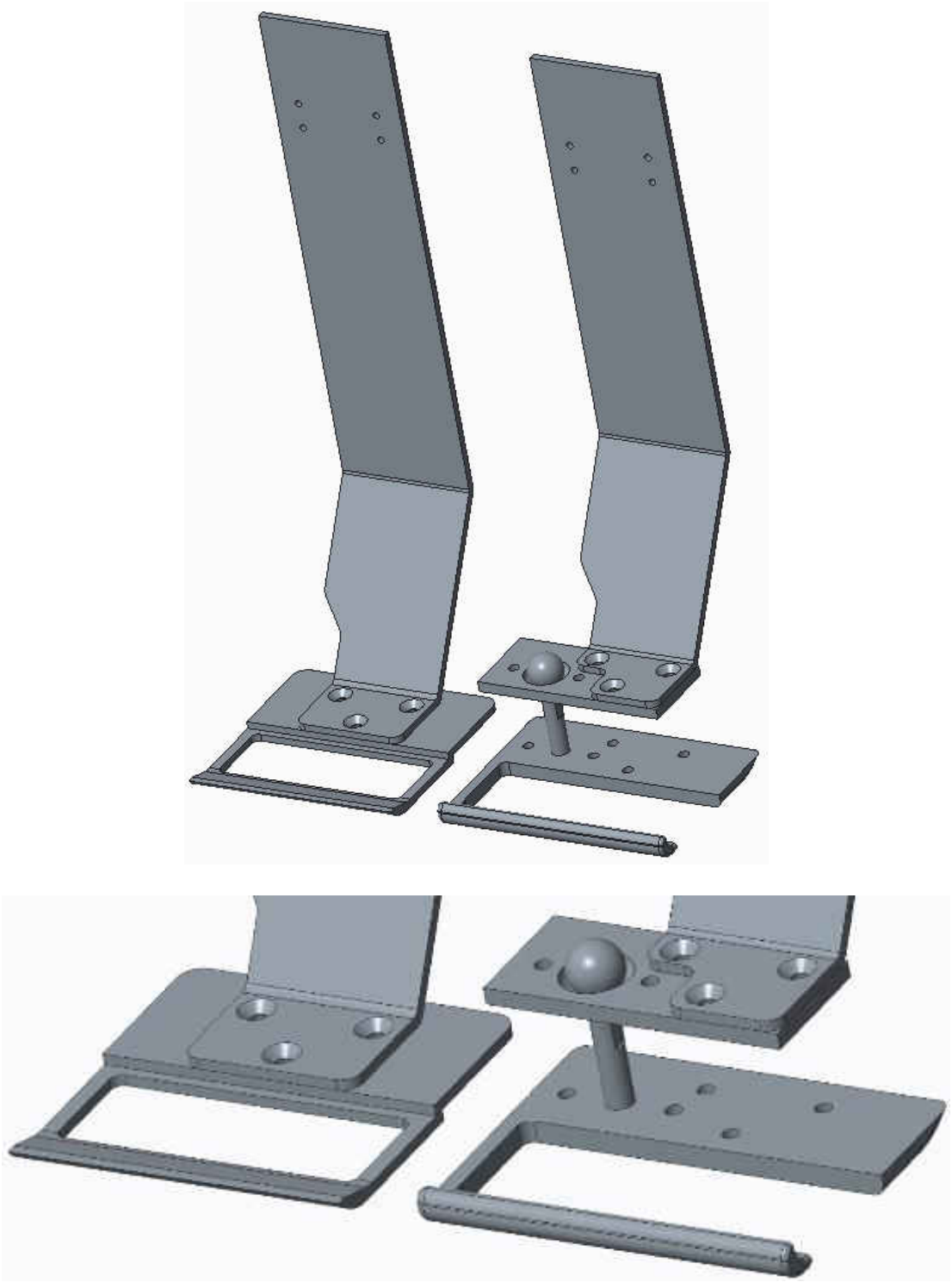

Figure 82 New Presser Foot Prototype 1

The model was milled from the CREO Parametric CAD files in STEP format, Figure 83.

Figure 83 New Milled Presser Foot Prototype 1

5 DISCUSSION

5.1 Compression Molded Discontinuous Fibers

5.1.1 Carbon Fiber Compression Molded Compound

The two kinds study for discontinuous fiber reinforced composites in this paper have each shown peculiar results. When considering the thermoset IM7/8552 samples as flat “bundles” of compacted fibers, the platelet-based composite shows the most isotropy at fiber length dimensions equal to that of the platelet width, 6.35 mm. However, its material properties have the lowest mean strength and standard deviation with 224.61 MPa and 38.46 respectively, and a modulus average of 31.72 GPa and 3.03 for standard deviation. With an increase in fiber length by a factor of four, or the 25.4 mm long fibers, flexural strength per individual sample saw a rise of as much as two times the lowest recorded strength. Even though samples were cut from the same panel made, the random nature of all the platelet directions can truly be noticeable for the 25.4 mm long fibers. The material properties for flexural strength were quite scattered coming out with a mean of 298.37 MPa, and a standard deviation of 80.68, but the modulus has a mean of 34.4GPa and only 6.0 for a standard deviation. The 12.7 mm long platelet samples gave the highest average strength with 402.88 MPa, but also came with a high standard deviation of 79.19 MPa. Modulus was also calculated to be the highest of the three with a mean of 40.40GPa and 8.62 for standard deviation. Overall, all samples showed the dominant failure mode comes from the matrix since platelet shapes were almost intact, and they were visible for all specimens at the braking sections.

The longer a fiber length the higher the material properties should be, but the 25.4 mm long platelets clearly do not behave in such trend. After calculating the volume (Figure 84) of a single platelet to the volume of the span used; the average number of localized platelets per

sample constantly decreased from 612, to 319, to 175 platelets for the 6.35, 12.7, and 25.4 mm long fibers, respectively. This shows that because the number of platelets in the system are low and there is a non-uniform platelet orientation due to the manufacturing process, less stresses were carried per sample. Therefore, even though scattered fiber orientations in a composite can give isotropic material characteristics, having some sort of control over its orientation will lead to more constant/predictable material properties.

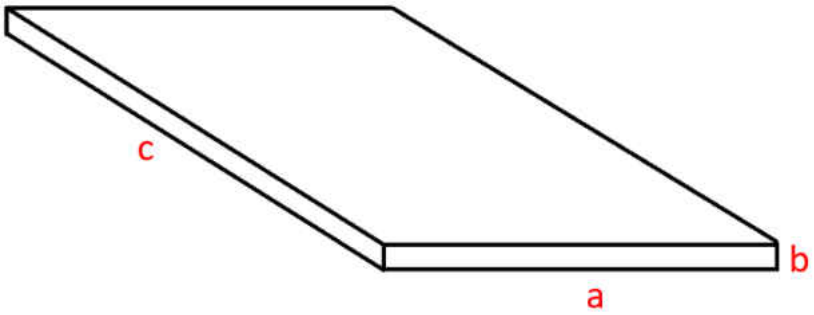

Figure 84 Volume of a Single IM7/8552 Platelet

where: a= 6.35 mm, b= 0.13 mm, c= 6.35/12.7/25.4 mm

If a structure is manufactured with IM7/8552 platelet-based composites that would be subjected to similar load conditions, the dimension of the platelets used need to be determined based on what the goal is. If the most isotropy is required, a shorter length of fibers with respect to the object's dimensions would help acquire such behavior. If high material properties are needed, then use of longer fibers are most certainly the best option but having a certain control of

how fibers are oriented with respect to the applied loads is also a key factor to achieving such goal.

5.1.2 Glass Fiber Organosheet Composite

After compacting JMs Nylon 6 thermoplastic composites and testing them in two different directions, the semi-finished sheets show there is a general fiber orientation which results in a difference in material properties. A correlation as span to thickness ratio increases can also be found, where a span of 20mm was the strongest for both biased and unbiased direction (Figure 85) with 400.25 and 289.72 MPa respectively and standard deviations of 16.88 and 40.50. A continuous decrease in flexural strength could also be observed as the span and ratios grew larger. The biased direction strength relation declined at a faster rate than the unbiased, with the unbiased ending at a higher flexural strength mean for the largest span.

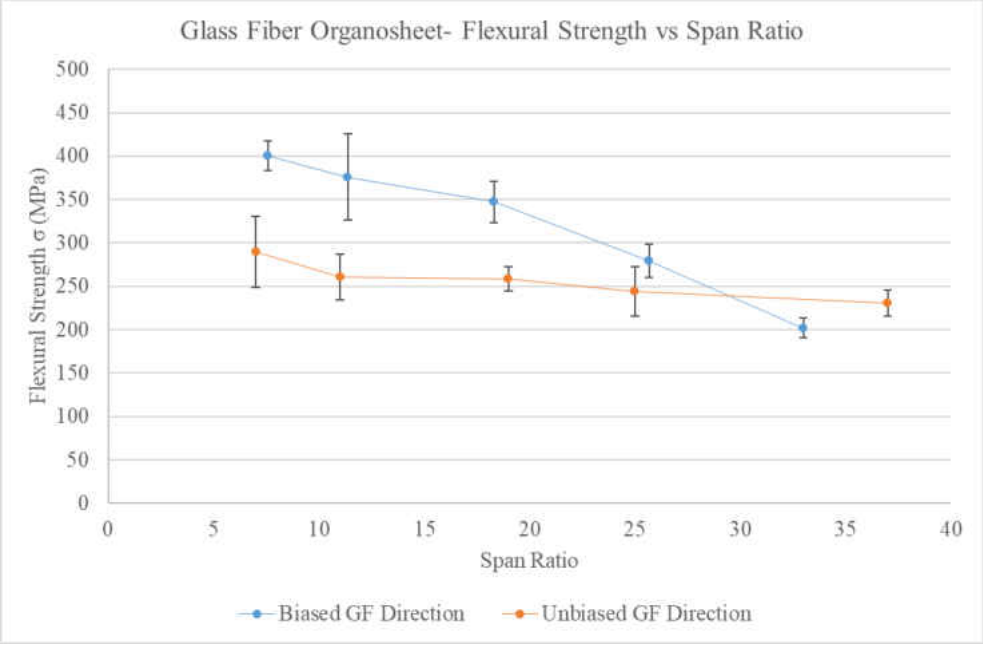

Figure 85 Glass Fiber Biased & Unbiased Directions: Flexural Strength Combined Error Bar Graph

The modulus behavior for both directions started in a similar manner but differed after a span to thickness ratio of about 18.5 (50mm span) was calculated. The biased direction obtained its maximum flexural modulus at said point, but the unbiased kept on increasing as the ratio grew larger (Figure 86). The design of experiments approach indicated that there is a strong interaction between the two factors of span and general fiber direction, where flexural modulus is the most affected by span.

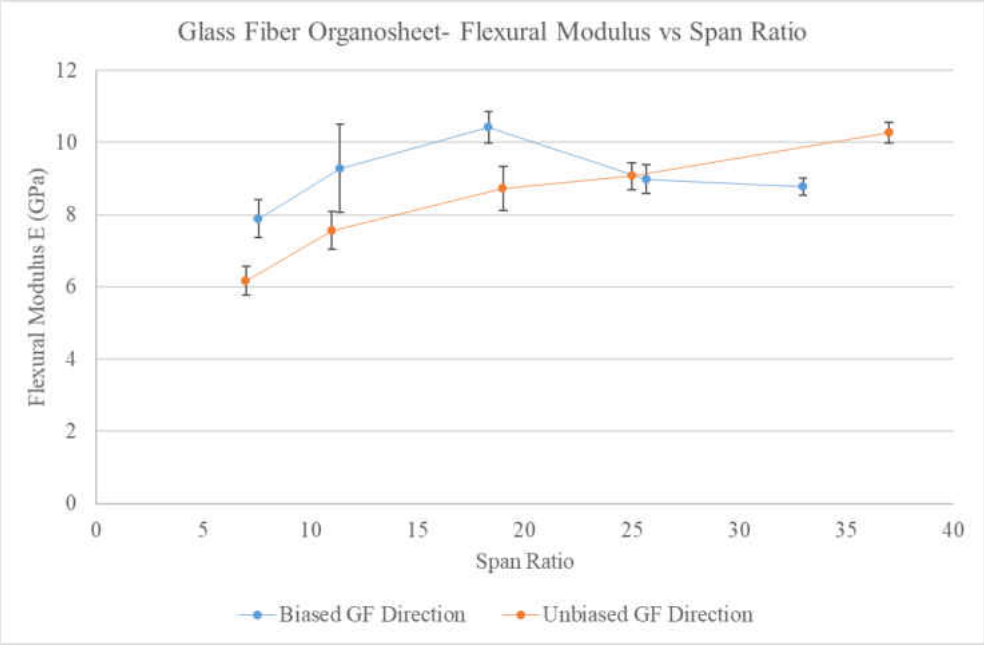

Figure 86 Glass Fiber Biased & Unbiased Directions: Flexural Modulus Combined Error Bar Graph

Johns Manville has a way of controlling the fiber orientation to a certain extent, which has shown that such manufacturing process helps limit the variance on material properties calculated, as well as how it can be applied to three-dimensional objects.

5.2 Non-crimp Fabric

Based on the new stitching objective with ISAAC, two testing methods of compaction and wrinkling were applied on a dry fabric to investigate behavior of non-crimp fabrics to be used for stitching and resin infusion. Consequently, a new design for the current presser foot was manufactured to accommodate for change in surface as the machines moves.

The compaction tests showed parameters such as sample dimension, compaction speed, and thickness have no effect on the overall behavior of the dry fabric. The parameter with the most influence on fabric thickness is the number of compaction cycles on the same area of the fabric, which has been shown to increase localized fiber volume fractions. This compaction can result in different resin infusion behavior once the dry fabric is mixed with the resin. Therefore, it is advisable to not apply pressures higher than 100 kPa on the fabric in order to keep the material as intact as possible for a proper resin infusion process.

Wrinkling tests showed that as applied loads on the fabric increased, fiber bundles were damaged, and their orientations compromised. This fabric damage can result in resin rich pockets and defects, thus, lowering the quality of parts after infusion. Based on the lowest applied force (50 N) which did not damage the fabrics as much as the other forces; the pressure exerted based on an approximation of the area in contact with the fabric surface is roughly 420 kPa. Therefore, exceeding forces over the calculated limit can result in compromise of the fabric architecture which once again, is not advisable.

The new presser foot design will help accommodate to movements the old stiff presser foot cannot do, that is being able to move along an uneven surface while conforming to the fabric it stitches on. The type of spring which will be applied to the new presser foot will be chosen based on the spring constant and the maximum pressure it will apply with respect to the underside area of the new presser foot. The data for the tests administered can help decide what the desired or limit of the applied loads can be.

6 CONCLUDING REMARKS

6.1 Compression Molded Discontinuous Fibers

IM7/8552 platelet-based composites:

- The composite shows the most isotropy at fiber length dimensions equal to that of the platelet width, 6.35 mm.
- The Flexural Strength and Modulus were at the lowest material properties with 25.4 mm long fibers even though they should result in the highest properties due to higher aspect ratios. This can also be explained by low amounts of localized platelets, resulting in less stresses carried per sample.
- A random fiber orientation results in too much variance when fiber length is equally comparable to the sample dimensions. If most platelets were oriented towards the load directions, then higher material properties would be calculated.

JM Nylon 6 thermoplastic composites

- A general fiber direction is present on the semi-finished sheets. Giving it different material properties with different loading conditions.

- The shortest span ratio gives the highest flexural strength for both biased, and unbiased direction.
- A design of experiments approach indicates there is a strong response based of what direction samples are tested, while span also has the most affected by span ratio
- This type of composite shows that a preferred fiber orientation in an almost randomly oriented discontinuous fiber composite can help control the structural behavior of composites. Giving it an advantage over how other discontinuous structures are made.

6.2 Non-crimp Fabric

Compaction Tests:

- As more cycles are added to the same location, fiber condensation becomes dominant after the second trial, leading to higher fiber volume fractions.
- The thicker the fabric, the more fiber indentation will be seen on affected areas based on the used geometry for compaction.
- To maintain the non-crimp fabric as uncompacted as possible for infusion processes, it is advisable to avoid pressures over 100 kPa.

Wrinkling Tests:

- As increasing forces are applied to the surface, more fiber damage will be present after dragging an object along it.
- Based on the applied forces and calculated critical pressure along the surface, anything over 400 kPa would result in fiber damage and compromised architecture. Resulting in defects with low quality parts.

Overall, both tested cases could compromise the fiber architecture, leading to setbacks during resin infusion and structural defects after curing of the composite.

New Presser Foot Design:

- The new model is set to help the stitching head move along the surface as it changes from different locations.
- Based on data from both compaction and wrinkling tests, it is not advisable for the spring force to be extremely high, as it could damage the fabric when the bottom of the presser foot is dragged along curved surfaces. The amount of pressure exerted by the new design depends the spring constant the underside contact area of the presser foot.

6.3 Future Work

6.3.1 Compression Molded Discontinuous Fibers

The first part of this thesis sets the foundations for future applications with discontinuous fiber reinforced composites. The explored size effect should be further quantified using progressive damage modeling tools in order to determine the interaction and combination between different damage modes in composite.

6.3.2 Non-crimp Fabric

This project set a starting point for the design of a new presser foot prototype that allows for a compliant system to enable stitching of the curvilinear surfaces. The future work should consider analysis of the compaction process with wrinkle formation. Specifically, finite element modeling efforts can consider the non-uniform contact stress distribution during the roller compaction: this can provide more insight into the stress levels that lead to wrinkle formation when complex geometry, such as leading edge of the presser foot, comes in contact with the layup of NCF. Furthermore, more experimental analysis of the wrinkle formation should be conducted to further inform the design of the stitching process about the possible defect formation. Finally, the installation of the presser-foot on ISAAC is required to explore if it properly integrates with the robotic arm. This will allow to identify if any changes to the initial design is required.

REFERENCES

[1] I. M. Daniel and O. Ishai, “Engineering Mechanics of Composite Materials, 2nd Ed”, Page 30. New York: Oxford University Press, 2006.

[2] V. D. Azzi and S. W. Tsai, “Strength of Laminated Composite Materials.,” *AIAA Journal*, vol. 4, no. 2, pp. 296–301, Feb. 1966, doi: 10.2514/3.3431.

[3] T. D. Skinner, S. Datta, A. Chattopadhyay, and A. Hall, “Biaxial Fatigue Damage in Quasi Isotropic Laminates,” presented at the AIAA Scitech 2020 Forum, Orlando, FL, Jan. 2020, doi: 10.2514/6.2020-0475.

[4] G. Nino, O. Bergsma, H. Bersee, and A. Beukers, “Structural Evaluation of Woven Composites,” presented at the 48th AIAA/ASME/ASCE/AHS/ASC Structures, Structural Dynamics, and Materials Conference, Honolulu, Hawaii, Apr. 2007, doi: 10.2514/6.2007-2354.

[5] A. Hindersmann, “Confusion about infusion: An Overview of Infusion Processes,” Composites Part A: Applied Science and Manufacturing, vol. 126, p. 105583, Nov. 2019, doi: 10.1016/j.compositesa.2019.105583.

[6] T. Okabe, T. Sasayama, and J. Koyanagi, “Micromechanical Simulation of Tensile Failure of Discontinuous Fiber-reinforced Polymer Matrix Composites using Spring Element Model,” Composites Part A: Applied Science and Manufacturing, vol. 56, pp. 64–71, Jan. 2014, doi: 10.1016/j.compositesa.2013.09.012.

[7] C. Chang, H. Conway, and T. Weaver, “The Elastic Constants and Bond Stresses for a Three-dimensional Composite Reinforced by Discontinuous Fibers,” presented at the 13th Structures, Structural Dynamics, and Materials Conference, San Antonio,TX,U.S.A., Apr. 1972, doi: 10.2514/6.1972-397.

[8] J.-W. Lee and D. Allen, “A Model for Predicting the Effective Elastic Properties of Randomly Oriented Fiber Composites Subjected to Hot Pressing, Extrusion, and Rolling,” presented at the 30th Structures, Structural Dynamics and Materials Conference, Mobile,AL,U.S.A., Apr. 1989, doi: 10.2514/6.1989-1253.

[9] K. R. Ramakrishnan, N. Le Moigne, O. De Almeida, A. Regazzi, and S. Corn, “Optimized Manufacturing of Thermoplastic Biocomposites by Fast Induction-heated

Compression Moulding: Influence of Processing Parameters on Microstructure Development and Mechanical Behaviour," Composites Part A: Applied Science and Manufacturing, vol. 124, p. 105493, Sep. 2019, doi: 10.1016/j.compositesa.2019.105493.

[10] Zaldua et al., "Nucleation and Crystallization of PA6 Composites Prepared by T-RTM: Effects of Carbon and Glass Fiber Loading," Polymers, vol. 11, no. 10, p. 1680, Oct. 2019, doi: 10.3390/polym11101680.

[11] S.-J. Joo, M.-H. Yu, W. Seock Kim, J.-W. Lee, and H.-S. Kim, "Design and Manufacture of Automotive Composite Front Bumper Assemble Component Considering Interfacial Bond Characteristics Between Over-molded Chopped Glass Fiber Polypropylene and Continuous Glass Fiber Polypropylene Composite," Composite Structures, vol. 236, p. 111849, Mar. 2020, doi: 10.1016/j.compstruct.2019.111849.

[12] B. Fengler et al., "Manufacturing Uncertainties and Resulting Robustness of Optimized Patch Positions on Continuous-Discontinuous Fiber Reinforced Polymer Structures," Composite Structures, vol. 213, pp. 47–57, Apr. 2019, doi: 10.1016/j.compstruct.2019.01.063.

[13] P. Feraboli, E. Peitso, F. Deleo, T. Cleveland, and P. B. Stickler, "Characterization of Prepreg-Based Discontinuous Carbon Fiber/Epoxy Systems," Journal of Reinforced Plastics and Composites, vol. 28, no. 10, pp. 1191–1214, May 2009, doi: 10.1177/0731684408088883.

[14] P. Feraboli, E. Peitso, T. Cleveland, and P. Stickler, "Characterization of Discontinuous Carbon Fiber / Epoxy Systems for Aerospace Applications: PART II," presented at the 49th AIAA/ASME/ASCE/AHS/ASC Structures, Structural Dynamics, and Materials Conference
 16th AIAA/ASME/AHS Adaptive Structures Conference
 10t, Schaumburg, IL, Apr. 2008, doi: 10.2514/6.2008-1939.

[15] Johns Manville - Advanced Composite Bulletin, "CR-6 Series Product Overview". April 2019.

[16] Z. Rao, L. Ou, Y. Wang, and P.-C. Wang, "A Self-Piercing-Through Riveting Method for Joining of Discontinuous Carbon Fiber Reinforced Nylon 6 Composite," Composite Structures, vol. 237, p. 111841, Apr. 2020, doi: 10.1016/j.compstruct.2019.111841.

[17] A. Pegoretti, M. Fidanza, C. Migliaresi, A.T. DiBenedetto,"Toughness of the Fiber/Matrix Interface in Nylon-6/Glass Fiber Composites", Composites Part A: Applied Science and Manufacturing, Volume 29, Issue 3, 1998, Pages 283-291, ISSN 1359-835X, https://doi.org/10.1016/S1359-835X(97)00079-1.

[18] Dawn Jegley, Adam Przekop, Marshall Rouse, Andrew Lovejoy, Alex Velicki, Kim Linton, Hsi-Yung Wu, Jaime Baraja, Patrick Thrash, and Krishna Hoffman "Development of Stitched Composite Structure for Advanced Aircraft," September 2015, NF1676L-20691

[19] A. E. Lovejoy and F. A. Leone, "Tension and Bending Testing of an Integral T-cap for Stitched Composite Airframe Joints," presented at the 57th AIAA/ASCE/AHS/ASC Structures, Structural Dynamics, and Materials Conference, San Diego, California, USA, Jan. 2016, doi: 10.2514/6.2016-2180.

[20] W. Chen, D. Zhang, X. Ren, and J. Lua, "A Coupled Flow and Residual Stress Model for Predicting Performance Variations of Composites Manufactured via Vacuum Assisted Resin Transfer Molding," presented at the AIAA Scitech 2020 Forum, Orlando, FL, Jan. 2020, doi: 10.2514/6.2020-2111.

[21] E. Glaessgen, I. Raju, and C. Poe, Jr., "Delamination and Stitch Failure in Stitched Composite Joints," presented at the 40th Structures, Structural Dynamics, and Materials Conference and Exhibit, St. Louis,MO,U.S.A., Apr. 1999, doi: 10.2514/6.1999-1247.

[22] V. Koissin, J. Kustermans, S. V. Lomov, I. Verpoest, B. Van Den Broucke, and V. Witzel, "Structurally Stitched NCF Preforms: Quasi-static Response," *Composites Science and Technology*, vol. 69, no. 15–16, pp. 2701–2710, Dec. 2009, doi: 10.1016/j.compscitech.2009.08.015.

[23] J. Sawyer, "Effect of Stitching on the Strength of Bonded Composite Single Lap Joints," presented at the 24th Structures, Structural Dynamics and Materials Conference, Lake Tahoe,NV,U.S.A., May 1983, doi: 10.2514/6.1983-969.

[24] Z. Yousaf, P. Potluri, and P. J. Withers, "Influence of Tow Architecture on Compaction and Nesting in Textile Preforms," *Appl Compos Mater*, vol. 24, no. 2, pp. 337–350, Apr. 2017, doi: 10.1007/s10443-016-9554-8.

[25] L. Li, Y. Zhao, J. Yang, J. Zhang, and Y. Duan, “An Experimental Investigation of Compaction Behavior of Carbon Non-Crimp Fabrics for Liquid Composite Molding,” *J Mater Sci*, vol. 50, no. 7, pp. 2960–2972, Apr. 2015, doi: 10.1007/s10853-015-8860-0.

[26] Hexcel – Product Data Sheet, “ HexPly 8552 Epoxy Matrix (180C/365F Curing Matrix”, 2020.

[27] J.-I. Kim, Y.-T. Hwang, K.-H. Choi, H.-J. Kim, and H.-S. Kim, “Prediction of the Vacuum Assisted Resin Transfer Molding (VARTM) Process Considering the Directional Permeability of Sheared Woven fabric,” *Composite Structures*, vol. 211, pp. 236–243, Mar. 2019, doi: 10.1016/j.compstruct.2018.12.043.

VITA

Anibal Benjamin Beltran Laredo

Department of Mechanical and Aerospace Engineering

Old Dominion University

Norfolk, VA

Education

Bachelor of Science in Mechanical Engineering, Old Dominion University Norfolk, VA, 2018

Concentration: Power Energy Conversions

Minor 1: Aerospace Engineering Minor 2: Criminal Justice

Presentations

2018 Automotive Composites Conference and Exhibition, Novi, Michigan, 2018

Presented Forged Carbon Fiber project during student competition

Title: *Application of Hybrid Compression Molded Composites for design and manufacturing of Rear Suspension Rocker Automotive Composite*

Publications

Siavash Sattar, Benjamin Beltran Laredo, Diego Pedrazzoli, Mingfu Zhang, and Oleksandr G. Kravchenko, “Understanding size Effects on Flexural Properties in Discontinuous Fiber Reinforced Nylon Composites”, Composites and Advanced Materials and Expo, 2020.